Gamma-Ray Spectroscopy of $^{11}_{\Lambda}B$ and $^{10}_{\Lambda}B$

A dissertation submitted in partial fulfillment of
the requirements for the degree of

Doctor of Science

by

Yusuke Miura

Department of Physics, Faculty of Science,
Tohoku University

2005

Abstract

We have measured γ rays from ${}^{11}_{\Lambda}$B and ${}^{10}_{\Lambda}$B using a germanium detector array, Hyperball. The γ-ray spectroscopy of the ${}^{11}_{\Lambda}$B was performed by the ^{11}B(π^+, K^+) reaction at the KEK-PS K6 beam line. In this experiment, six γ-ray transitions from ${}^{11}_{\Lambda}$B were observed at 263.6 $\pm$ 0.5 (stat.) $\pm$ 1.1 (syst.) keV, 457.6 $\pm$ 1.2 $\pm$ 1.1 keV, 504.7 $\pm$ 1.0 $\pm$ 1.1 keV, 569.5.0 $\pm$ 0.5 $\pm$ 1.1 keV, 1483.3 $\pm$ 0.2 $\pm$ 0.7 keV and 2476.9 $\pm$ 2.1 $\pm$ 1.2 keV. Among these γ rays, the 1483-keV transition has two notable characteristics in the lifetime and the γ-ray yield. In the weak coupling scheme, there are three candidates for the spin assignment of this transition, namely $1/2^+ \rightarrow 5/2^+$, $3/2^+ \rightarrow 5/2^+$ and $1/2^+; T = 1 \rightarrow 5/2^+$. On the other hand, the peak at 2477 keV, which is fully broadened by Doppler effect, is suggested to be an $M1(3/2^+; T = 1 \rightarrow 1/2^+)$ where the $1/2^+$ state is based on the ^{10}B(1^+, 2154 keV) state.

The purpose of this experiment was to investigate the spin-dependent forces of ΛN effective interactions and to measure the magnetic moment of a Λ in the nucleus. The four spin-dependent parameters of ΛN effective interactions have been studied in the previous experiments using Hyperball. In the present experiment, the consistency of the previous results were tested from the energy spacing of the 1483-keV γ ray. All of three candidates for this transition were inconsistent with a theoretical prediction based on the parameters determined in previous experiments. If this transition is assigned to $1/2^+ \rightarrow 5/2^+$, which is the most probable assignment, the nucleon-spin dependent spin-orbit interaction parameter (S_N) can be determined to be -0.9 MeV. In this experiment, the magnetic moment of a Λ in the nuclear medium was also planned to measure from the $B(M1)$ of Λ spin-flip transition. However, the $B(M1)$ value was not measured in the present study because the spin assignment of observed transitions were not identically determined.

The γ-ray spectroscopy of the ${}^{10}_{\Lambda}$B was performed by the ^{10}B(K^-, π^-) reaction at the BNL-AGS D6 beam line. The purpose of this experiment was to investigate the energy spacing of the ground-state spin doublet in ${}^{10}_{\Lambda}$B $(2^-, 1^-)$, which is mainly determined by the spin-spin force of the ΛN effective interaction. In this experiment, the corresponding transition was not observed for the γ-ray energy region from 60 keV to 470 keV where the γ ray was expected to be observed. Using the calculated values of the (K^-, π^-) cross section for the ${}^{10}_{\Lambda}$B (2^-) and the ${}^{16}_{\Lambda}$O (1^-_2) states, it is concluded that the expected yield for the ${}^{10}_{\Lambda}$B $(2^-, 1^-)$ transition was not large enough to be observed.

Both of the structures of ${}^{11}_{\Lambda}$B and ${}^{10}_{\Lambda}$B imply that hypernuclear structure cannot be always reproduced consistently with the ΛN spin-dependent interaction parameters in the present framework.

Contents

Chapter 1 Introduction 1

§ 1 Hypernuclear γ-ray spectroscopy 1

1.1 ΛN effective interaction . . . 1

The spin-spin interaction . . . 4

The spin-orbit interaction . . . 5

The tensor interaction . . . 6

The ΛNN three-body interaction . . . 7

1.2 Magnetic moment of a Λ in the nucleus . . . 8

§ 2 Previous γ-ray spectroscopy experiments of hypernuclei 9

2.1 The γ-ray spectroscopy with the (π^+, K^+) reaction . . . 9

2.2 The γ-ray spectroscopy with the (K^-, π^-) reaction . . . 10

2.3 The γ-ray spectroscopy with the stopped K^- reaction . . . 11

§ 3 The γ-ray spectroscopy of ${}^{11}_{\Lambda}$B 12

3.1 Consistency check of the ΛN effective interaction . . . 12

3.2 The g-factor of a Λ in nuclear medium . . . 13

§ 4 The γ-ray spectroscopy of ${}^{10}_{\Lambda}$B 15

Chapter 2 γ-ray spectroscopy of ${}^{11}_{\Lambda}$B — Experimental Setup 17

§ 1 Overview 17

§ 2 KEK-PS K6 beamline 17

§ 3 Magnetic spectrometer system of K6 beamline 18

3.1 Spectrometer for incident particle . . . 18

3.2 Spectrometer for outgoing particle (SKS) . . . 21

§ 4 Hyperball 25

4.1 Germanium detectors for the hypernuclear experiments . . . 26

4.2 BGO scintillation counter . . . 29

4.3 Readout electronics . . . 31

§ 5 Target 32

§ 6 Trigger Logic 32

§ 7 Data acquisition system **34**

§ 8 Data summary **35**

Chapter 3 γ-ray spectroscopy of $^{11}_{\Lambda}$B — Analysis **36**

§ 1 Overview **36**

§ 2 Magnetic spectrometers **37**
2.1 Momentum reconstruction of incident particle . . . 38
2.2 Momentum reconstruction of outgoing particle . . . 40
2.3 Particle identification . . . 41
2.4 Vertex position and reaction angle . . . 42
2.5 Missing mass and binding energy of Λ . . . 45
2.6 Velocity of the recoiling $^{11}_{\Lambda}$B . . . 50

§ 3 Hyperball **51**
3.1 Event selection . . . 51
Coincidence with the (π^+, K^+) reaction . . . 51
BGO scintillation counter . . . 52
Pile-up rejection . . . 52
Reset veto . . . 53
3.2 Energy calibration . . . 55
3.3 γ-ray detection efficiency . . . 58
3.4 Doppler-shift correction . . . 59
3.5 Doppler-shift attenuation method (DSAM) . . . 59

Chapter 4 γ-ray spectroscopy of $^{11}_{\Lambda}$B — Results **63**

§ 1 Binding energy of $^{11}_{\Lambda}$B **63**

§ 2 γ-ray energy spectrum **63**
2.1 γ rays from $^{11}_{\Lambda}$B . . . 63
2.2 Systematic errors . . . 64

§ 3 γ-ray gated excitation energy **66**

§ 4 Lifetime measurement **69**
4.1 Lifetime of the γ-ray transitions in $^{11}_{\Lambda}$B . . . 69
4.2 Systematic errors . . . 70

Chapter 5 γ-ray spectroscopy of ${}^{11}_{\Lambda}$B — Discussion 76

§ 1 Properties of the observed γ rays 76

§ 2 Spin assignment 78
2.1 1483-keV transition 78
2.2 2477-keV transition 79

§ 3 Consistency of the ΛN effective interaction parameters 81
3.1 1483-keV transition 81
3.2 2477-keV transition 81
3.3 ΛN effective interaction parameters 82

§ 4 $B(M1)$ measurement 82

Chapter 6 γ-ray spectroscopy of ${}^{10}_{\Lambda}$B 84

§ 1 Overview 84

§ 2 Experimental setup 84

§ 3 γ rays from ${}^{10}_{\Lambda}$B 86

§ 4 Energy spacing of ${}^{10}_{\Lambda}$B $(2^-, 1^-)$ 87

§ 5 ΛN effective interaction parameters 91

Chapter 7 Summary 94

Chapter A Matrix elements of the two-body ΛN forces 96

Chapter B Wave function of ^{10}B 99

Chapter C Transition probability in the weak-coupling scheme 101

Chapter D Previous experiment for the γ-ray spectroscopy of ${}^{10}_{\Lambda}$B 104

Chapter **106**

List of Figures

1.1 Schematic view of the low-lying level structure of a Λ hypernucleus. . 3
1.2 Low-lying level structure of ${}^{7}_{\Lambda}$, ${}^{12}_{\Lambda}$C and ${}^{13}_{\Lambda}$C. 6
1.3 The psuedo-scaler meson exchange between a Λ and a nucleon. 7
1.4 The γ-ray spectra obtained from the ^{7}Li$(\pi^+, K^+){}^{7}_{\Lambda}$Li reaction. 10
1.5 Calculated level scheme of ${}^{11}_{\Lambda}$B by Millener. 16
2.1 Schematic view of the KEK-PS K6 beamline. 18
2.2 Schematic view of the spectrometer for the incident pions. 19
2.3 Schematic view of BH1 and BH2. 20
2.4 Schematic drawing of the drift chamber and the read-out system for the incident particle. 22
2.5 Cell structure of the drift chambers for the incident particle. 22
2.6 Schematic view of SKS. 23
2.7 Wire configuration of SDC4. 24
2.8 Schematic drawing of Hyperball. 25
2.9 The crystal of reverse-electrode coaxial type Ge detector. p-type electrode is on the outside. 26
2.10 Schematic drawing of the Ge detectors for the Hyperball system fabricated by Eurisys Measures. 27
2.11 The peak shape difference between at (a) the beginning and (b) the end of the experiment. 28
2.12 Transistor reset-type preamplifier. 28
2.13 Schematic drawing of the LN_2 supplying system. 29
2.14 Schematic drawing of Ge detector and BGO scintillator. 30
2.15 Schematic view of the light output from BGO scintillator for a few hundred keV γ ray. 30
2.16 Block diagram of readout electronics of the Ge detectors. 31
2.17 Block diagram of trigger logic. 33
2.18 Block diagram of Ge calibration trigger. 34
2.19 Block diagram of data acquisition system. 35
3.1 Flow chart of a event-by-event analysis. 37
3.2 Minimum χ^2_{K6} distribution of the incident particles. 39
3.3 Momentum distribution of the incident particles. 39
3.4 Minimum χ^2_{SKS} distribution of the outgoing particles. 40
3.5 The time-of-flight spectrum measured for the incident particles. . . . 41
3.6 The measured mass spectrum of the outgoing particles. 42
3.7 The distribution of the scattering angle measured for the (π^+, K^+) event. 43
3.8 Angular resolution estimated by comparing the scattering angle measured for a 0.72 GeV/c π^+ beam without target. 43

3.9 The z-vertex distribution for 6-cm target (left) and their differentials for z axis (right). . . . 44
3.10 The z-vertex distribution for 10-cm target and their differentials for z axis. . . . 44
3.11 Correlation between the horizontal scattering angle (dx/dz) and the missing mass measured for the carbon target. . . . 46
3.12 Λ-binding energies in ${}^{12}_{\Lambda}$C and ${}^{11}_{\Lambda}$B measured for the target of 3.54, 2.38, 14.3 and 23.8 g/cm^2 thick, respectively. . . . 47
3.13 Λ-binding energies in ${}^{11}_{\Lambda}$B measured for the targets of 14.3 and 23.8 g/cm^2 thick. . . . 49
3.14 Distributions of the momentum difference between the two spectrometers measured for 0.72 GeV/c π^+ without target with ^{11}B target (23.8 g/cm^2). . . . 49
3.15 Velocity distribution of the recoiling ${}^{11}_{\Lambda}$B, which is measured from the momenta of the incident and the outgoing particles. . . . 50
3.16 Energy (ADC) dependence of the TDC value (TFA) of γ rays for a typical Ge detector. . . . 51
3.17 BGO suppression. . . . 53
3.18 Pile-up rejection. . . . 54
3.19 Illustration for the pile-up rejection. . . . 54
3.20 Residuals of the measured γ-ray energies in Table 3.3. Measured energies were not used for the calibration. . . . 56
3.21 The long term stability of the peak position of the Ge detectors. . . . 57
3.22 Total photo-peak efficiency of Ge detectors. . . . 58
3.23 Stopping time of ${}^{11}_{\Lambda}$B in the ^{11}B target as a function of the initial velocity (β) calculated using the SRIM code. . . . 60
3.24 Stopping power of boron ion in various materials compared between the calculation by the SRIM code. . . . 61
3.25 Simulated peak shapes for the lifetime of 0.1, 0.5, 1.0 and 7.5 psec. . . 62
4.1 Excitation energy spectra of ${}^{11}_{\Lambda}$B. . . . 64
4.2 γ-ray spectra in the ^{11}B$(\pi^+, K^+){}^{11}_{\Lambda}$B reaction. . . . 65
4.3 The excitation energy spectra of ${}^{11}_{\Lambda}$B plotted for those events in which the γ rays from ${}^{11}_{\Lambda}$B were observed. . . . 67
4.4 The excitation energy spectra plotted for those events in which the γ rays were observed from a certain region. . . . 68
4.5 γ-ray energy spectrum for the 264-keV transition before (left) and after (right) the Doppler-shift correction. Fitting results were shown with the solid lines. . . . 73
4.6 γ-ray energy spectrum for the 458-keV transition before (left) and after (right) the Doppler-shift correction. Fitting results were shown with the solid lines. . . . 73

4.7 γ-ray energy spectrum for the 500-keV transition before (left) and after (right) the Doppler-shift correction. Fitting results were shown with the solid lines. 74
4.8 γ-ray energy spectrum for the 570-keV transition before (left) and after (right) the Doppler-shift correction. Fitting results were shown with the solid lines. 74
4.9 γ-ray energy spectrum for the 1483-keV transition before (left) and after (right) the Doppler-shift correction. Fitting results were shown with the solid lines. 75
4.10 γ-ray energy spectrum for the 2477-keV transition before (left) and after (right) the Doppler-shift correction. Fitting results were shown with the solid lines. 75
5.1 Possible candidates for the spin-assignment of the 1483-keV transition. p-type electrode is on the outside. 79
5.2 The most probable assignments for the 1483-keV and the 2477-keV transitions. 80
6.1 Schematic view of the BNL-AGS D6 beamline. 85
6.2 Schematic view of the BNL-AGS E930('01) setup around the target. . 85
6.3 Expected level scheme of ${}^{10}_{\Lambda}$B. 87
6.4 Excitation energy spectra of ${}^{10}_{\Lambda}$B. 88
6.5 The (K^-, π^-) scattering angle dependence in the excitation energy of ${}^{10}_{\Lambda}$B. 89
6.6 γ-ray spectrum measured for the ${}^{10}_{\Lambda}$B bound-state region and unbound region. 90
6.7 γ-ray spectrum of the ${}^{16}_{\Lambda}$O $(1^-_2 \rightarrow 1^-_1, 0^-)$ transition measured using the H_2O target after the Doppler-shift correction. 92
6.8 Cross sections for the 930 MeV/c K^- calculated by Motoba. 92
6.9 The energy dependence of the γ-ray detection efficiency. 93
6.10 Energy dependence of the expected yield for the the ${}^{10}_{\Lambda}$B $(2^- \rightarrow 1^-)$ transition and the yield for the assumed peak on the background. . . 93
C.1 The electromagnetic transitions between the hypernuclear states, which are based on a transition of the core nucleus. 102

List of Tables

1.1 The ΛN effective interaction parameters derived for several hypernuclei by Millener. . . . 4
2.1 The specification of the beam line spectrometer. . . . 19
2.2 The specification of SKS. . . . 21
2.3 Specification of the drift chambers. . . . 24
2.4 Properties of BGO scintillatiors. . . . 30
2.5 Total number of pions irradiated on each target. . . . 35
3.1 The momentum loss in the targets of 1-cm thick. . . . 46
3.2 γ-ray sources for the off-beam energy calibration. . . . 55
3.3 Observed γ rays during the in-beam period where the Doppler effect is expected to be small. . . . 55
3.4 Energy resolution of the Ge detectors measured for the in-beam period. 56
4.1 Number of events and relative intensities for observed γ transitions. . 66
4.2 Lifetimes of the observed γ transitions in ${}^{11}_{\Lambda}$B. . . . 69
5.1 The difference in the measured and the expected energy spacing of the hypernuclear levels measured in the previous experiments. . . . 82
5.2 $B(M1)$ values for observed γ rays from ${}^{11}_{\Lambda}$B. . . . 83
B.1 The comparison between theory and experiment for electromagnetic transition strengths in ^{10}B. . . . 100
B.2 The [42] symmetry components of the Barker I wave functions for ^{10}B. 100
D.1 Difference in the experimental setup. . . . 105

Chapter 1

Introduction

§ 1 Hypernuclear γ-ray spectroscopy

One of the most important features of γ-ray spectroscopy is that we can achieve an excellent energy resolution by using a germanium (Ge) detector. It has been a powerful method for nuclear physics, for example, by measuring precise level energies, spin-parities and lifetimes of the nuclear states. However, γ-ray spectroscopy with Ge detectors has not been applied to the hypernuclear physics for a long time. It is because of a short lifetime of a Λ particle and a small cross section of the hypernuclear production. The γ-ray detection has to be performed near high intensity meson beams such as π^+ or K^-. In such a situation, high counting rate and huge backgrounds from beam particles had prevented us from receiving benefit from a good performance of Ge detectors. In recent years, as techniques developed, Ge detectors have come to be used for hypernuclear physics.

In 1998, Hyperball, an array of 14 Ge detectors, was constructed in order to measure the precise structure of hypernuclei. The study of the hypernuclear structure measured by reaction spectroscopy using magnetic spectrometers is limited by the energy resolution of around 1 MeV (FWHM). On the other hand, the energy resolution of a typical Ge detector is around 2 keV (FWHM). Thus, Hyperball opened a new era for the hypernuclear γ-ray spectroscopy and the study of the hypernuclear structure was drastically improved.

Particularly, the spin-dependence of the ΛN effective interactions has come to be well studied from precise structure of hypernuclei with its excellent resolution. In the present study, the spin-dependence of the ΛN effective interaction was investigated by the γ-ray spectroscopy of $^{11}_{\Lambda}$B and $^{10}_{\Lambda}$B. As a next step of hypernuclear structure studies via γ-ray spectroscopy, the Λ-spin-flip B(M1) is going to be measured to investigate the magnetic moment of a Λ in the nucleus.

1.1 ΛN effective interaction

The ΛN interaction in the free space can be investigated by ΛN scattering experiments. However, such experiments are very difficult to perform because of the short lifetime of Λ particle. Therefore, the information on the ΛN interaction has been obtained from structure of hypernuclei.

The theoretical calculations on the ΛN effective interaction are established to extract pure two-body effects from structure of hypernuclei. The two-body effective interaction between a nucleon in the p-orbit and a Λ in the s-orbit ($p_N s_\Lambda$) can be expressed in terms of five radial integrals associated with each term in

$$V_{\Lambda N}(r) = V_0(r) + V_\sigma(r)\mathbf{s_N}\cdot\mathbf{s_N} + V_\Lambda(r)\mathbf{l_{N\Lambda}}\cdot\mathbf{s_\Lambda} + V_N(r)\mathbf{l_{N\Lambda}}\cdot\mathbf{s_N} + V_T(r)\mathbf{S_{N\Lambda}}, \quad (1.1)$$

where $\mathbf{l_{N\Lambda}}$ is the relative orbital angular momentum and

$$\mathbf{S_{N\Lambda}} = 3\frac{(\sigma_\mathbf{N}\cdot\mathbf{r})(\sigma_\mathbf{\Lambda}\cdot\mathbf{r})}{r^2} - \sigma_\mathbf{N}\cdot\sigma_\mathbf{\Lambda}$$

where $r = |\mathbf{r_N} - \mathbf{r_\Lambda}|$ [1, 2]. These five integrals are introduced as parameters and denoted by $\overline{V}$, Δ, S_Λ, S_N and T. For example, Δ is defined as,

$$\Delta = \int \phi^*_{\Lambda N}(r)V_\sigma(r)\phi_{\Lambda N}(r)r^2 dr, \quad (1.2)$$

where $\phi_{\Lambda N}$ is the relative wave function between a Λ and a nucleon. The other parameters are similarly defined. Among these five parameters, the average central interaction parameter ($\overline{V}$) is determined to reproduce the measured Λ separation energies (B_Λ) for several p-shell hypernuclei. The other four parameters express spin-dependent forces, namely, the spin-spin force (Δ), the Λ-spin-dependent spin-orbit force (S_Λ), the nucleon-spin-dependent spin-orbit force (S_N) and the tensor force (T).

Using the jj two-body matrix elements, these parameters can be expressed as follows [3],

$$\begin{aligned}
\overline{V} &= \frac{1}{12}\left(V_0 + 5V_2 + 3V_{11} + 3V_{31}\right)\\
\Delta &= \frac{1}{9}\left(V_0 + 5V_2 - V_{11} - 5V_{31} + 8\sqrt{2}V_{od}\right)\\
S_\Lambda &= \frac{1}{12}\left(-2V_0 + 5V_2 + 2V_{11} - 6V_{31} - 4\sqrt{2}V_{od}\right)\\
S_N &= \frac{1}{12}\left(-2V_0 + 5V_2 - 6V_{11} + 3V_{31}\right)\\
T &= -\frac{5}{108}\left(2V_0 + V_2 - 2V_{11} - V_{31} - 2\sqrt{2}V_{od}\right).
\end{aligned} \quad (1.3)$$

Here, V_0, V_2, V_{11}, V_{31} and V_{od} are defined as,

$$\begin{aligned}
V_0 &= \langle p_{N1/2}s_{\Lambda 1/2};\ 0^-|V_{\Lambda N}|\ p_{N1/2}s_{\Lambda 1/2};\ 0^-\rangle\\
V_2 &= \langle p_{N3/2}s_{\Lambda 1/2};\ 2^-|V_{\Lambda N}|\ p_{N3/2}s_{\Lambda 1/2};\ 2^-\rangle\\
V_{11} &= \langle p_{N1/2}s_{\Lambda 1/2};\ 1^-|V_{\Lambda N}|\ p_{N1/2}s_{\Lambda 1/2};\ 1^-\rangle\\
V_{31} &= \langle p_{N3/2}s_{\Lambda 1/2};\ 1^-|V_{\Lambda N}|\ p_{N3/2}s_{\Lambda 1/2};\ 1^-\rangle\\
V_{od} &= \langle p_{N3/2}s_{\Lambda 1/2};\ 1^-|V_{\Lambda N}|\ p_{N1/2}s_{\Lambda 1/2};\ 1^-\rangle.
\end{aligned} \quad (1.4)$$

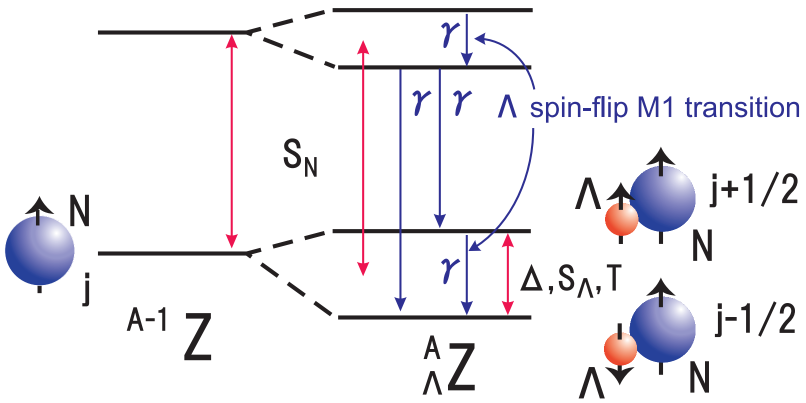

Figure 1.1: Schematic view of the low-lying level structure of a Λ hypernucleus. If core spin $j \neq 0$, one state of the core nucleus splits into two states of hypernucleus. By observing γ rays from hypernuclei, spin-dependent forces of ΛN interaction can be investigated. see text for details.

Since hypernuclear states are characterized by the combination of these matrix elements, energies of the states can be written in terms of these five parameters.

In order to study the spin dependence of the ΛN effective interaction, it is convenient to consider a weak-coupling scheme that the structure of hypernuclei consists of two components, a Λ and the remaining nucleons collectively called as a "core". If the core spin is not zero ($j_{core} \neq 0$), one state of the core nucleus splits into two states in the hypernucleus according to the spin direction of a Λ as shown in Fig. 1.1. Since the energy spacing between these two states is typically of the order of 100 keV, it is necessary to use Ge detectors to observe the γ transition between these states. Such spin doublets are often called "hypernuclear fine structure", and γ transitions between these doublets are called "Λ-spin-flip $M1$ transition". In this weak-coupling scheme, the wave functions of the hypernuclear state are described by the shell-model calculation. Then, all of the spin-dependent parameters were experimentally determined from the energy spacings of specific hypernuclear states which have a dominant contribution from one parameter (see Appendix A).

The values of the four spin-dependent parameters were derived by Millener [3] using available experimental data, namely $^{7}_{\Lambda}$Li [4], $^{9}_{\Lambda}$Be [5], $^{13}_{\Lambda}$C [6] and $^{16}_{\Lambda}$O [7]. The parameters given from Eq. (1.1) are derived for several hypernuclei as shown in Table 1.1. In principle, these parameters are taken to be constant throughout the shell but the integrals can take slightly different values because the ΛN wave function ($\phi_{\Lambda N}(r)$) is affected by the size of hypernuclei.

These phenomenological parameters can be compared with elementary ΛN two-body interaction models which are calculated by one-boson-exchange (OBE) models [9] or quark models through G-matrix method which describes the difference

Table 1.1: The ΛN effective interaction parameters derived for several hypernuclei by Millener [3]. These parameters are defined by Eq.(1.2) and chosen to reproduce the experimental data of ${}^{7}_{\Lambda}$Li, ${}^{9}_{\Lambda}$Be, ${}^{13}_{\Lambda}$C and ${}^{16}_{\Lambda}$O. These parameters explain the energy spacing of many hypernuclear states except for the case of ${}^{10}_{\Lambda}$B. see text for details.

	Δ [MeV]	S_Λ [MeV]	S_N [MeV]	T [MeV]
${}^{7}_{\Lambda}$Li	0.48	-0.01	-0.40	0.03
${}^{8}_{\Lambda}$Li	0.459	-0.011	-0.433	0.027
${}^{9}_{\Lambda}$Be	0.557	-0.013	-0.549	0.029
${}^{10}_{\Lambda}$B	0.458	-0.01	-0.428	0.027
${}^{11}_{\Lambda}$B	0.488	-0.01	-0.437	0.03
${}^{12}_{\Lambda}$C	0.495	-0.012	-0.507	0.025
${}^{13}_{\Lambda}$C	0.532	-0.013	-0.545	0.027
${}^{15}_{\Lambda}$N, ${}^{16}_{\Lambda}$O	0.468	-0.011	-0.429	0.023

between the interaction in the free space and in the nuclear matter. For the OBE models, several versions of the Nijmegen models are available [10, 11, 12]. From such a point of view, the investigation of the ΛN effective interaction has been the main subject in the experiments of γ-ray spectroscopy of hypernuclei. In the following sections, detailed description for these spin-dependent parameters will be made.

The spin-spin interaction

The spin-spin interaction can be studied from the energy spacing between the 1^+ excited state and the 0^+ ground state of the $A = 4$ hypernuclei. Experiments to measure the γ rays from ${}^{4}_{\Lambda}$H and ${}^{4}_{\Lambda}$He were performed at CERN [13, 14]. Based on these results, the spin-spin interaction parameter was estimated by Millener *et al.* to be $\Delta = 0.5$ MeV [2]. However, Gibson *et al.* pointed out that the contribution from the ΛNN three-body force caused by ΛN-ΣN coupling plays an important role in the $A = 4$ hypernuclei [15], which makes it difficult to extract quantative information on the spin-spin interaction. The contribution from this effect is calculated with some of Nijmegen potentials by Akaishi *et al.* They concluded that NSC97f model gives a rather good agreement with all the measured Λ binding energis of s-shell hypernuclei (${}^{3}_{\Lambda}$H, ${}^{4}_{\Lambda}$H, ${}^{4}_{\Lambda}$He and ${}^{5}_{\Lambda}$He) by considering the coherent ΛN-ΣN coupling effect [38]. In this calculation, both of the ΛN spin-spin interaction and the coherent ΛN-ΣN coupling interaction contribute to the 0^+-1^+ energy spacings of ${}^{4}_{\Lambda}$H and ${}^{4}_{\Lambda}$He. These energy spacings are also calculated by Hiyama *et al.* with the four-body calculation [17, 18].

Although their calculation based on NSC97f also reproduces the s-shell hypernuclear level energies considerablly well, the strength of the spin-spin interaction should be studied from structure of p-shell hypernuclei where the contribution from three-body force is much smaller. In particular, the $3/2^+$-$1/2^+$ energy spacing of ${}^{7}_{\Lambda}$Li is expected to be simply explained by the spin-spin interaction. In this case, since the isospin of the core nucleus, namely ^{6}Li (1^+), is equal to zero, the contribution from the three-body force effect is expected to be small. This energy spacing is measured to be 691 keV in KEK-PS E419 [19], and the Δ parameter is derived to be 0.48 MeV by comparing the measured energy with the Millener's calculation [20].

On the other hand, the fact that no γ rays are observed for the transition between the ground-state spin doublet $(1^-, 2^-)$ of ${}^{10}_{\Lambda}$B [8, 7] suggests a smaller spin-spin interaction parameter. Fetisov *et al.* proposed $\Delta = 0.3$ MeV [21] to explain this energy spacing, which is, however, inconsistent with other hypernuclear data. Despite of recent precise measurements, it seems that the strength of the spin-spin interaction is not confirmed yet.

The spin-orbit interaction

The spin-orbit force of the NN interaction acts within a short range (∼1 fm). From the picture of the one-boson-exchange (OBE) model, the spin-orbit force is derived from the exchange of the vector and scaler mesons such as ρ, ω and σ. Since these mesons are heavy, the interaction acts within a range shorter than the size of nucleon. In such a short range, the quark model is expected to be a good agreement with experiments than the OBE model.

Generally, the spin-orbit force of the ΛN interaction can be written by a nucleon-spin-dependent term and a Λ-spin-dependent term. These terms are parameterized as S_N and S_Λ within a framework of the shell model calculation by Millener, respectively [2]. S_N can be measured by comparing nucleon-excitation energy between a hypernucleus and its core nucleus (Fig.1.1). This effect has been studied from the measured energy spacings of the ${}^{7}_{\Lambda}$Li$(5/2^+, 1/2^+)$ [4], ${}^{13}_{\Lambda}$C$(3/2^+, 1/2^+)$ [6], ${}^{12}_{\Lambda}$C$(1^-_2, 1^-_1)$ and ${}^{12}_{\Lambda}$C$(1^-_3, 1^-_1)$ [22] (Fig.1.2). S_N was derived by Millener from the energy spacings of the ${}^{7}_{\Lambda}$Li$(5/2^+, 1/2^+)$ and ${}^{13}_{\Lambda}$C$(3/2^+, 1/2^+)$ to be -0.4 MeV [3].

On the other hand, S_Λ is determined from hypernuclear fine structure. By measuring the energy spacing of ${}^{9}_{\Lambda}$Be$(5/2^+, 3/2^+)$ [5], S_Λ was determined to be -0.01 MeV. The experiment on ${}^{13}_{\Lambda}$C$(1/2^-, 3/2^-)$ [6] gave another energy spacing which is related to the Λ-spin-dependent spin-orbit force. In this case, we cannot discuss the S_Λ parameter because a Λ occupies the p-orbit. However, this energy spacing also has direct information of the Λ-spin-dependent spin-orbit force. Both of these experimental results indicate that a Λ-spin-dependent spin-orbit force is much smaller than the NN spin-orbit force.

The spin-orbit force can be considered in another formalization, namely the symmetric spin-orbit force (SLS, $\propto \mathbf{l_{N\Lambda}} \cdot (\mathbf{s_\Lambda} + \mathbf{s_N})$) and the antisymmetric spin-orbit force (ALS, $\propto \mathbf{l_{N\Lambda}} \cdot (\mathbf{s_\Lambda} - \mathbf{s_N})$). The antisymmetric spin-orbit term is peculiar to the hyperon-nucleon (YN) interaction because this term does not exist in the case

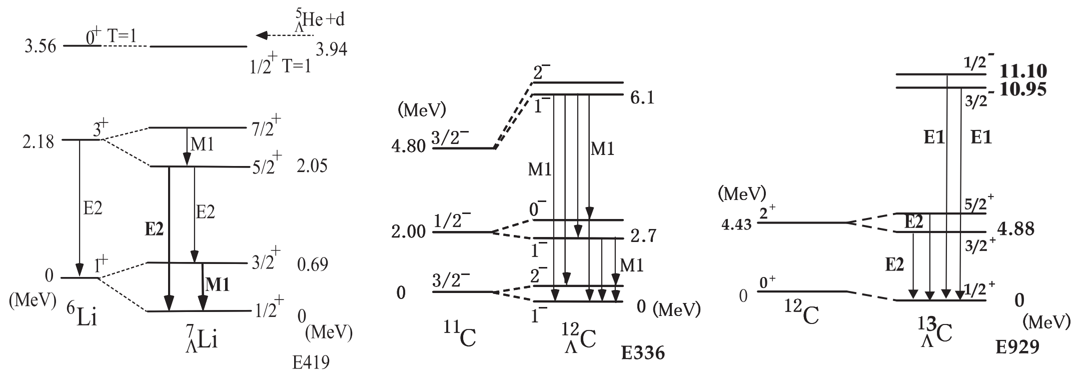

Figure 1.2: Low-lying level structure of $^7_\Lambda$Li [4], $^{12}_\Lambda$C [5] and $^{13}_\Lambda$C [6]. The nucleon-spin-dependent spin-orbit term (S_N) has been studied from the structure of these hypernuclei.

of the nucleon-nucleon (NN) interaction. As a typical difference between the quark model and the OBE model, the quark model predicts that the ALS component of the YN interaction is strong, almost comparable with the SLS one [23]. In the case of the ΛN interaction, the SLS and ALS have different signs. Therefore, the sum of the SLS and ALS components which is proportional to the Λ-spin-dependent spin-orbit force takes a small value. On the other hand, the OBE model predicts a much smaller ALS force and the SLS+ALS takes a larger value. The experimental results of $^9_\Lambda$Be and $^{13}_\Lambda$C indicate a very small Λ-spin-dependent spin-orbit force, which seems to support quark model calculations.

The tensor interaction

The tensor force is mediated by psuedoscaler mesons and vector mesons. In the case of the NN interaction, the large strength of the tensor force is mainly determined by the one-pion exchange. On the other hand, the tensor force is expected to be small in the case of the ΛN interaction because the one-pion exchange is prohibited. The tensor force is expected to be mainly determined by the kaon and the two-pion exchange in the ΛN interaction.

Since the mass of the kaon is lighter than the mesons which mediate the spin-orbit force, the tensor force is expected to act within rather longer range. Therefore, the OBE model is expected to match well with experiments. The tensor force parameter (T) was predicted to be from 0.02 MeV to 0.06 MeV using the OBE model proposed by Nijmegen group [10, 11, 12]. The energy spacings of the $^{14}_\Lambda$C, $^{14}_\Lambda$N, $^{15}_\Lambda$N and $^{16}_\Lambda$O are expected to be favorable to measure the tensor force. Experimentally, the energy spacing of $^{16}_\Lambda$O($1^-, 0^-$) was measured to determine the tensor force parameter in BNL-AGS E930('01) [7]. The result from this experiment shows that the OBE

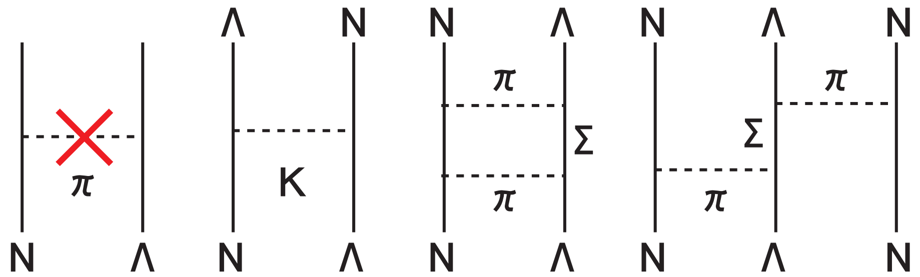

Figure 1.3: The psuedo-scaler meson exchange between a Λ and a nucleon. The one-pion exchange is forbidden in the ΛN interaction.

model explains well the tensor force of the ΛN interaction.

The ΛNN three-body interaction

The ΛN-ΣN coupling effect plays an important role in the ΛN interaction. As shown in Fig.1.3, the two-pion exchange interaction can be divided into two terms, namely two-body and three-body interaction. The former interaction can be included in the ΛN effective interaction. However, the latter interaction should be considered additionally. Akaishi *et al.* have calculated the three-body ΛN-ΣN coupling effect on A = 3, 4 and 5 systems [38]. Millener has applied this effect in the case of p-shell hypernuclei as described in §3. For instance, it is conjectured that this effect appears as the charge symmetry breaking between ${}^4_\Lambda$H and ${}^4_\Lambda$He [15]. The binding energies of ${}^4_\Lambda$He are larger than that of ${}^4_\Lambda$H by 0.35 MeV in the ground states (0^+) and 0.24 MeV in the first excited states (1^+). Although the reason for this large charge symmetry breaking is not understood yet, the ΛN-ΣN coupling might be explain the difference because there is 9 MeV difference in mass between Σ^+, Σ^0, and Σ^-.

1.2 Magnetic moment of a Λ in the nucleus

Since the constituent quark mass of hadrons may be changed by the partial restoration of chiral symmetry, the mass of hadrons in nuclear medium can be different from that in the free space. There is a theoretical prediction that the mass of the vector mesons is expected to decrease because of the partial restoration of chiral symmetry [24]. This effect was confirmed by the experiment which observed the mass modification of ρ meson in the copper nucleus [25, 26].

Our interest is what happens in the case of baryons. Nucleons cannot be used to measure the nuclear medium effect because the Pauli effect prevents us from inserting a nucleon deep inside of the nucleus to identify such effect. On the other hand, since a Λ is a different particle from the nucleon, it behaves as a probe at deep inside of a nucleus. Therefore, the nuclear medium effect of baryons can be studied by investigating properties of a Λ in hypernuclei. However, it is difficult to measure the mass modification of a Λ in the nucleus from the invariant mass measurement. To study the medium effect of baryons from hypernuclei, it is interesting to measure the magnetic moment of a Λ in the nucleus. In the free space, the magnetic moment of baryons can be well explained by a picture that each quark has a magnetic moment of a Dirac particle with a constituent quark mass. If the constituent quark mass changes in nuclear medium, the magnetic moment of baryons can also be changed.

Meanwhile, when two baryons come close to each other, the magnetic moment of the baryons in a nucleus can be changed due to the Pauli effect between quarks. This effect is called "quark exchange current" and estimated with quark cluster model to change the magnetic moment of Λ by a few percent [27]. On the other hand, the effect of meson exchange current should also be considered. In the case of a Λ particle, the meson exchange current is smaller than that of a nucleon because one-pion exchange is forbidden in the ΛN interaction (Fig.1.3). However, the exchange of a kaon and two pions were estimated to change the magnetic moment by a few percent [28]. By studying the magnetic moment of a Λ in a nucleus using several hypernuclei, these three effects may be able to be understood separately.

Experimentally, we focused on the $B(M1)$ of the Λ-spin-flip transition to study the magnetic moment. Detailed description about the experimental method will be made in § 3.

§ 2 Previous γ-ray spectroscopy experiments of hypernuclei

The γ-ray spectroscopy of hypernuclei has to be performed nearby high intensity hadron beams. It is because the cross sections for hypernuclear production and the lifetimes of the hypernuclei are too short to be separated from the beams, which require in-beam measurement. Since the experiments are difficult to perform, the number of experiments which attempted to measure γ rays from hypernuclei has not been so many. In the beginning, some γ rays from hypernuclei were measured using sodium iodide (NaI) detectors. Since 1998, after the construction of Hyperball, the energy resolution of the hypernuclear γ-ray spectroscopy was drastically improved using Ge detectors. In this section, some of the hypernuclear γ-ray spectroscopy experiments will be introduced. The experiments will be classified according to the production process of the hypernuclei, namely, the (π^+, K^+), the (K^-, π^-) and the stopped K^- reactions. These production processes are characterized by momentum transfers, cross sections and spin-flip and spin-nonflip amplitudes.

In the previous experiments of the hypernuclear γ-ray spectroscopy, the main subject was to investigate the ΛN effective interaction. The introduction will be mainly focused on the experiment related to this subject.

2.1 The γ-ray spectroscopy with the (π^+, K^+) reaction

The most remarkable feature of the (π^+, K^+) reaction is that we can produce various deeply-bound hypernuclear states. It is because of a large orbital angular momentum transfer of this production process [29]. The spin-nonflip states are selectively populated by the (π^+, K^+) reaction [30]. On the other hand, the cross section for this hypernuclear production process is smaller than the (K^-, π^-) and the stopped K^- reactions. Most of the experiments with the (π^+, K^+) reaction choose 1.05 GeV/c for the incident π^+ momentum so as to maximize the cross section of the hypernuclear production. These characteristics of this production process are mainly determined by its elementary process, namely the $n(\pi^+, K^+)\Lambda$ reaction.

The hypernuclear γ-ray spectroscopy via the (π^+, K^+) reaction was performed in the KEK-PS E419 experiment for the first time. Four γ transitions from ${}^{7}_{\Lambda}$Li including $M1$ $(3/2^+ \to 1/2^+)$ and $E2$ $(5/2^+ \to 1/2^+)$ were observed with a ^{7}Li target using Hyperball (Fig.1.4). As we have already mentioned in §1.2, the spin-spin force and the nucleon dependent spin-orbit force of the ΛN effective interactions were investigated from these measured energy spacings [4].

The shrinkage of ${}^{7}_{\Lambda}$Li was also confirmed in this experiment [19]. In the nuclear medium, a Λ in the $0s$ orbit attracts nucleons around it and causes a shrinkage of the nucleus. This effect is called "glue-like role" of Λ in the nucleus. By comparing $B(E2)$ of ${}^{7}_{\Lambda}$Li $(5/2^+ \to 1/2^+)$ with that of the core transition ^{6}Li $(3^+ \to 1^+)$, it was found that the size of ${}^{7}_{\Lambda}$Li is $19 \pm 4\%$ smaller than that of ^{6}Li [19]. Such a nuclear

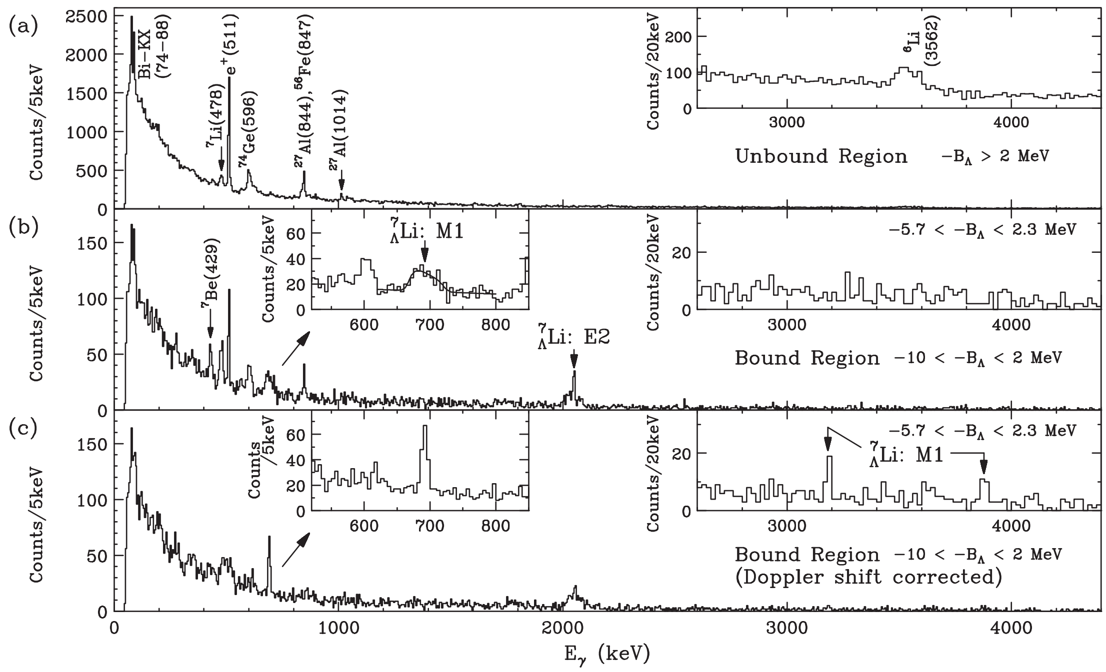

Figure 1.4: The γ-ray spectra obtained from the $^7\mathrm{Li}(\pi^+, K^+)^7_\Lambda\mathrm{Li}$ reaction [19]. The spin-spin force and the nucleon-spin-dependent spin-orbit force are investigated from this result.

shrinking effect is a general property of light hypernuclei, which was pointed out by Motoba *et al.* [31] for the first time and precisely calculated by Hiyama *et al.* [32]

The measurement of the $B(E2)$ was carried out by Doppler shift attenuation method (DSAM). The DSAM is also applied to the observed γ rays from $^{11}_\Lambda\mathrm{B}$ in the present experiment. Detailed description about the DSAM will be made in Chapter 3.

2.2 The γ-ray spectroscopy with the (K^-, π^-) reaction

The elementary cross section of the $n(K^-, \pi^-)\Lambda$ reaction is larger than that of the $n(\pi^+, K^+)\Lambda$ reaction [34]. In addition, the produced Λ prefers to remain in the nucleus because of the small momentum transfer. Therefore, the cross sections for hypernuclear states are considerably large in the (K^-, π^-) reaction. For small reaction angles with small momentum transfer, the (K^-, π^-) reaction mainly substitutes a neutron for a Λ within the same orbit in producing the hypernuclei by the orbital angular momentum transfer $\Delta L = 0$. The produced states are called substitutional states. The momentum transfer becomes large when we select large reaction angles. However, the ΔL is expected to be 0 or 1 even if we choose such a region. The spin-flip and spin-nonflip amplitudes depend on the momentum of the incident K^- in addition to the reaction angle. Many experiments are performed with $p_{K^-} = 0.7 \sim 0.9$ GeV/c in order to maximize the elementary cross section. In such a case, spin-nonflip states are selectively populated. On the other hand, when we choose larger K^--beam momenta ($p_{K^-} \simeq 1.1$ GeV/c), the spin-flip amplitude becomes large [34].

In 1998, two γ transitions around 11 MeV, which correspond to ${}^{13}_{\Lambda}$C ($1/2^- \to 1/2^+$) and ${}^{13}_{\Lambda}$C ($3/2^- \to 1/2^+$), were measured at BNL-AGS D6 beamline via the ($K^-, \pi^-\gamma$) reaction (BNL-AGS E929) [6]. The experiment was performed using the sodium iodide (NaI) detectors. The Λ-spin-dependent spin-orbit force was investigated from the energy spacing of ${}^{13}_{\Lambda}$C($1/2^-, 3/2^-$) in which a Λ occupies p-orbit.

Soon after this experiment, the γ-ray spectroscopy experiment of ${}^{9}_{\Lambda}$Be was performed at the same beamline but using the Ge detector array, Hyperball (BNL-AGS E930('98)). The energy spacing of the Λ spin-flip doublet ($3/2^+, 5/2^+$) was measured and the Λ-spin-dependent spin-orbit force was investigated for a Λ in the s-shell [5].

Three years later, in order to determine the strength of the tensor force, γ rays from ${}^{16}_{\Lambda}$O were measured with almost the same experimental setup as of the γ ray measurement of ${}^{9}_{\Lambda}$Be (BNL-AGS E930('01)). This result indicates that the strength of the tensor force which is calculated from the meson exchange model is almost consistent with the experiment. The data with a ^{10}B target was also acquired but no γ rays from ${}^{10}_{\Lambda}$B were observed in this experiment. This result will be described in Chapter 6.

γ rays from hyperfragments were also investigated using the (K^-, π^-) reaction. By performing experiments with the incident K^- momentum $p_{K^-} = 0.7 \sim 0.9$ GeV/c, the kinematics results in a very small recoil momentum of a Λ ($q_\Lambda = 40 \sim 70$ MeV/c at $\theta = 0°$). Then, the substitutional states are dominantly produced by the (K^-, π^-) reaction even in the highly excited states of hypernuclei. Since such states decay into other hypernuclei, it is convenient to use the (K^-, π^-) reaction in measuring γ rays from the hyperfragments. Some of the γ transitions from hyperfragments are measured in the BNL-AGS E930('01) [7].

2.3 The γ-ray spectroscopy with the stopped K^- reaction

The K^- absorption reaction was the only process available for the Λ hypernuclear production in 1960's. In recent years, the stopped K^- reaction was revived to utilize the merit of large production yields of various hyperfragments. This hypernuclear production process has a larger momentum transfer than the case of the in-flight (K^-, π^-) reaction. However, the momentum transfer is smaller than the case of the (π^+, K^+) reaction [29]. The angular momentum transfer is also large because K^- in the atomic orbit brings larger angular momentum into produced hypernuclei.

A γ-ray spectroscopy experiment via the stopped K^- reaction using Hyperball was performed with the ^{7}Li, ^{9}Be, ^{10}B, ^{11}B and ^{12}C targets at KEK in 2002. From ^{10}B, ^{11}B and ^{12}C targets, the ${}^{7}_{\Lambda}$Li ($5/2^+ \to 1/2^+$) transition was observed. According to the measured production rate, the stopped K^- method seems to be a useful tool for γ-ray spectroscopy of hypernuclei, particularly by using γ-γ coincidence technique in the future.

§ 3 The γ-ray spectroscopy of ${}^{11}_{\Lambda}$B

The purpose of the γ-ray spectroscopy of ${}^{11}_{\Lambda}$B consists of two subjects. The first subject is to investigate the spin-dependent forces of the ΛN effective interactions. As mentioned in the previous sections, the individual strengths of the four parameters have been already determined from experimental results using Hyperball. However, some experiments imply that there remains inconsistency and a cross check of these values using other hypernuclear data is still necessary. γ rays from ${}^{11}_{\Lambda}$B can give us additional information on the ΛN effective interaction.

Another subject is to measure the g-factor of Λ in a nucleus. The ${}^{11}_{\Lambda}$B ($3/2^+ \rightarrow 1/2^+$) transition is considered to be the best Λ-spin-flip $M1$ transition in which we can measure the $B(M1)$ with Doppler shift attenuation method within a reasonable beamtime.

3.1 Consistency check of the ΛN effective interaction

${}^{11}_{\Lambda}$B is a good object to verify the four spin-dependent parameters because many bound states are expected to exist below the particle decay threshold into ${}^{10}_{\Lambda}$Be and a proton. As shown in Table 1.1, these parameters for ${}^{11}_{\Lambda}$B are obtained by using the results of the previous experiments as

$$\Delta = 0.488,\ S_{\Lambda} = -0.01,\ S_N = -0.437,\ T = 0.03 \text{ [MeV]}. \tag{1.5}$$

The structure of ${}^{11}_{\Lambda}$B is considered predominantly by weak-coupling scheme between a Λ and a core nucleus, ^{10}B. Consequently, the spin component of the core-nuclear wave function is important to understand the energy spacings from four spin-dependent parameters (see §1.2). In order to understand the general features of electromagnetic transitions in the most complicated p-shell nucleus, the odd-Z odd-N nucleus ^{10}B, Kurath performed a shell-model calculation by considering that the low-lying ^{10}B states are predominantly of [42] symmetry for which the spin and isospin values can only be $S = 1$, $T = 0$ or $S = 0$, $T = 1$ [35]. Barker modified this shell model interaction parameters to give a better agreement with experiments [36]. Recently, Millener improved the Barker I wave function by using typical effective g-factors instead of the bare g-factors (see Appendix B). Then, the wave function is used to describe the spin component of the states in ${}^{11}_{\Lambda}$B [3].

Figure 1.5 shows the expected level structure of ${}^{11}_{\Lambda}$B, which is calculated by Millener using the parameters in Eq.(1.5) [3]. In his shell-model calculation, excitation energies, γ-ray branching ratios and lifetimes of ${}^{11}_{\Lambda}$B bound states are estimated.

Then, based on his calculation, we found that nine γ-ray transitions are expected to be observed within a reasonable beamtime at KEK. In order to observe these γ rays, we performed an experiment for the γ-ray spectroscopy of ${}^{11}_{\Lambda}$B in KEK-PS E518 (see Chapter 2 for details). Among these γ rays, the energy spacing of the $M1(3/2^+_1 \rightarrow 1/2^+_1)$ transition of which $B(M1)$ we are going to measure is calculated to be

$$\begin{aligned} &E(3/2^+_1) - E(1/2^+_1) \\ &\qquad = 1.209\Delta + 0.282 S_\Lambda + 0.296 S_N - 0.345 T + \Delta E'_{core} + \Lambda\Sigma \\ &\qquad = 653 \text{ [keV]}. \end{aligned} \tag{1.6}$$

Here, the coefficient of each parameter is determined by the LS component of the wave functions of the initial and final states in ${}^{11}_{\Lambda}$B (see Appendix A). $\Lambda\Sigma$ expresses the ΛN-ΣN coupling effect and is estimated to be 56 keV. As mentioned in §1, the ΛN-ΣN coupling effect in the s orbit was calculated by Akaishi *et al.* through G-matrix method [38]. To extend this calculation to p-shell hypernuclei, Millener took the YNG interaction of Akaishi for the ΛN-ΣN coupling and performed shell-model calculation with a basis of $p_N s_\Lambda$ and $p_N s_\Sigma$ configurations [37]. $\Delta E'_{core} = 147$ keV is originated from the configuration mixing of two $3/2^+$ states in ${}^{11}_{\Lambda}$B, whose amplitude is estimated to be

$$\begin{aligned} |3/2^+_1\rangle &= 0.883\ |1^+_1 \times s_\Lambda\rangle + 0.112\ |1^+_2 \times s_\Lambda\rangle + 0.004\ |2^+_1 \times s_\Lambda\rangle \\ |3/2^+_2\rangle &= 0.116\ |1^+_1 \times s_\Lambda\rangle + 0.866\ |1^+_2 \times s_\Lambda\rangle + 0.016\ |2^+_1 \times s_\Lambda\rangle. \end{aligned} \tag{1.7}$$

The energy spacing of the $M1(3/2^+_1 \rightarrow 1/2^+_1)$ transition is expected to have a large contribution from the spin-spin interaction.

Meanwhile, the energy spacing of an $E2(1/2^+_1 \rightarrow 5/2^+_1)$ transition, which is expected to have the largest yield, is calculated as

$$\begin{aligned} &E(1/2^+_1) - E(5/2^+_1) \\ &\qquad = -0.243\Delta + 1.234 S_\Lambda - 1.090 S_N - 1.627 T + \Delta E_{core} + \Lambda\Sigma \\ &\qquad = 1020 \text{ [keV]}. \end{aligned} \tag{1.8}$$

Here, ΔE_{core} is the measured energy spacing of the core nuclear levels (718.3 keV) and $\Lambda\Sigma$ is calculated to be -4 keV. In this case, the energy spacing is mainly determined by the nucleon-spin-dependent spin-orbit interaction (S_N).

The energy spacings between the other states are also expressed in terms of these four parameters. We can verify the parameters by comparing the measured and the expected energy spacings.

3.2 The g-factor of a Λ in nuclear medium

Experimentally, it is difficult to measure the magnetic moment of a Λ in the nucleus directly. For many radionuclide, it is a powerful method to observe the nuclear magnetic resonance for investigation of the magnetic moment. However, we cannot use such a method because the lifetime of hypernuclei is too short.

The g-factor of a Λ in nuclear medium can be studied from the probability of a Λ-spin-flip $M1$ transition ($\Gamma(M1)$). Generally, the magnetic dipole operator $\boldsymbol{O}$ can be expressed in terms of orbital angular momentum of protons and intrinsic spin of each nucleon and a Λ. In the case of hypernuclei, this operator can be divided into a core part and a Λ part, and denoted as follows,

$$\begin{aligned}
\boldsymbol{O} &= \boldsymbol{O_{orbit}} + \boldsymbol{O_{spin}} \\
&= \sum_{protons} (g_l \boldsymbol{l_p} + g_s \boldsymbol{s_p}) + \sum_{neutrons} g_n \boldsymbol{s_n} + g_\Lambda \boldsymbol{s_\Lambda} \\
&= g_c \boldsymbol{J_c} + g_\Lambda \boldsymbol{s_\Lambda} \\
&= \boldsymbol{O_c} + \boldsymbol{O_\Lambda}.
\end{aligned} \tag{1.9}$$

Here, g_l, g_s, g_n, g_Λ and g_c are effective g-factors of proton-orbit, proton-spin, neutron-spin, Λ-spin and core nucleus respectively. These are expressed in terms of nuclear magneton (μ_N).

By assuming a weak coupling between a Λ and the core nucleus, the $\Gamma(M1)$ can be expressed as [1, 39],

$$\begin{aligned}
\Gamma(M1) &= \alpha_1 E_\gamma^3 \left(\frac{1}{2J_i+1}\right) \sum_{J_i^z, J_f^z} |\langle \phi_f | \, \boldsymbol{O}_{M1,\mu} | \phi_i \rangle|^2 \\
&= \alpha_1 E_\gamma^3 \left(\frac{1}{2J_i+1}\right) |\langle \phi_f \| \, \boldsymbol{O}_{M1} \| \phi_i \rangle|^2 \\
&= \alpha_1 E_\gamma^3 (2J_f+1) \\
&\times \left(\langle J_c \| \, \boldsymbol{O_c} \| J_c \rangle \begin{Bmatrix} J_c & J_f & \frac{1}{2} \\ J_i & J_c & 1 \end{Bmatrix} + (-1)^{J_i - J_f} \langle 1/2 \| \, \boldsymbol{O_\Lambda} \| 1/2 \rangle \begin{Bmatrix} \frac{1}{2} & J_f & J_c \\ J_i & \frac{1}{2} & 1 \end{Bmatrix} \right)^2
\end{aligned} \tag{1.10}$$

where J_i, J_f and J_c represent the total angular momentum of the initial, final and core states respectively. $\langle \phi_f \| \boldsymbol{O}_{M1} \| \phi_i \rangle$ is the reduced matrix element defined with the Wigner-Eckart theorem. Here, α_1 is a numerical constant for $M1$ transition and turns out to be

$$\alpha_1 = 1.76 \times 10^{13} \ [\mathrm{sec}^{-1} \mathrm{MeV}^{-3}]. \tag{1.11}$$

On the other hand, the magnetic moment ($\mu(j)$) of a system with the angular momentum j is given by

$$\mu(j) = jg = \sqrt{\frac{3}{4\pi} \cdot \frac{2j}{(2j+1)(2j+2)}} \langle j \| \boldsymbol{O} \| j \rangle. \tag{1.12}$$

Then, Eq.(1.10) can be written in the form,

$$\begin{aligned} B(M1) &= \frac{3}{4\pi}\cdot\frac{3}{2}\,(2J_f+1)\begin{Bmatrix} J_i & J_f & 1 \\ \frac{1}{2} & \frac{1}{2} & J_c \end{Bmatrix}^2 (g_c-g_\Lambda)^2 \\ &= \frac{3}{8\pi}\cdot\frac{2J_f+1}{2J_c+1}\,(g_c-g_\Lambda)^2[\mu_N^2]. \end{aligned} \tag{1.13}$$

Here, we have used the relation of $J_i = J_c \pm 1/2$ and $J_f = J_c \mp 1/2$ for the Λ-spin-flip $M1$ transition, respectively. Note that reduced transition probability ($B(M1)$) is defined by using the reduced matrix element as

$$B(M1) = \frac{1}{2J_i+1}\left|\langle\phi_f\|\,\boldsymbol{O}_{M1}\|\phi_i\rangle\right|^2. \tag{1.14}$$

Equation (1.13) shows that the g-factor of a Λ in the nucleus (g_Λ) can be derived by measuring the $B(M1)$ and the g-factor of the core nucleus (g_c).

The $B(M1)$ value can be measured with Doppler shift attenuation method. If γ ray emission is fast enough after the production of the hypernucleus, the width of the observed γ ray peak is broadened by Doppler effect. The lifetime of the excited state is obtained by comparing the observed peak shape with that of a Monte Carlo simulation. This method can be used when the lifetime of the excited state is comparable with the stopping time of the hypernucleus. Detailed description will be made in Chapter 3. In the previous experiment with Hyperball, this method was applied to measure the $B(E2)$ of ${}^{7}_{\Lambda}$Li ($5/2^+ \rightarrow 1/2^+$) transition (see §2.1).

§ 4 The γ-ray spectroscopy of ${}^{10}_{\Lambda}$B

The purpose of the γ-ray spectroscopy of ${}^{10}_{\Lambda}$B was to measure the energy spacing of the ground-state spin doublet ($2^-, 1^-$). The γ rays from ${}^{10}_{\Lambda}$B were attempted to measure in the previous experiment by Chrien *et al.* at BNL [8] but the transition between the ground-state spin doublet was not observed. This result is inconsistent with the theoretical calculations by Millener where the energy spacing was calculated using the parameters in Table 1.1 as

$$\begin{aligned} E(2_1^-) - E(1_1^-) &= 0.578\Delta + 1.414S_\Lambda + 0.014S_N - 1.068T + \Lambda\Sigma \\ &= 197\ [\text{keV}]. \end{aligned} \tag{1.15}$$

Here, $\Lambda\Sigma$ expresses the ΛN-ΣN coupling effect of -15 keV. However, the result of the previous experiment was statistically insufficient. Consequently, we have performed an experiment to confirm in the BNL-AGS E930('01) as discussed in Chapter 6.

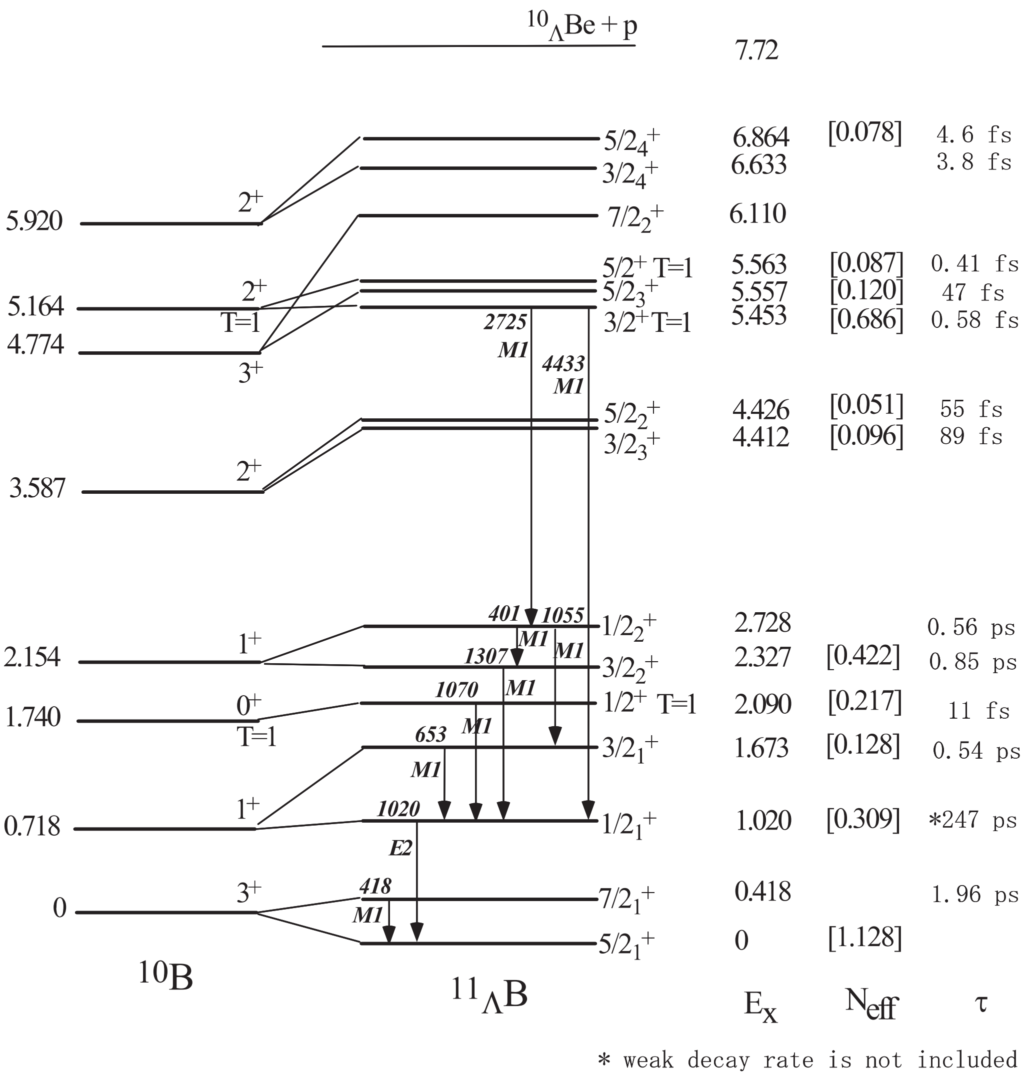

Figure 1.5: Calculated level scheme of $^{11}_{\Lambda}$B by Millener [3]. Calculated excitation energy, cross section, and lifetime of each state are listed on the right side. In total, nine γ transitions are expected to be observed in KEK-PS E518.

Chapter 2

γ-ray spectroscopy of ${}^{11}_{\Lambda}$B — Experimental Setup

§ 1 Overview

The experiment to investigate γ rays from ${}^{11}_{\Lambda}$B was performed at the north experimental hall of the 12-GeV proton synchrotron (PS) in the High Energy Accelerator Research Organization (KEK), with the K6 beamline, the Superconducting Kaon Spectrometer(SKS), and Hyperball. The $(\pi^+, K^+\gamma)$ reaction was used to produce bound states of ${}^{11}_{\Lambda}$B in this experiment. Incident and scattered particles were detected for every pion and kaon by the magnetic spectrometers at the K6 beamline. Using the measured momenta of the pion and kaon, the mass of ${}^{11}_{\Lambda}$B is reconstructed and the bound states region of ${}^{11}_{\Lambda}$B is tagged. In order to observe the γ rays from tagged events, a germanium (Ge) detector array, Hyperball, is placed around the target.

In this section, detailed explanation of the experimental setup will be made.

§ 2 KEK-PS K6 beamline

At the KEK-PS K6 beamline, we used 1.05 GeV/c π^+ meson as a secondary beam. This momentum was selected so as to maximize the cross section of the hypernuclear production (see Chapter 1).

Schematic view of the K6 beamline is shown in Fig.2.1. Protons which were accelerated up to 12 GeV with synchrotron was irradiated onto a platinum (Pt) target(ϕ 6×60 mm). The primary proton beam was extracted for extraction period of 1.5 seconds in each 4.0 seconds synchronized to the KEK-PS operation cycle. The intensity of the primary protons was typically 1.2×10^{12} protons/spill at the production target of the K6 beamline.

The secondary beam produced at the Pt target was derived to the experimental target using the two dipole magnets (D1, D2), ten quadrupole magnets (Q1-Q10), a sextuple magnet (SX), an electrostatic separator (DC separator) with two correction magnets (CM1, CM2), and four slits. The slits were installed between D1 and Q1 (acceptance slit), between Q2 and Q3 (intermediate focus slit), between SX and Q5

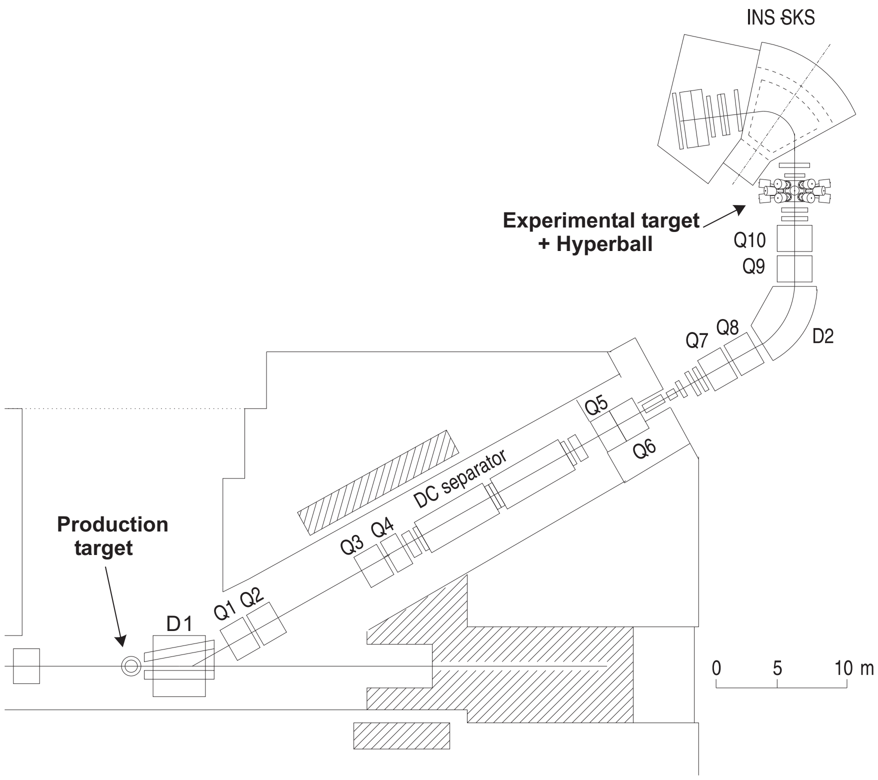

Figure 2.1: Schematic view of the KEK-PS K6 beamline.

(momentum slit), and between Q6 and Q7 (mass slit). Pions in the secondary beam was selected by its velocity and momentum. Then, the beam was focused on the experimental target. The π^+ beam intensity was typically 3.5 $\times 10^6$ π^+/spill.

§ 3 Magnetic spectrometer system of K6 beamline

In this section, the magnetic spectrometer system of the K6 beamline will be discribed. The spectrometer system can be divided into two parts, namely the spectrometer for the incident particle and that for the scattered particle. More detailed description of the K6 beamline and the SKS can be found in Ref.[40].

3.1 Spectrometer for incident particle

Figure 2.2 is a schematic view of the spectrometer for the incident pions. This spectrometer consists of a QQDQQ magnet system with four sets of drift chambers

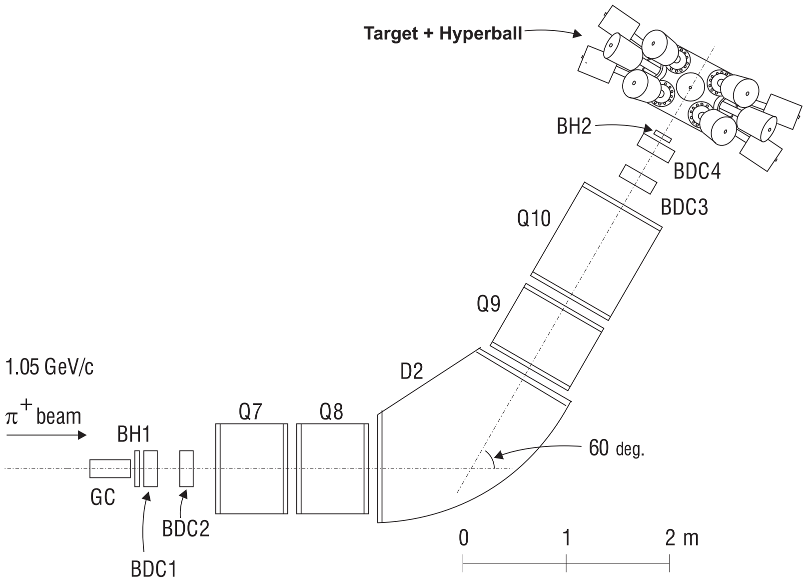

Figure 2.2: Schematic view of the spectrometer for the incident pions.

(BDC1,2,3,4) and trigger counters (GC, BH1, and BH2). The specification of the spectrometer system is shown in Table 2.1. The spectrometer is designed in order to realize a momentum resolution of 0.1%(FWHM) at around 1 GeV/c.

Trigger counters

The magnets, the slits, and the separator of the K6 beamline were tuned in order to deliver pure and high intensity 1.05 GeV/c π^+ beam onto the experimental target. Although, there still remains some contamination of positrons and protons in the beam at the target. Trigger counters were set so as to remove such unnecessary particles.

Contamination of positrons in the secondary beam was typically 20 % [42]. A Freon gas Čerenkov counter (GC) removes positrons at the trigger level. The refractive index of the Freon is 1.00245 and the positron rejection efficiency was better

Table 2.1: The specification of the beam line spectrometer.

Momentum resolution	0.1 % (FWHM) at 1 GeV/c
Momentum bite	$\pm$3 %
Maximum central momentum	1.2 GeV/c
Bending angle	60°

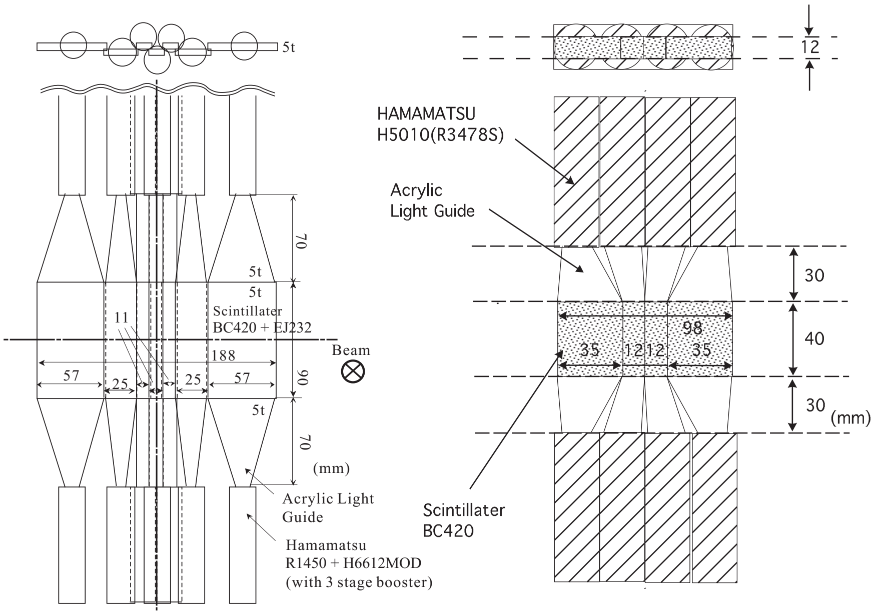

Figure 2.3: Schematic view of BH1 and BH2.

than 99.9%.

The BH1 and BH2 are segmented plastic scintillation counters. The number of segments and the size of these counters were determined to avoid problems caused by high counting rate. By requiring timing coincidence between these counters, proton contamination of $\sim 10\%$ in the pion beam was rejected at the trigger level. Schematic view of the BH1 and BH2 is shown in Fig.2.3.

Drift chambers

At the K6 beamline, four sets of drift chambers (BDC1-4) were placed to measure the trajectory of the incident particles. BDC1 and 2 were placed upstream of the magnet system, and BDC3 and 4 were placed downstream of the magnet system (Fig.2.2).

Figure 2.4 shows a schematic drawing of the drift chamber. These chambers were designed so as to operate under the condition of high counting rate (see §2). They have the same structure and each of six planes ($xx'uu'vv'$) has 48 sense wires with 5mm spacings. Cathode planes were put between the wire planes. The direction of sense wires in the x and x' planes were parallel to the vertical axis, while the uu' and vv' planes were tilted $\pm 15°$ from the vertical axis. Positions of the wires in the x, u, and v planes were 2.5 mm shifted with the corresponding wires in the x', u', and v' planes in order to solve left-right ambiguities (Fig. 2.5) [42]. Gold-plated tungsten wire of 12μmϕ was used for sense wires and that of 75μmϕ was for potential wires. The spatial resolution of the BDC's was about 300 μm (RMS) and the detection efficiency of each plane was about 99%. The gas mixture was Ar(76%)+C_4H_{10}(20%)+Methylal(4%).

Table 2.2: The specification of SKS.

Momentum resolution	0.1 % (FWHM) at 0.72 GeV/c
Momentum bite	$\pm$10 %
Maximum central momentum	1.1 GeV/c
Bending angle	100° for the central trajectory
Solid angle	100 msr
Flight path	$\sim$ 5 m for the central trajectory

3.2 Spectrometer for outgoing particle (SKS)

We used the superconducting kaon spectrometer (SKS) to measure the outgoing kaon. The spectrometer was constructed to realize both high resolution and large acceptance. As summarized in Table 2.2, SKS has a good momentum resolution of 10% at around 0.72 GeV/c and covers 100 msr. For the (π^+, K^+) reaction, the magnet was excited at 2.2 T (272 A). In order to avoid a loss of kaon from decay, a flight path length is kept as short as possible (typically 5 m).

SKS consists of a superconducting dipole magnet with four sets of drift chambers (SDC1,2,3,4) and trigger counters (TOF, AC1, AC2, and LC). Schematic view of the spectrometer is shown is Fig.2.6.

Trigger counters

Trigger counters were set to choose kaons in the scattered particles. There were 15-segmented plastic scintillation counters (TOF), two stages of silica aerogel Čerenkov counters (AC1,2) and 14-segmented Lucite Čerenkov counters (LC).

The TOF counters were used to measure the time-of-flight of the scattered particle. A typical timing resolution between BH2 and TOF was about 200 psec in rms.

The silica aerogel Čerenkov counters whose refractive index was 1.06 were used to reject pions in the scattered particles at the trigger level. The threshold momenta correspond to 0.4 GeV/c for pions and 1.8 GeV/c for kaons, respectively.

LC is a threshold-type Lucite Čerenkov counter whose refractive index was 1.49. There were many protons in the scattered particles, which came not only from a target but also from other materials. LC rejects such protons whose momenta are less than 0.85 GeV/c at the trigger level.

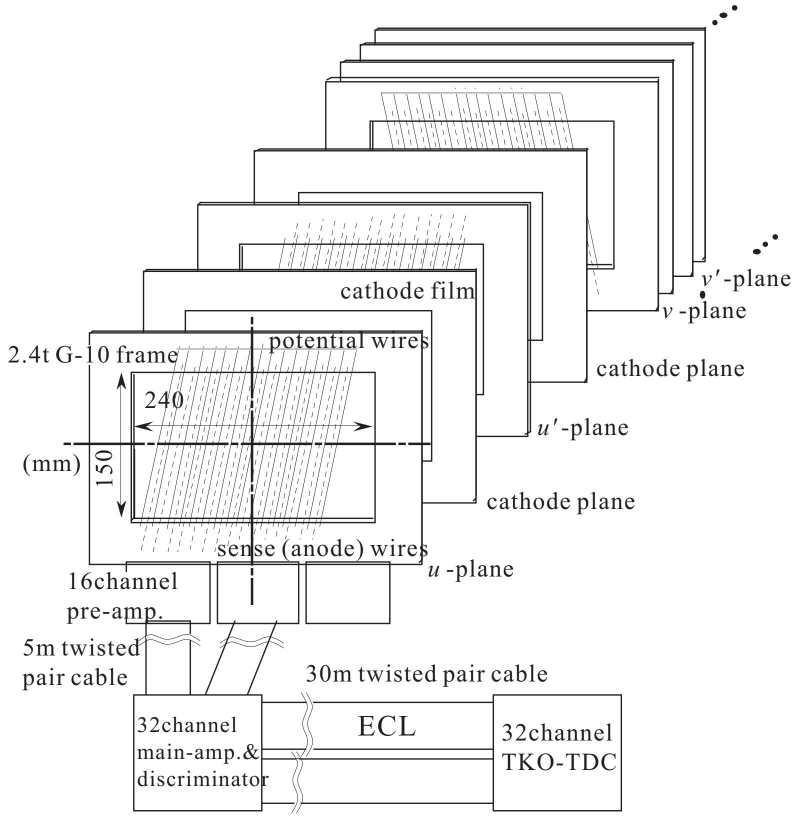

Figure 2.4: Schematic drawing of the drift chamber and the read-out system for the incident particle.

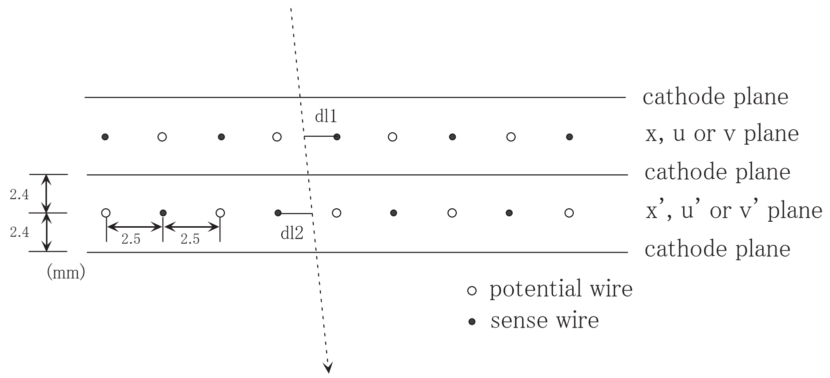

Figure 2.5: Cell structure of the drift chambers for the incident particle.

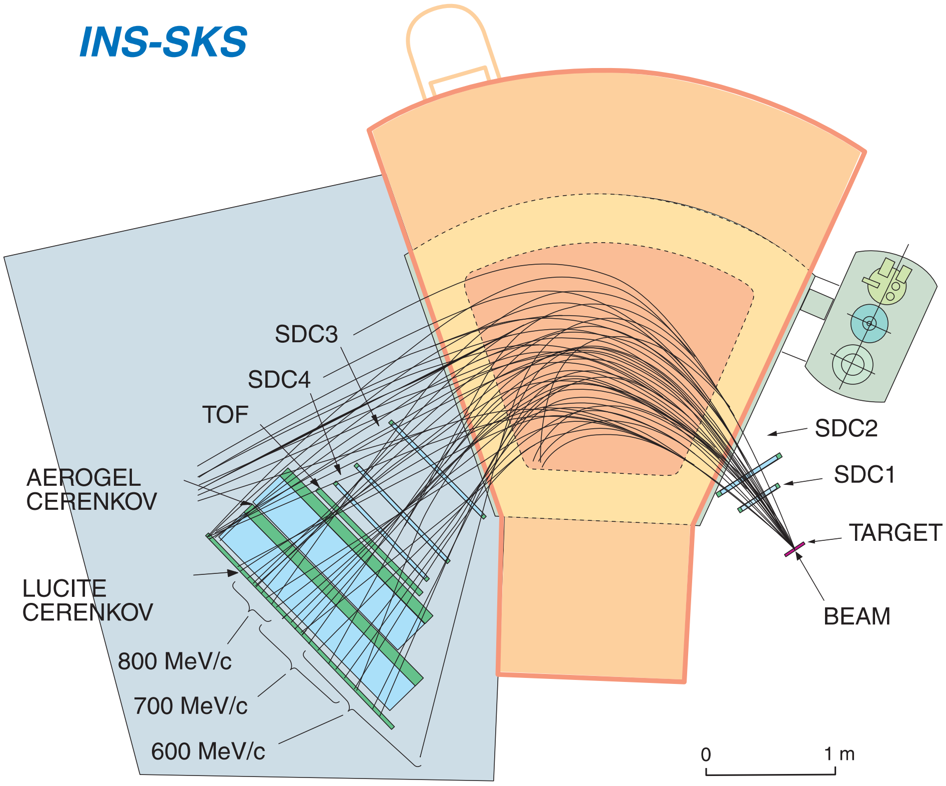

Figure 2.6: Schematic view of SKS.

Drift chambers

SDC1,2 were set at the upstream of the magnet and SDC3,4 were at the downstream. These chambers were used to measure the trajectory of the scattered particles. SDC1,2 had almost the same structure as BDC's but SDC1 had only two planes ($uu'vv'$) and SDC2 had 80 sense wires per a plane. SDC3,4 had a larger drift space ($\pm$ 21mm) than the other drift chambers of this spectrometer system. It is because we do not have to mind the counting rate at the downstream of the SKS magnet. The SDC3 had four planes of sense wires ($xx'yy'$). On the other hand, SDC4 was divided into two chambers, namely SDC4X and SDC4Y. Each of the chamber had 6 planes of sense wires. The wire configuration of SDC4 is shown in Fig.2.7. In SDC3,4, gold-plated tungsten wire of 20 μmϕ was used for sense wires and that of 80 μmϕ was for potential wires. The gas mixture was Ar(50%)+C_4H_{10}(50%). Specification of the drift chambers are summarized in Table 2.3.

Table 2.3: Specification of the drift chambers.

Name	Effective area (cm^2)	Maximum drift length (mm)	Planes	Resolution (μm in rms)
BDC1,2,3,4	$24^W\times 15^H$	2.5	$xx'uu'vv'$	300
SDC1	$24^W\times 15^H$	2.5	$uu'vv'$	300
SDC2	$40^W\times 15^H$	2.5	$xx'uu'vv'$	300
SDC3	$100^W\times 100^H$	21	$xx'yy'$	250
SDC4	$100^W\times 100^H$	21	$x\times 6, y\times 6$	250

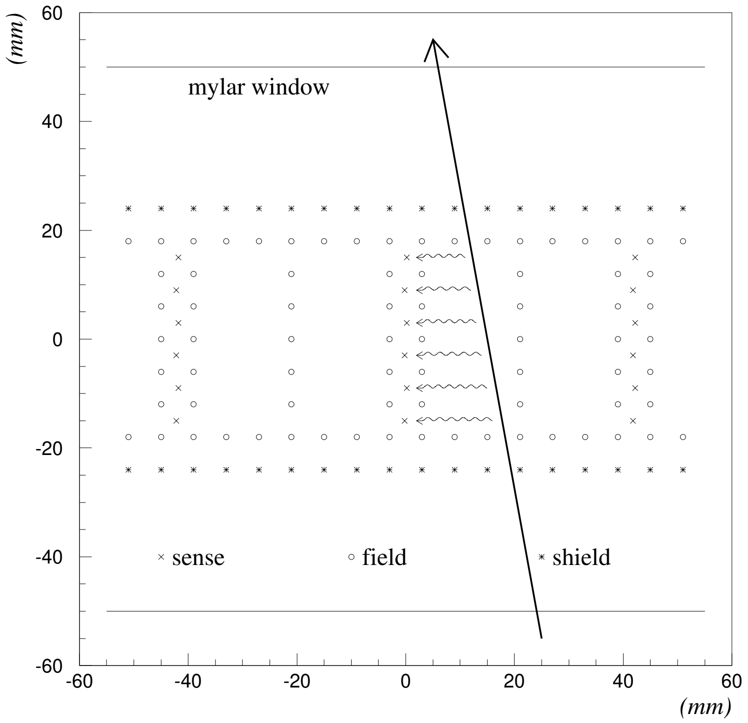

Figure 2.7: Wire configuration of SDC4.

§ 4 Hyperball

In order to measure γ rays from hypernuclei, we used the germanium (Ge) detector array, Hyperball, which consists of 14 Ge detectors (Fig.2.8). Each Ge detector is surrounded by BGO scintillation counters equipped to suppress background. Fast readout electronics are also necessary to use Ge detectors under the experimental condition of the hypernuclear γ-ray spectroscopy. Hyperball covers 15 % of a solid angle for a point γ-ray source. Typical distance from the target to the surface of the Ge crystals facing the target was 15 cm. As described in the next chapter, the photo-peak efficiency of the Ge detectors is about 2 % for the 1-MeV γ ray from a point source. In this section, the specification of Hyperball will be described.

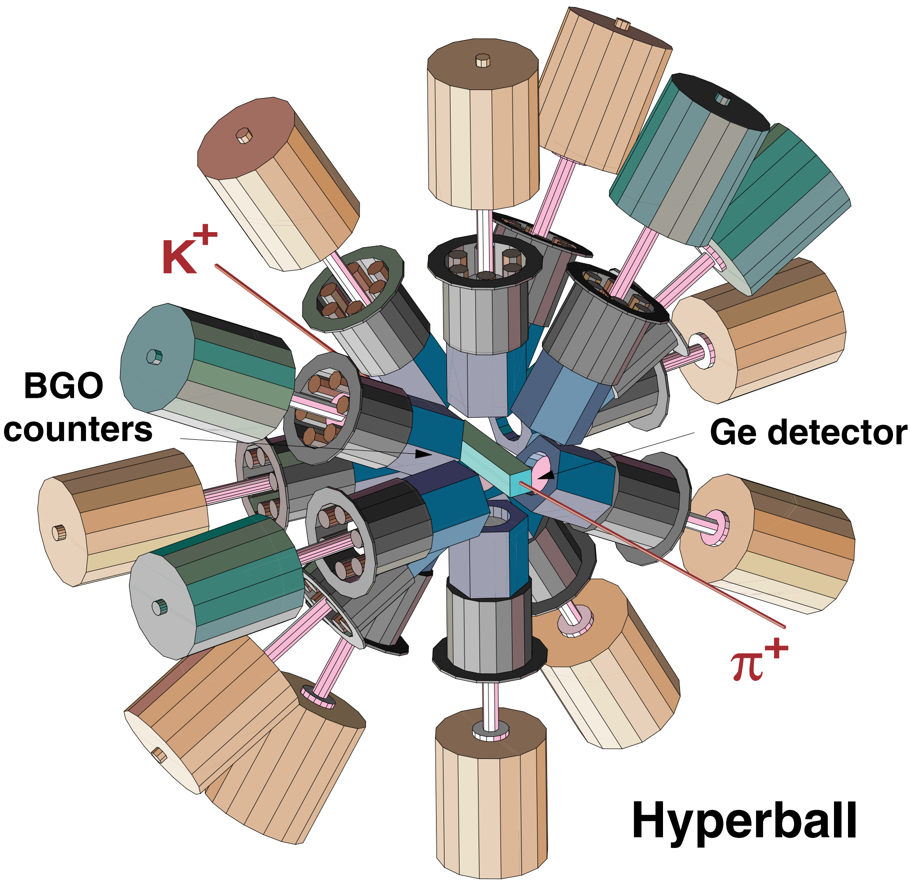

Figure 2.8: Schematic drawing of Hyperball.

4.1 Germanium detectors for the hypernuclear experiments

There are some difficulties in using Ge detectors for the hypernuclear γ-ray spectroscopy. The experiments are performed with meson beams, such as π^+ or K^-, where a typical beam intensity is of the order of 10^6 particles per a second and the beam momentum is 0.7 – 1.1 GeV/c. In such a situation, the beam particles and their halo, which are scattered on the thick target, produce high counting rate and high energy-deposit rate on Ge detectors.

In the present experiment, the counting rate of a Ge detector was typically from 10 kHz to 70 kHz. The counting rate was varied according to position of the Ge detectors, thickness of the target and the beam intensity. When a high energy beam particle is scattered on the target and penerates the Ge detectors, it gives an energy deposit of the order of 50 MeV. On the other hand, the energy range of γ rays which we aim to measure is around 1 MeV. The wide energy range by γ rays and charged particles requires us to use reset-type preamplifiers with a low gain as described later. Typically, the energy deposit rate of a Ge detector were 200–800 GeV per a second. Fast shaping amplifiers with gated integrators were also used to overcome such problems.

Germanium detectors

We have 15 high-purity germanium detectors (HPGe) which can be used for the Hyperball system. Ten of them were fabricated by ORTEC [43] and five were by Eurisys Measures [44]. The ORTEC detectors equipped a beryllium window of 0.5 mm thick so as not to attenuate the low energy γ rays. On the other hand, Eurisys detectors equipped an aluminum window of 2.0 mm thick. Schematic view of each detector is shown in Fig. 2.10.

Every Ge detector had reverse-electrode coaxial-type crystal whose relative efficiency was 60 %. Here, relative efficiency is normalized by the efficiency of a sodium iodidide (NaI) scintillation counter of 3"ϕ $\times$3", where the efficiency is measured using the 1.33-MeV γ ray emitted from ^{60}Co source which is placed at 25 cm distance. The size of each crystal is typically 70 mmϕ $\times$ 70 mm. As shown in Fig.2.9, the p-type electrode (ion-implanted boron) is located

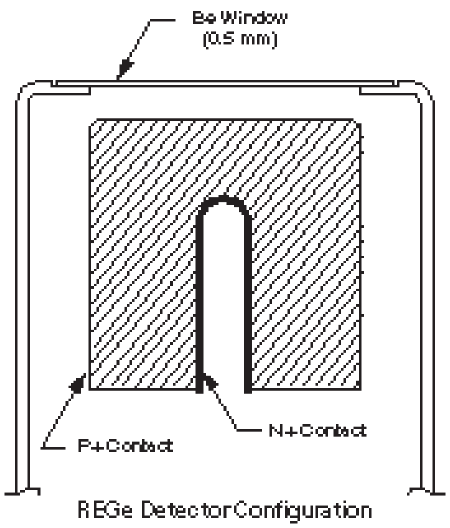

Figure 2.9: The crystal of reverse-electrode coaxial type Ge detector. p-type electrode is on the outside.

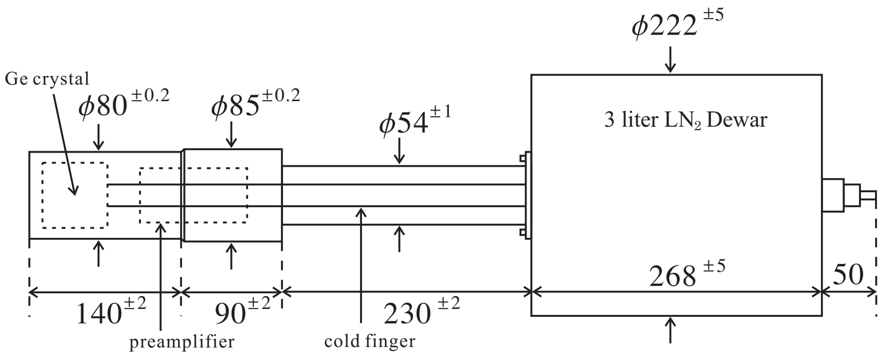

Figure 2.10: Schematic drawing of the Ge detectors for the Hyperball system fabricated by Eurisys Measures.

on the outside of the crystal and the n-type contact (diffused lithium) is on the inside, which are opposite from the conventional coaxial detector. There are two advantages in this electrode arrangement, namely, window thickness and radiation damage resistance. The ion-implanted contact can be extremely thin (0.3 μm) compared to a lithium-diffused contact (0.5 mm). Therefore, the detector achieves better efficiency for the low energy γ rays. Properties of the detector on the radiation damage resistance will be described in the following paragraph.

Radiation damages

In our experimental condition, the radiation damage is mainly due to fast neutrons from targets. The damage increases the hole-capture rate in the effective volume of Ge crystal. Therefore, as the damage increases, the observed peak shape tends to have a low-energy tail. In the case of the reverse-electrode coaxial-type crystal, the hole is collected to the electrode which is located at the outer side of the crystal. It decreases the averaged drift length of the hole and the effect of the radiation damage can be minimized. Figure 2.11 shows the peak shape difference between at the beginning and the end of the experiment for the γ ray from ^{60}Co source.

Once the Ge crystal is warmed up to the normal temperature after the crucial radiation damage, the damage is increased by, so called, reverse annealing effect and the peak becomes to have terrible low-energy tail with which the detector cannot be used for the experiment. To avoid such a trouble, Ge detectors have to be kept at low temperature using liquid nitrogen. Figure 2.11 is the spectrum obtained before the reverse annealing. The radiation damage can be almost recovered by annealing the crystal but the damage is accumulated to the crystal.

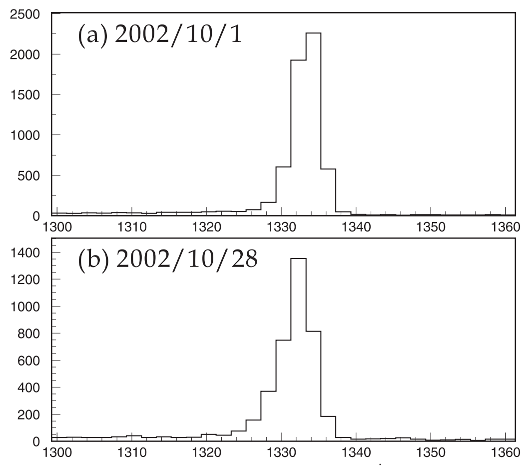

Figure 2.11: The peak shape difference between at (a) the beginning and (b) the end of the experiment. Radiation damage causes a low-energy tail in the spectrum (b).

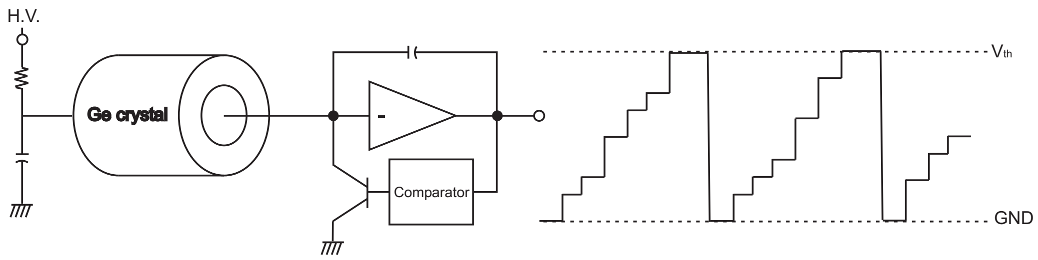

Figure 2.12: Transistor reset-type preamplifier. The comparator turns on the transistor to reset the preamp when output reaches the upper limit of its range (V_{th}).

Reset-type preamplifier

Traditionally, resistor-feedback-type preamplifier has been used for Ge detectors. However, it cannot be used under a high counting rate and a high energy deposit rate because the amplifier output will be kept saturating if the gain is optimized to realize a reasonable energy resolution. In the case of the transistor-reset-type preamplifier, a comparator turns on a transistor switch to reset the preamplifier when the output signal voltage reaches the upper limit of its range (Fig.2.12). It takes only a few microseconds to reset the charge but the dead time per a reset is typically 15 μsec because a large fraction of the charge by the reset affects the following main-amplifier. The gain of our preamplifier is much lower than the conventional type in order to reduce the reset rate. The output signal of the preamplifier for the γ rays from ^{60}Co (1.17, 1.33 MeV) was typically 40 mV. In this experiment, the reset rate for one Ge detector is typically 1.5–5 kHz, which corresponds to the dead time of 2–8 %. The threshold for a reset was set to be typically 6 V.

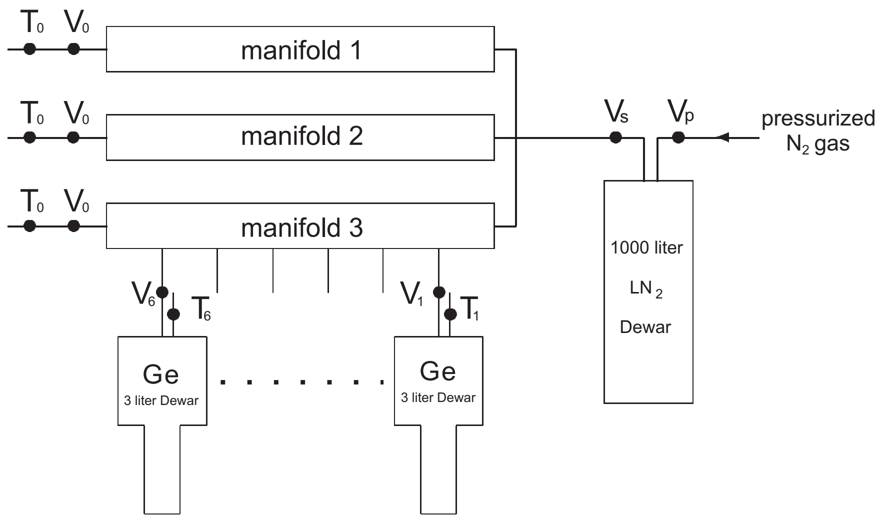

Figure 2.13: Schematic drawing of the LN_2 supplying system.

Cryogenic systems

The Ge detectors were kept at a low temperature by supplying liquid nitrogen (LN_2) every 12 hours. As shown in Fig.2.13, each Ge detector had a 3 ℓ LN_2 Dewar, which was connected to a 1000 ℓ LN_2 Dewar which was pressured by nitrogen gas. LN_2 was supplied to the detectors by controlling valves manually. During the supplying process, the temperature at the gateway for LN_2 to each detector Dewar was monitored in order to judge whether the LN_2 is full or not [45].

4.2 BGO scintillation counter

The BGO scintillation counters were used to suppress backgrounds in the Ge detector spectrum from electromagnetic shower caused by decay of π^0 and Compton scattering. As shown in Fig.2.14, each Ge detector was surrounded by six segmented BGO crystal and each of them was connected to a $1\frac{1}{8}''$ photomultiplier tube (HAMAMATSU R1355). Considering the γ-ray stopping power, we used the BGO counters of 2-cm thick. The BGO counters are not participated in the trigger but used in offline analysis. If the γ ray hit the Ge detector and its surrounding BGO counters simultaneously, the event was eliminated from the γ-ray spectrum of the Ge detector. The properties of BGO scintillators are summarized in Table 2.4. Because of a long decay time and a small light yield, the photo electrons from BGO scintillator light are distributed sporadically. Therefore, the pulse hight of the PMT output signal is almost the same as that of single photo-electron for γ rays of a few hundred keV. In this experiment, the threshold of the discriminator is set low enough to achieve a good detection efficiency for such γ rays (Fig.2.15). In this case, satellite component increases the background in the TDC spectrum and prevents BGO scintillators from using under high counting rate.

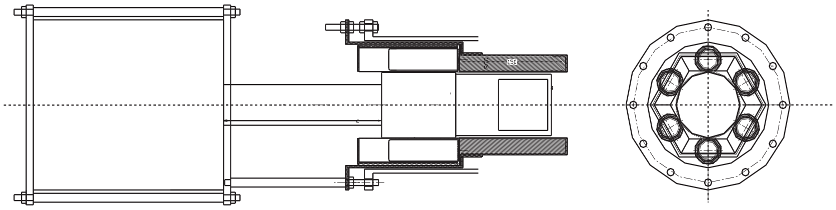

Figure 2.14: Schematic drawing of Ge detector and BGO scintillator.

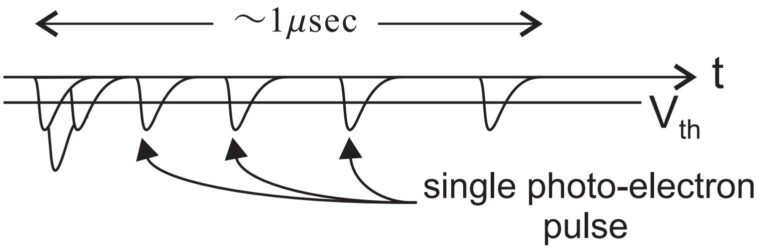

Figure 2.15: Schematic view of the light output from BGO scintillator for a few hundred keV γ ray.

Table 2.4: Properties of BGO scintillatiors.

$1/e$ decay time	300 nsec
Relative light output (NaI(Tl):100)	$7 \sim 10$ %
Density	7.13 g/cm^3
Refractive index	2.15
Radiation length	7.97 g/cm^2

4.3 Readout electronics

In order to measure the γ-ray energy under high counting rate, we have to be worried about the dead time caused by pile-up of the shaping amplifier output. In such a condition, short shaping time constants are necessary to achieve high throughput. We used ORTEC 973U (Ultra-Highrate Amplifier, UHA) which contains a shaping amplifier with a fast time constant and a "gated-integrator (GI)". Because of a short time constant, the shaping amplifier output signal is deformed and the resolution is deteriorated. The GI solves this problem by integrating the signal. This amplifier reduces the dead time because it achieves a good energy resolution with a integration time of 3 μsec, which is faster than that of the conventional shaping amplifiers($\sim$10 μsec). The GI output was connected to 8064-channel ADC (ORTEC AD413A).

As shown in Fig.2.16, the timing information of the γ ray was measured by two different way in relative to the timing of the (π^+, K^+) reaction. We used ORTEC 579 (Timing-Filter Amplifier, TFA) to achieve the best timing resolution of Ge detectors. Output signal of the TFA was connected to constant-fraction discriminator (CFD). The threshold for the timing measurement using the TFA was decided by this device as low as possible. We also measured the γ-ray timing using count-rate meter output (CRM) of the UHA. In this case, the threshold is automatically decided by the UHA. We mainly used the TFA for the timing measurement because the timing resolution is better and the threshold is reliable for the low energy γ ray. Both of the CRM and the TFA outputs were connected to multihit TDC which can measure up to 16 hits per a event (LeCroy 3377).

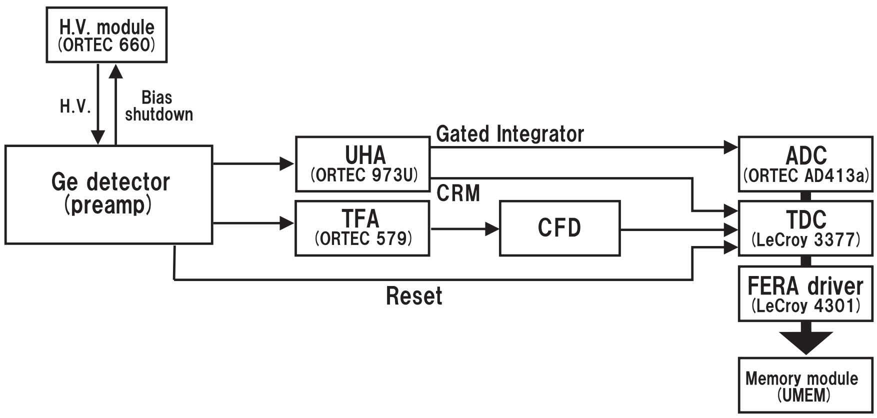

Figure 2.16: Block diagram of readout electronics of the Ge detectors.

§ 5 Target

We used 98.8 % enriched ^{11}B whose density was 2.38 g/cm^3 for target. The ^{11}B powder was sintered in order to reduce the dispersion of the stopping time of ${}^{11}_{\Lambda}$B, which increases an error for the lifetime measurement with DSAM (see Chapter 3 for details). If a grain of ^{11}B is too small to stop the produced ${}^{11}_{\Lambda}$B in it, the stopping time cannot be estimated from the density of ^{11}B. In order to avoid such ambiguity, we made 10 pieces of ^{11}B tablet whose size was 5 cmϕ $\times$1 cm using a special hot-press technique in Institute for Materials Research of Tohoku University. The density of each tablet was equivalent to more than 99% of ^{11}B metal density.

The thickness of the target was 23.8 g/cm^2(10 cm) and 14.3 g/cm^2(6 cm), which was adjusted by changing the number of tablet. As summarized in Table 2.5, the position and the thickness were adjusted several times in order to optimize the counting rate of the background γ-ray considering the radiation damage.

§ 6 Trigger Logic

The block diagram of the trigger logic in the present experiment is shown in Fig.2.17. For incident pions, we made the BEAM trigger as

$$\mathrm{BEAM} \equiv \overline{\mathrm{GC}} \cdot \mathrm{BH1} \cdot \mathrm{BH2}. \tag{2.1}$$

The positron contamination was removed by the anti-coincidence with the GC counter.

Outgoing kaons were selected by the KOUT trigger as

$$\mathrm{KOUT} \equiv \mathrm{TOF} \cdot \mathrm{LC} \cdot \overline{\mathrm{AC1}} \cdot \overline{\mathrm{AC2}}, \tag{2.2}$$

where LC was used to remove protons and AC's were used to remove pions. There were many protons remaining in the KOUT trigger because the LC counters sometimes give signals for protons by δ-rays. Therefore, we removed them in the offline analysis.

Thus, the trigger for the (π^+, K^+) reaction was defined as

$$\mathrm{PIK} \equiv \mathrm{BEAM} \cdot \mathrm{KOUT}. \tag{2.3}$$

The trigger timing was determined by the timing of the BH2 counters. We didn't use the Ge detectors nor the BGO counters in the trigger logic.

There was another trigger which was prepared to monitor the in-beam performances of the Ge detectors. We made the trigger as

$$\mathrm{CALIB} \equiv \sum_{\text{Ge detectors}} \text{Ge CRM} \cdot \text{Co pulsar}. \tag{2.4}$$

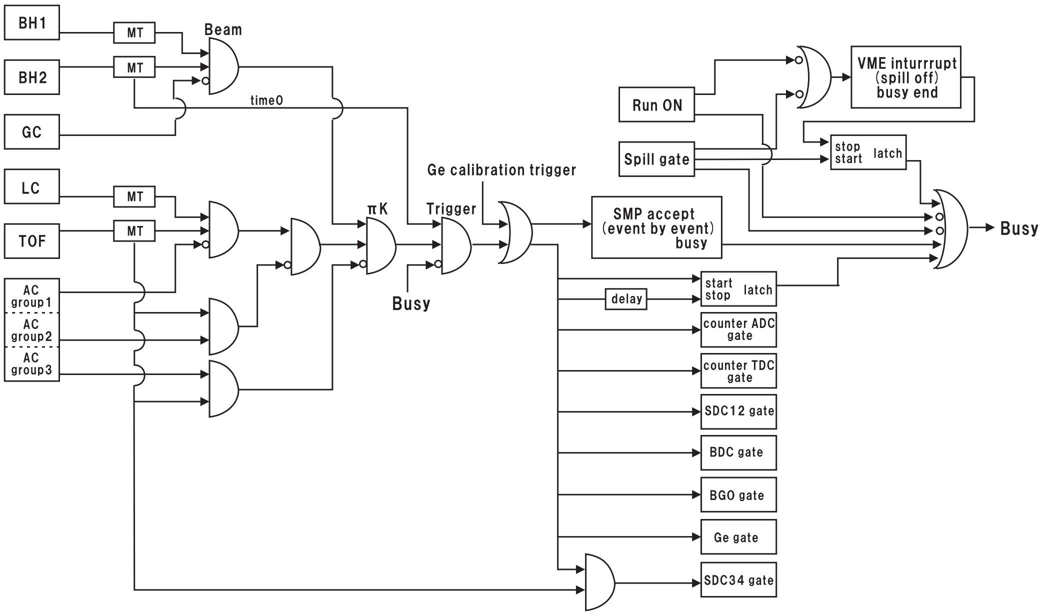

Figure 2.17: Block diagram of trigger logic.

This trigger was used to observe γ rays from a ^{60}Co source which was located behind each Ge crystal as shown in Fig.2.18. The 1 kBq ^{60}Co source was put on a plastic scintillator and connected to a photomultiplier tube (PMT) to observe β ray. The CALIB trigger was generated by requiring timing coincidence between the plastic scintillator (β ray) signal (Co pulsar) and the Ge detector (γ ray) signal (Ge CRM). Then, the trigger signals were summed up for all the Ge detectors. The CALIB trigger was set for both of the durations in beam-on period and in beam-off period for each synchrotron operation cycle. The performance of the Ge detectors was checked by comparing the ^{60}Co γ-ray peak counts and peak shapes for these two periods.

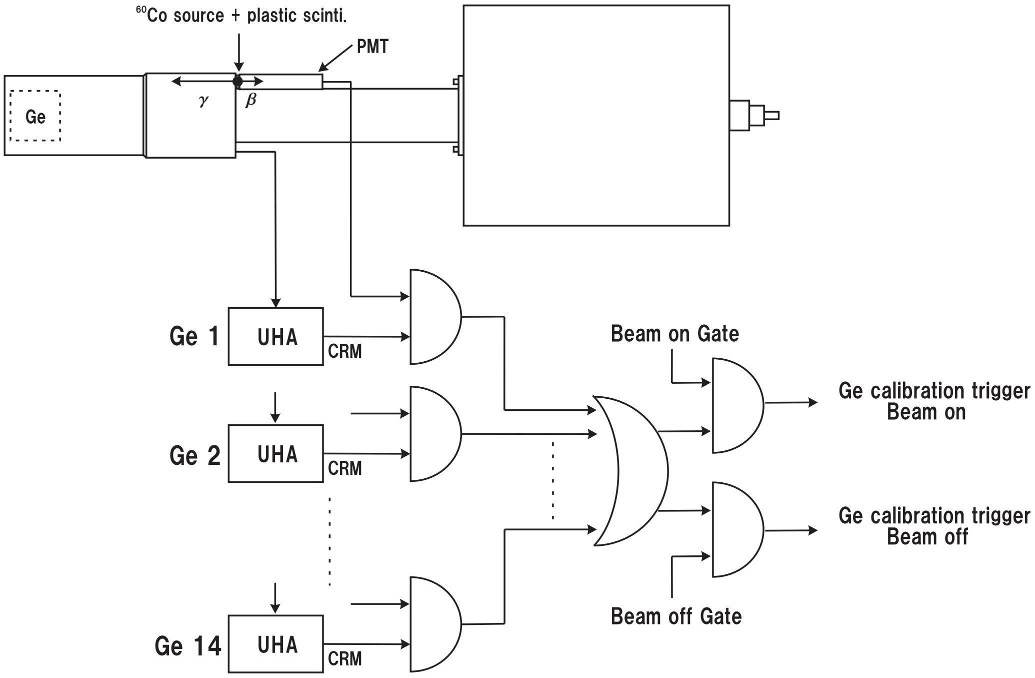

Figure 2.18: Block diagram of Ge calibration trigger.

§ 7 Data acquisition system

In order to reduce a dead time caused by data acquisition (DAQ) system, the ADC and TDC data is transfered to a memory module during the timing gate which includes the (π^+, K^+) reaction trigger and the Ge calibration trigger. The ADC and TDC data of the Ge detectors was transferred to Universal Memory Module (UMEM) in the VME crate via FERA bus [46]. The other data was transfered from ADC's and TDC's in six TKO crates to respective Super Memory Partner (SMP) modules in the VME crate.

As shown in Fig.2.19, the collected data was transfered to the LINUX PC in the VME crate after the "Spill End" signal which is issued at the end of the timing gate for the CALIB trigger in the beam-off period (Beam OFF ^{60}Co gate). The data was written on the DVD RAM and also sent to the on-line analyzer process.

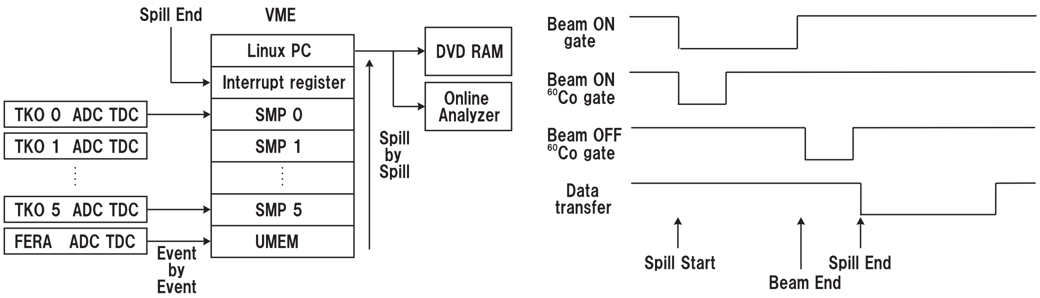

Figure 2.19: Block diagram of data acquisition system. The data transfer starts by the "Spill End" signal which is issued after the "Beam OFF ^{60}Co gate".

§ 8 Data summary

We used about 700 hours of beam time for this experiment in the autumn of 2002. The total amount of irradiation is summarized in Table 2.5. The data with a thin ^{11}B and a carbon targets were taken to observe an excitation energy of hypernuclei using the magnetic spectrometers. The target position was defined as a distance from the center of Hyperball frame toward the beam direction.

Table 2.5: Total number of pions irradiated on each target. Target position was defined as a distance from center of Hyperball to the center of the target toward the beam direction.

Target	Thickness (g/cm^2 (cm))	Target position (mm)	Number of pions
^{11}B	23.8 (10.0)	75	0.6×10^{11}
^{11}B	14.3 (6.0)	125	6.2×10^{11}
^{11}B	14.3 (6.0)	25	1.3×10^{11}
^{11}B	23.8 (10.0)	50	7.9×10^{11}
^{11}B	2.38 (1.0)	50	3.0×10^{10}
carbon	3.54 (2.0)	0	1.3×10^{10}

Chapter 3

γ-ray spectroscopy of ${}^{11}_{\Lambda}$B — Analysis

§ 1 Overview

In this chapter, the analysis procedure of KEK-PS E518 will be described in detail. Figure 3.1 shows a flow chart of the whole analysis.

The analysis for this experiment can be divided into two parts. One is the analysis on the magnetic spectrometers. The purpose of this measurement is to calculate the excitation energy of ${}^{11}_{\Lambda}$B and select the bound state region. The incident and the scattered particles were classified into pions, kaons and protons. The momenta and the trajectories of each particle were derived to calculate the excitation energy. The momentum vector and the vertex position were measured by the spectrometers and used for the event-by-event Doppler shift correction of the γ-ray energy.

The other part is analysis on γ rays. The γ-ray energies were observed using germanium (Ge) detectors for the events in which the bound states of ${}^{11}_{\Lambda}$B were found to be populated by the (π^+, K^+) reaction. In order to reduce background from measured γ-ray spectra, we selected events using timing information of the Ge detectors and the BGO scintillation counters. Using the timing information of the Ge detector, the backgrounds from accidental counting and pile up within $\sim$3 μsec width of ADC input signal were reduced. When the charge collected in the preamplifier is released by the transistor reset, the Ge detector detects uncertain energy information within 10 μsec or so. Such energy information was also removed by measuring the timing of the reset signal which was issued at the preamplifier of the Ge detectors. The timing information of the BGO scintillation counters was measured to suppress backgrounds from electromagnetic shower caused by decay of π^0 and Compton scattering. The background was also suppressed when the high energy charged particles penetrated the Ge crystal. The energy calibration, Doppler-shift correction and Doppler-shift attenuation method were also mentioned in this chapter. The measured γ-ray energy was calibrated using γ-ray sources and known γ rays observed as backgrounds. The Doppler-shift correction is useful when the lifetime of the transition is shorter than the stopping time of the hypernuclei. The Doppler-shift attenuation method is used to measure the lifetime of the γ-ray transition.

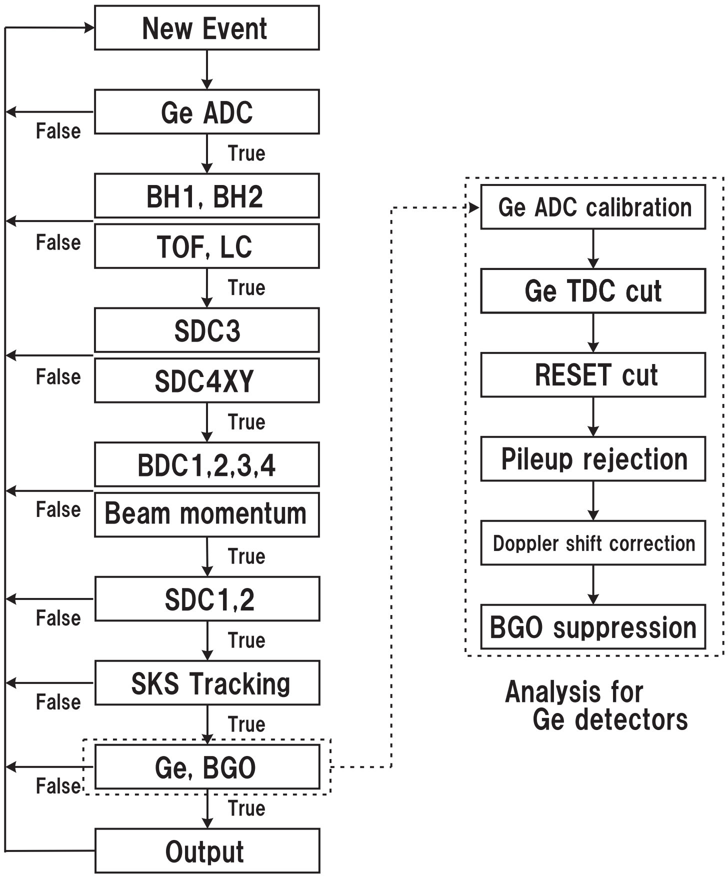

Figure 3.1: Flow chart of a event-by-event analysis.

§ 2 Magnetic spectrometers

As mentioned in Chapter 2, we used the magnetic spectrometer systems at the KEK-PS K6 beamline. Following rough event selection which was performed by requiring some hits in the ADC's of the Ge detectors, we selected an incident π^+ and a scattered K^+ from the events in the PIK trigger. Incident π^+ was selected by measuring the time-of-flight between BH1 and BH2. Scattered K^+ was roughly selected using the TOF and the LC counters. Since the trajectory of the scattered kaons were different according to the scattering angle, we were not able to classify the particles completely only from the time-of-flight measurement.

After that, the momenta and the flight-path lengths of the incident and the scattered particles were determined from the hit position on the drift chambers by reconstructing the trajectory using Runge-Kutta method. Candidates for the position and the direction of each particle were determined at the entrance and the exit of the magnet systems using the TDC data of the drift chambers. Then, the mass of the scattered particles, which was calculated using these values as well as the time-of-flight between the BH2 and the TOF counters, were used for the particle identification. The vertex position and the scattering angle were also measured in order to select good events. Finally, the hypernuclear mass was reconstructed from the momentum vectors of the incident π^+ and the scattered K^+.

In this section, the procedure of the analysis to obtain the hypernuclear mass spectrum are described in detail.

2.1 Momentum reconstruction of incident particle

The momentum of the incident particles was measured from the hit position of drift chambers located at the upstream (BDC1,2) and downstream (BDC3,4) of the QQDQQ magnet system. At first, the candidates for the trajectory of each particle were locally reconstructed by fitting the hit positions with the linear function at the upstream and the downstream of the magnet system, respectively. Then, the momentum was determined by minimizing the χ^2 value which is defined as

$$\chi^2_{K6} \equiv \underbrace{\frac{1}{n-5}\sum_{i=1}^{12} H_i \left(\frac{P_i - f_i(\vec{X}_{in})}{w_i}\right)^2}_{\text{BDC1,2}} + \underbrace{\frac{1}{n-5}\sum_{i=13}^{24} H_i \left(\frac{P_i - g_i(\vec{X}_{out})}{w_i}\right)^2}_{\text{BDC3,4}}. \tag{3.1}$$

Here,

$$\begin{aligned} n &= \sum_{i=1}^{24} H_i \\ H_i &= \begin{cases} 1, & \text{if } i\text{th plane has a hit in the local track,} \\ 0, & \text{if } i\text{th plane has no hit in the local track,} \end{cases} \\ \vec{X}_{out} &= \mathcal{M}(\vec{X}_{in}, p), \end{aligned} \tag{3.2}$$

where P_i is the candidates for the hit position on the ith plane of the drift chambers, which is obtained from local tracks, and w_i is the spatial resolution of the ith plane. $\vec{X}_{in}$ and $\vec{X}_{out}$ represents a direction of incident particles at the entrance and the exit of the magnet system. The hit position on the ith plane for the fitted trajectories is denoted as $f_i(\vec{X}_{in})$ and $g_i(\vec{X}_{out})$. $\vec{X}_{out}$ is calculated from $\vec{X}_{in}$ through the 3rd-order transport matrix ($\mathcal{M}$) using a momentum (p) as a parameter [41]. For multi-track events, the best track was selected to give the least χ^2 value. Figure 3.2 shows a typical distribution of the minimum χ^2_{K6}. The events whose χ^2_{K6} is less than 30 were accepted as good tracks. Figure 3.3 shows a typical momentum distribution of the incident particles.

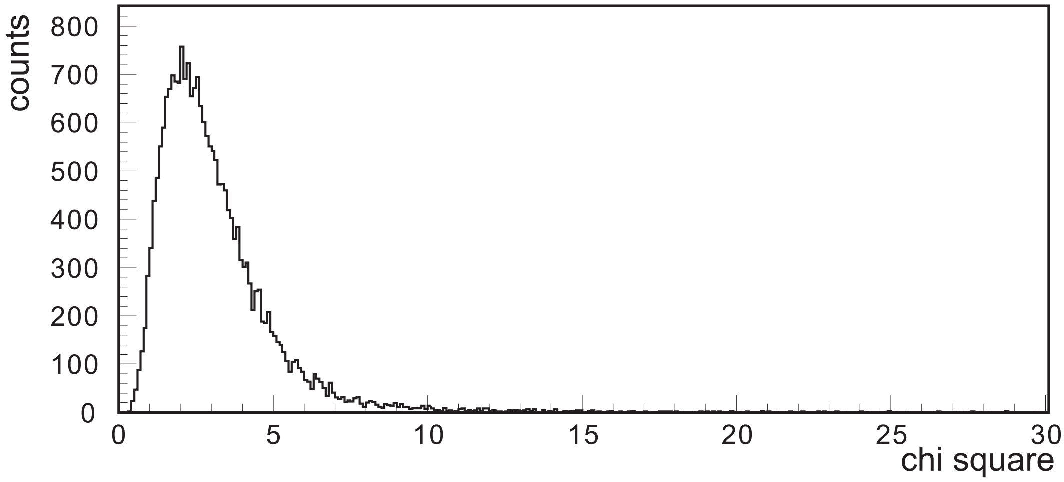

Figure 3.2: Minimum χ^2_{K6} distribution of the incident particles.

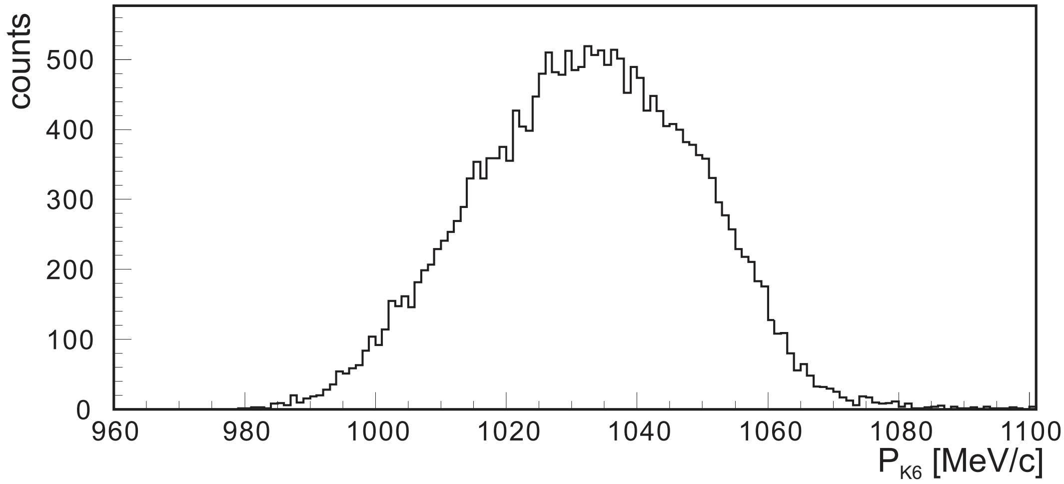

Figure 3.3: Momentum distribution of the incident particles.

2.2 Momentum reconstruction of outgoing particle

The momentum of outgoing particles which were scattered at the target were determined from hit positions of the drift chambers located at the upstream (SDC1,2) and downstream (SDC3,4) of the SKS magnet. The first step of the analysis is almost identical to that for the incident particle. The candidates for the trajectories of each particle were locally reconstructed by fitting the hit positions with the linear function and the corrected hit positions at each chamber plane are obtained.

Since the SKS magnet has a large acceptance, the transport matrix is not convenient to calculate the momentum. The momentum and the trajectory were calculated by Runge-Kutta method using the precisely measured magnetic field map. There were five parameters to be optimized, namely the momentum $(1/p)$, the horizontal and the vertical positions of the particles at $z = 0$ (x_0, y_0) and their differential to the z axis $(\frac{dx_0}{dz}, \frac{dy_0}{dz})$. These parameters were determined by minimizing the χ^2_{SKS} which is defined by

$$\chi^2_{SKS} \equiv \frac{1}{n-5} \sum_{i=1}^{n} \left(\frac{x_i^{tracking} - x_i^{data}}{w_i} \right)^2 , \tag{3.3}$$

where n is the number of planes having hits, $x_i^{tracking}$ and x_i^{data} are the hit positions on the ith plane in the tracking and the data, respectively, and w_i is the spatial resolution of the ith hit plane. The path length of the trajectory was also obtained here.

Figure 3.4 shows a typical distribution of the minimum χ^2_{SKS}. The events whose χ^2_{SKS} is less than 30 were accepted as good tracks.

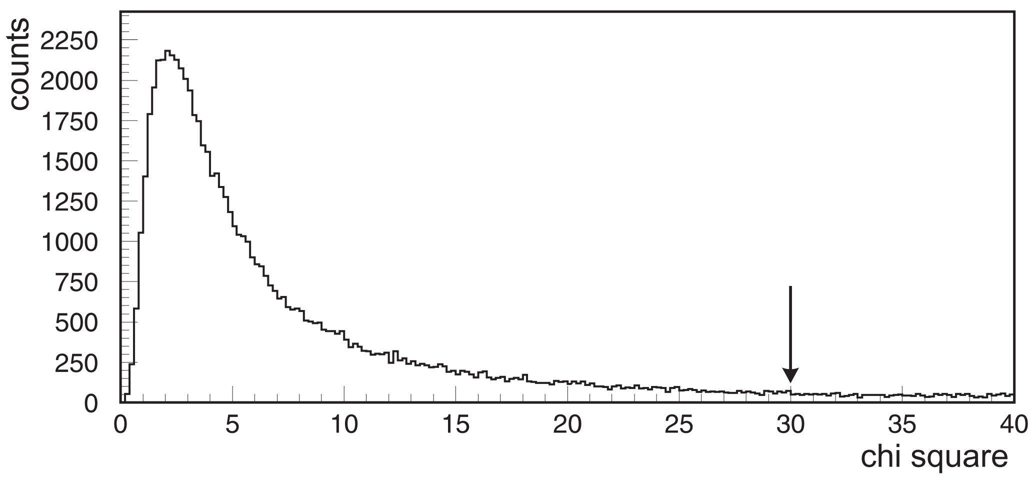

Figure 3.4: Minimum χ^2_{SKS} distribution of the outgoing particles. The events where $\chi^2_{SKS} < 30$ were accepted as good tracks.

2.3 Particle identification

The incident and the outgoing particles were roughly identified in the trigger level (see §6 in Chapter 2). More precise identification is necessary in the offline analysis in order to reduce the background from hypernuclear mass spectrum.

The incident pions were selected using the time-of-flight between the BH1 and the BH2 as shown in Fig.3.5. The events in the region indicated with arrows were selected as pions. The outgoing kaons were selected from the measured mass (M_{out}) which was calculated by

$$M_{out} = \frac{p}{\beta}\sqrt{1-\beta^2}, \tag{3.4}$$

where p is the measured momentum of an outgoing particle. β is the velocity which is measured from the time-of-flight and the flight-path length between the BH2 and the TOF counters. Figure 3.6 shows a typical mass spectrum for the PIK trigger events. The events whose mass corresponds to 400 MeV< M_{out} < 600 MeV were selected as kaons.

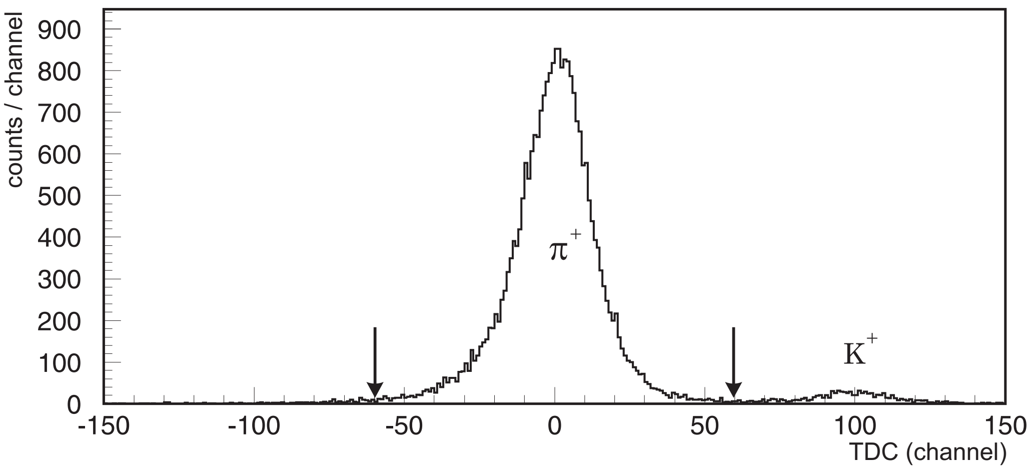

Figure 3.5: The time-of-flight spectrum measured for the incident particles. The events between two arrows were selected as π^+.

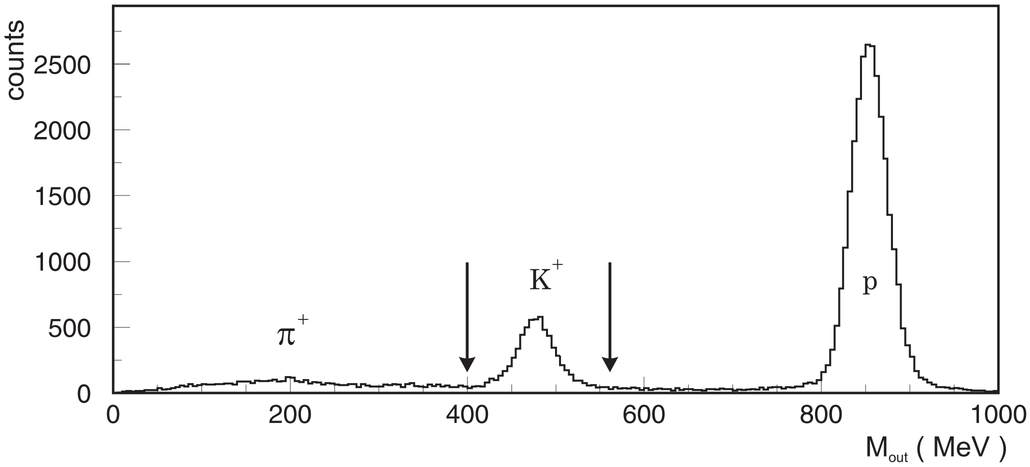

Figure 3.6: The measured mass spectrum of the outgoing particles. The events between two arrows were selected as K^+.

2.4 Vertex position and reaction angle

The vertex position and the scattering angle were obtained from the trajectories of the incident and the outgoing particles. The trajectory of the incident pions were determined by a local track in BDC3,4. For the outgoing kaons, the trajectory was determined in the momentum reconstruction of the SKS.

The vertex position in the z coordinate (z-vertex) was defined as the closest point between the incident and the outgoing trajectories projected on the x-z plane, because the spatial resolution in the x coordinate was better than the y coordinate. The x- and y-vertices were determined as an average of the positions between the incident and the outgoing trajectories at the z-vertex point. Figures 3.9 and 3.10 show a z-vertex distribution (left) and their differentials for z axis (right), which is obtained for a target of 6-cm thick and 10-cm thick, respectively. The reaction point in the target region was selected as shown by two arrows in Figures 3.9 and 3.10 (left). As mentioned in Chapter 2, we adjusted the target thickness and position several times. The cut parameter of the reaction point was set for each conditions. The vertex resolution was obtained by fitting the differential spectra with gaussian to be 1.2 cm (FWHM) for the 6-cm target and 1.6 cm(FWHM) for the 10-cm target. The resolution affects the accuracy of the Doppler-shift correction and the lifetime measurement using Doppler-shift attenuation method (see §3 in detail).

Figure 3.7 shows the distribution of the scattering angle measured for the (π^+, K^+) events. Here, the reaction point was selected using the measured z-vertex. In order to remove events whose z-vertex resolution was significantly bad, we selected the event whose horizontal scattering angle is larger than 10 mrad. Angular resolutions were estimated by comparing the scattering angle measured for a 0.72 GeV/c π^+ beam without target (Fig.3.8). The obtained resolutions were 11.8 mrad (FWHM) for the horizontal reaction angle and 16.5 mrad (FWHM) for the vertical angle including a multiple scattering effect of $\sim$ 7 mrad (FWHM) in the target.

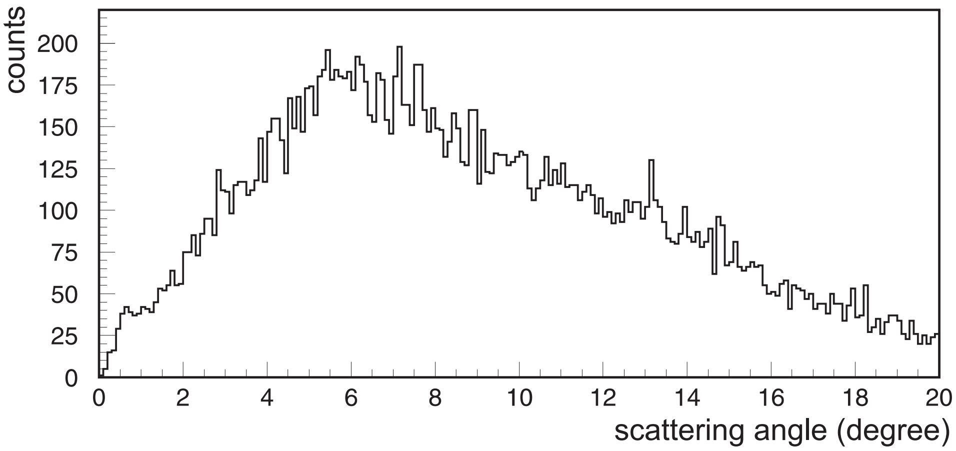

Figure 3.7: The distribution of the scattering angle measured for the (π^+, K^+) event. Here, vertex position was selected for the target region.

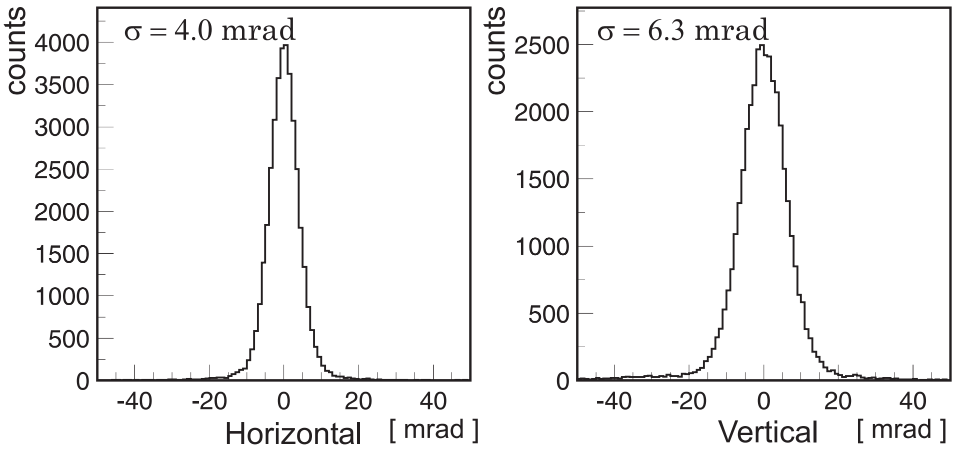

Figure 3.8: Angular resolution estimated by comparing the scattering angle measured for a 0.72 GeV/c π^+ beam without target.

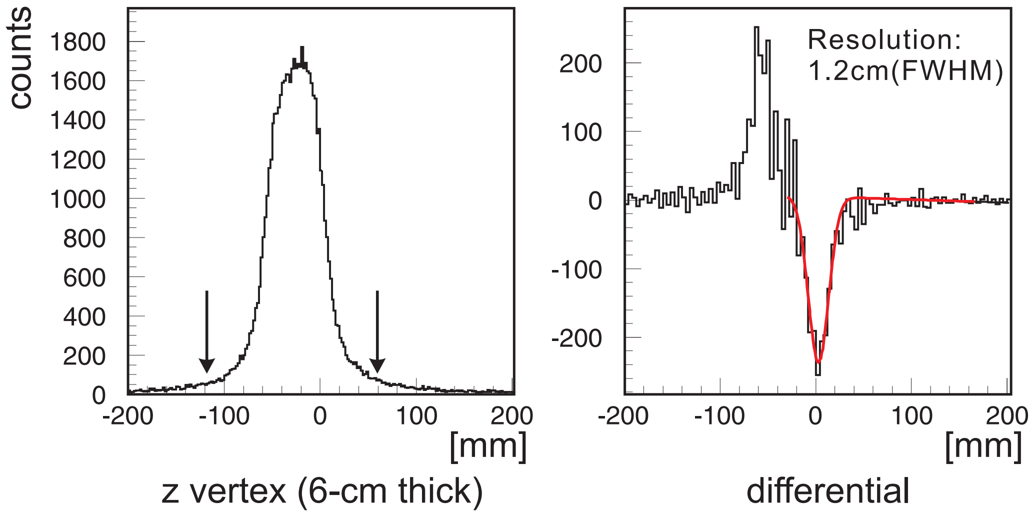

Figure 3.9: The z-vertex distribution for 6-cm target (left) and their differentials for z axis (right). The target position was 25 mm downstream from the center of the Hyperball frame. The events between two arrows were selected as good events in the target region. The vertex resolution was measured by fitting the differential spectrum with gaussian.

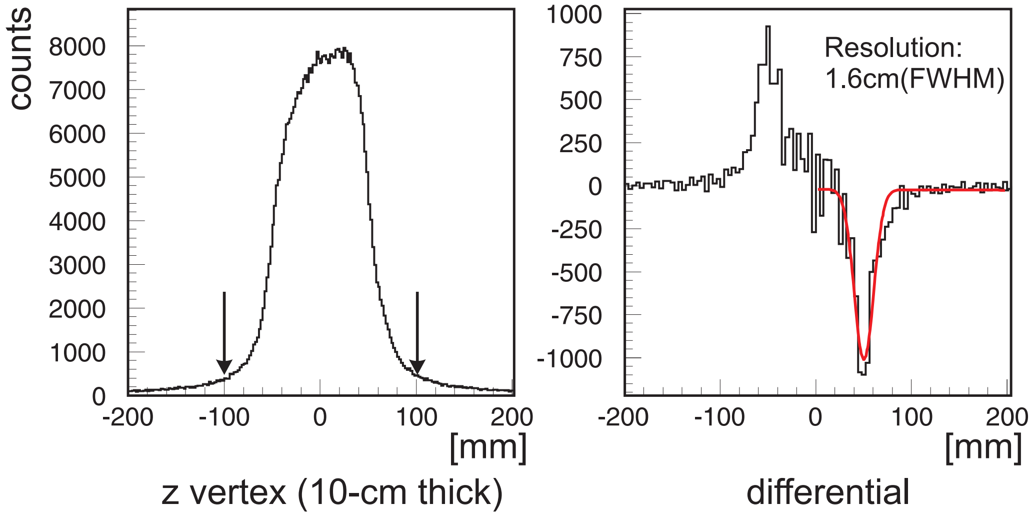

Figure 3.10: The z-vertex distribution for 10-cm target (left) and their differentials for z axis (right). The target position was 50 mm downstream from the center of the Hyperball frame.

2.5 Missing mass and binding energy of Λ

The missing mass of the hypernuclei produced by the ^{11}B (π^+, K^+) reaction was calculated by

$$M_{hyp} = \sqrt{(E_{\pi^+} + M(^{11}\mathrm{B}) - E_{K^+})^2 - |\vec{p}_{\pi^+} - \vec{p}_{K^+}|^2}, \tag{3.5}$$

where E_{π^+}, E_{K^+}, $\vec{p}_{\pi^+}$ and $\vec{p}_{K^+}$ are energy and momentum of the incident and outgoing particles, respectively. In order to calculate the missing mass, the momenta of pions and kaons have to be corrected. We considered the correlation between the momentum offset and the scattering angle, the energy loss in the target and the absolute scale of the missing mass.

Figure 3.11 shows a correlation between the horizontal scattering angle and the missing mass measured by a carbon target of 3.54 g/cm^2 thick. As shown in the left figure, the missing mass has the correlation with the scattering angle before the momentum correction. Then, we have corrected the momentum of the scattered K^+ as

$$p_{K^+}^{corrected} = p_{K^+} + 17.0\left(\frac{dx}{dz}\right)_{K^+} + 28.36\left(\frac{dx}{dz}\right)_{K^+}^2 - 2.0\left(\frac{dy}{dz}\right)_{K^+} - 10.0\left(\frac{dx}{dz}\right)_{K^+}^2 [\mathrm{MeV}/c], \tag{3.6}$$

and obtained the right figure. Here, parameters were phenomenologically introduced to remove the correlation.

The absolute scale of the missing mass was calibrated using the carbon target because the Λ-binding energy (B_Λ) and the (π^+, K^+) cross sections of the states in $^{12}_{\Lambda}$C are experimentally well known [42]. Here, B_Λ is defined by

$$-B_\Lambda = M_{hyp} - M_\Lambda - M_{core}. \tag{3.7}$$

The Λ-binding energies are experimentally determined to be 10.76 ± 0.19 MeV for $^{12}_{\Lambda}$C and 10.24 ± 0.05 MeV for $^{11}_{\Lambda}$B [47]. As shown in Fig.3.12 (a), the ground state of $^{12}_{\Lambda}$C was fitted by a gaussian and the peak position was used to check the B_Λ scale. Then, 6.5-MeV offset is added to the momentum of the outgoing kaons. This offset is arbitrary because we can also reproduce the same effect by changing the momentum of the incident pions or both of the incident and outgoing particles. Therefore, the absolute momentum scale has still some uncertainty.

We applied the same corrections for the correlation between the momentum offset and the scattering angles to $^{11}_{\Lambda}$B and $^{12}_{\Lambda}$C because these corrections are originated from inaccuracy in the momentum reconstruction by the magnetic spectrometers. The other correction, for the energy loss in the target was estimated using the calculated momentum losses in a 1-cm thick target and the flight-path lengths of the incident pions and the outgoing kaons in the target region. The momentum losses for the carbon and the ^{11}B targets were calculated for 1.05 GeV/c pions and 0.72 GeV/c kaons using LEPS code [48] as summarized in Table 3.1. The flight-path length was measured from the reaction vertex and their track for each particle.

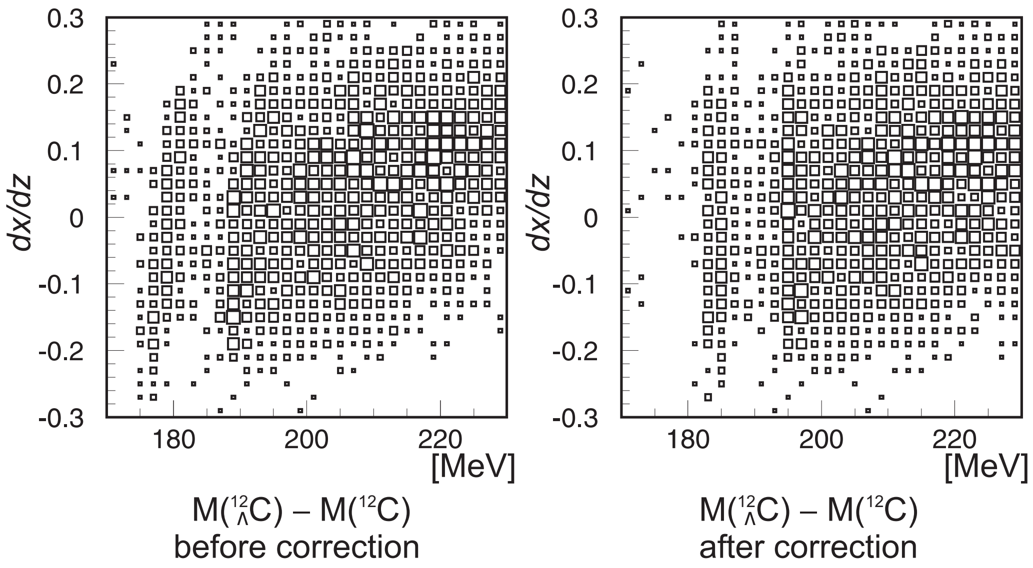

Figure 3.11: Correlation between the horizontal scattering angle (dx/dz) and the missing mass measured for the carbon target. The momentum of the scattered kaons was corrected in the right figure. In the right figure, the absolute mass scale and the energy loss in the target were also corrected.

By applying these momentum corrections, we obtained the binding energy spectra as shown in Fig.3.12. In this figure, we can see that the measured B_Λ was well calibrated for the carbon and the 1-cm ^{11}B targets. However, the absolute values of the B_Λ can be different for each thickness of the ^{11}B target according to inaccuracy in the energy loss correction. The difference in the 6-cm and 10-cm targets was estimated by comparing the mass spectrum gated for the γ rays from ${}^{11}_{\Lambda}$B (Fig.3.13). Then, the uncertainty was estimated to be less than 0.5 MeV.

The resolution in the mass spectra cannot be estimated from Fig.3.13 because many states are expected to be included in it. Then, the mass resolution was estimated from the momentum resolution of the magnetic spectrometers and the expected energy-loss fluctuation in the target. In this experiment, the mass resolution is mainly determined by the energy-loss fluctuation because we used thick

Table 3.1: The momentum loss in the targets of 1-cm thick.

	Momentum loss in carbon	Momentum loss in ^{11}B
1.05 GeV/c π^+	3.19 MeV/c	3.94 MeV/c
0.72 GeV/c K^+	3.78 MeV/c	4.69 MeV/c

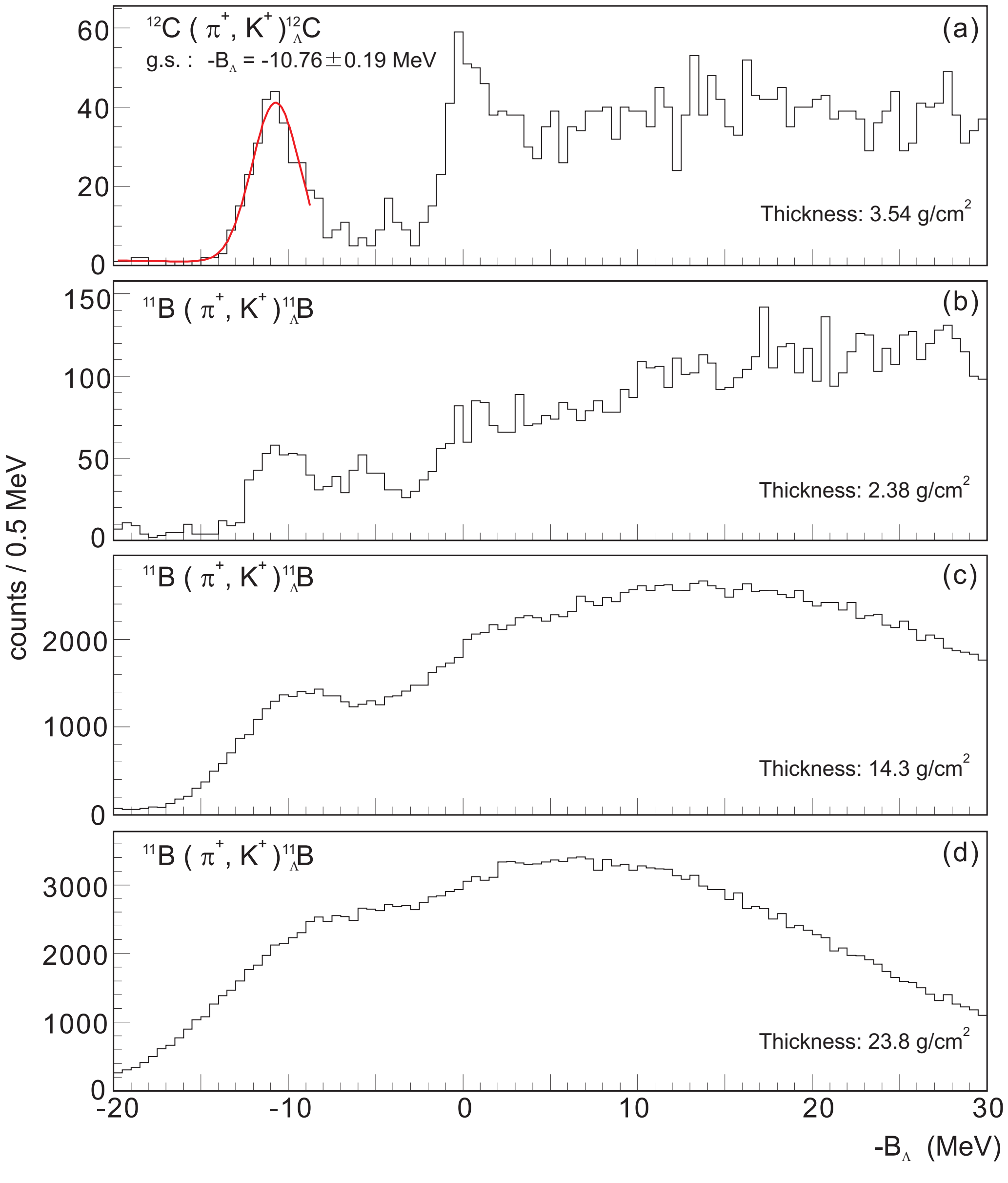

Figure 3.12: Λ-binding energies in (a) ${}^{12}_{\Lambda}$C and (b, c, d) ${}^{11}_{\Lambda}$B measured for the target of 3.54, 2.38, 14.3 and 23.8 g/cm^2 thick, respectively. The absolute scale is calibrated using the ground state in ${}^{12}_{\Lambda}$C, which is experimentally determined to be B_Λ = 10.76 ± 0.19 MeV.

targets [45]. Figure 3.14 shows a distribution of the momentum difference between the two spectrometers measured for 0.72 GeV/c pions (a) without and (b) with the ^{11}B (23.8 g/cm^2) target. The momentum-loss fluctuation in (a) is originated from the resolution of the spectrometers and the energy-loss fluctuation in the BH2 counter, which is obtained to be 3.80±0.05 MeV/c (FWHM). In (b), the position and the width of the peak are changed due to the energy loss in the target. The energy-loss fluctuation in the target was estimated to be 6.56±0.21 MeV (FWHM) by comparing these spectra. This fluctuation was consistent with the calculated value of 6.12 MeV (FWHM), which is obtained by using the Bethe-Bloch formula. Therefore, the mass resolution was estimated using the calculated values of the energy-loss fluctuation for 1.05-GeV/c pions and 0.72-GeV/c kaons. In addition to these effects, inaccuracy in the measured vertex position also contributes to the energy-loss fluctuation. Consequently, the hypernuclear mass resolution can be calculated from Eq.(3.5) as

$$\Delta M_{hyp} = \sqrt{\left(\frac{\partial M_{hyp}}{\partial p_{\pi^+}}\right)^2 \Delta p_{\pi^+}^2 + \left(\frac{\partial M_{hyp}}{\partial p_{K^+}}\right)^2 \Delta p_{K^+}^2 + \left(\frac{\partial M_{hyp}}{\partial \theta}\right)^2 \Delta\theta^2}. \tag{3.8}$$

Here, the contribution from the scattering angle θ was negligibly small, and Δp is defined for the incident and the outgoing particles as

$$\Delta p = \sqrt{\Delta p_{Eloss}^2 + \Delta p_{spec}^2 + \Delta p_{vertex}^2}, \tag{3.9}$$

where Δp_{Eloss}, Δp_{spec} and Δp_{vertex} express the momentum fluctuation due to the energy loss, the resolution of the magnetic spectrometers and the vertex resolution, respectively. Δp_{Eloss} was calculated for the averaged flight-path length in the target. Δp_{spec} and Δp_{vertex} were obtained from the momentum difference between the incident and the outgoing particles $(p_{\pi^+} - p_{K^+})$ as

$$\Delta p_{(\pi^+ - K^+)} \equiv \Delta(p_{\pi^+} - p_{K^+}) = \sqrt{2}\Delta p_{spec,vertex}. \tag{3.10}$$

Here, the contribution from the incident and the outgoing particles are assumed to be the same. Then, the hypernuclear mass resolution was calculated to be 4.5 MeV (FWHM) for the 6-cm target and 5.8 MeV (FWHM) for the 10-cm target. On the other hand, the mean energy loss was also estimated from Fig.3.14 (b) to be 36.34±0.10 MeV, which was consistent with the calculated value of 38.4 MeV using the LEPS code.

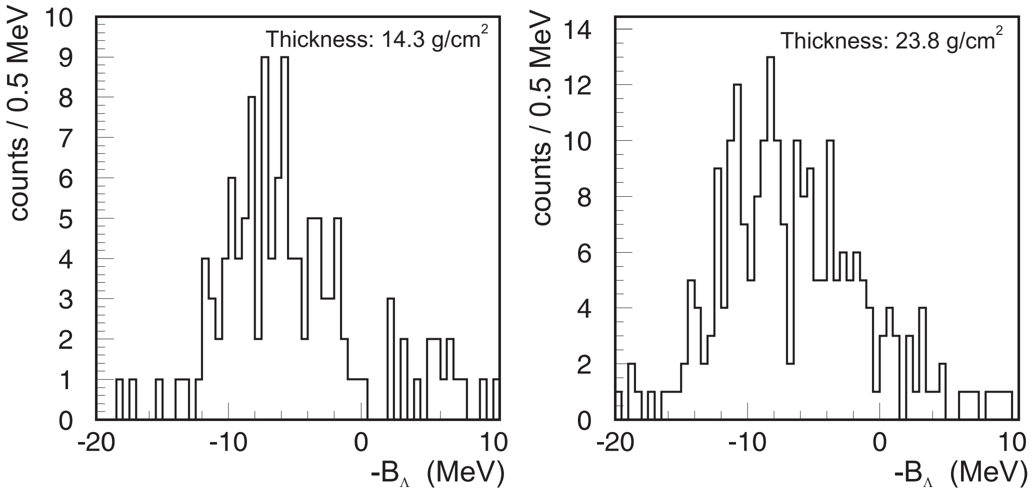

Figure 3.13: Λ-binding energies in ${}^{11}_{\Lambda}$B measured for the targets of 14.3 and 23.8 g/cm^2 thick. The spectra are plotted for the events in which the γ rays were observed from ${}^{11}_{\Lambda}$B using Hyperball.

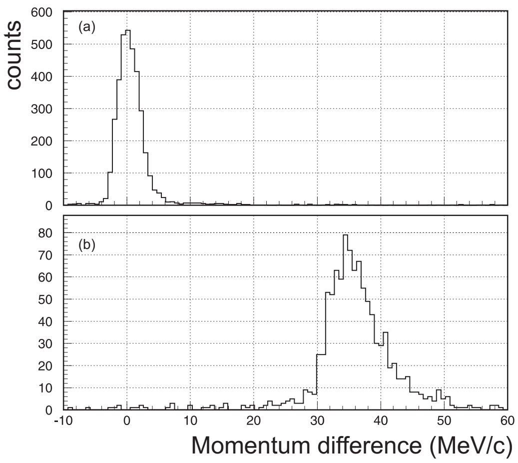

Figure 3.14: Distributions of the momentum difference between the two spectrometers measured for 0.72 GeV/c π^+ (a) without target (b) with ^{11}B target (23.8 g/cm^2). The momentum difference is normalized and the peak position in (a) is adjusted to zero.

2.6 Velocity of the recoiling ${}^{11}_{\Lambda}\mathbf{B}$

The velocity of the recoiling ${}^{11}_{\Lambda}$B has to be measured to correct for the Doppler effect and to determine the lifetimes of γ-ray transitions using Doppler-shift attenuation method (see §3 for details). It can be measured from the momenta of the incident and the outgoing particles as

$$\vec{\beta} = \frac{\vec{p}_{\pi^+} - \vec{p}_{K^+}}{E_{\pi^+} + M({}^{11}\mathrm{B}) - E_{K^+}}. \tag{3.11}$$

Figure 3.15 shows a measured velocity ($|\vec{\beta}|$) distribution of the recoiling ${}^{11}_{\Lambda}$B. The most probable value and the width of the distribution was obtained to be 0.033 ± 0.001 and $(2.89 \pm 0.02) \times 10^{-3}$(FWHM).

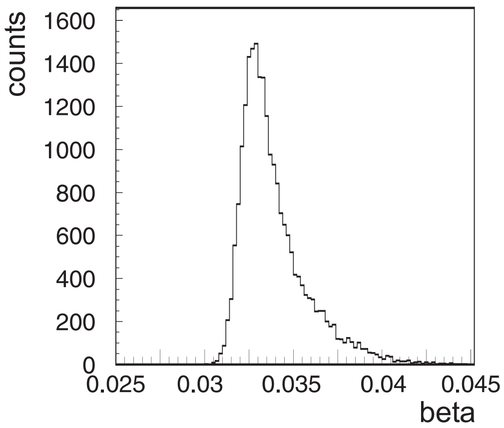

Figure 3.15: Velocity distribution of the recoiling ${}^{11}_{\Lambda}$B, which is measured from the momenta of the incident and the outgoing particles.

§ 3 Hyperball

In this section, the analysis procedure of the Hyperball detectors will be described. The procedure will be described on the event selection, the energy calibration, the γ-ray detection efficiency, the Doppler-shift correction and the Doppler-shift attenuation method.

3.1 Event selection

We measured γ-ray energy (Ge ADC) by choosing proper events using the timing information of the Ge detectors and the BGO scintillation counters. In the following subsections, the condition for the event selection will be described in detail.

Coincidence with the (π^+, K^+) reaction

We measured the γ-ray timing in the Ge detectors using the PIK trigger as a common stop signal (see §6 in Chapter 2). By choosing a proper timing in the TDC spectrum measured by Ge detectors, we reduced the background from the accidental coincidence. Since the time resolution depends on the γ-ray energy, we set a different timing gate width according to the energy. The timing gate was set for each Ge detector so as not to kill the γ rays which was in coincidence with the beam timing. As we mentioned in §4 in Chapter 2, the γ-ray timing was independently measured for each of the CRM and the TFA signals. Because of a good timing resolution, we used the TFA signal to select the events. For a typical Ge detector, the observed TFA spectrum and its γ-ray energy dependence were shown in Fig.3.16.

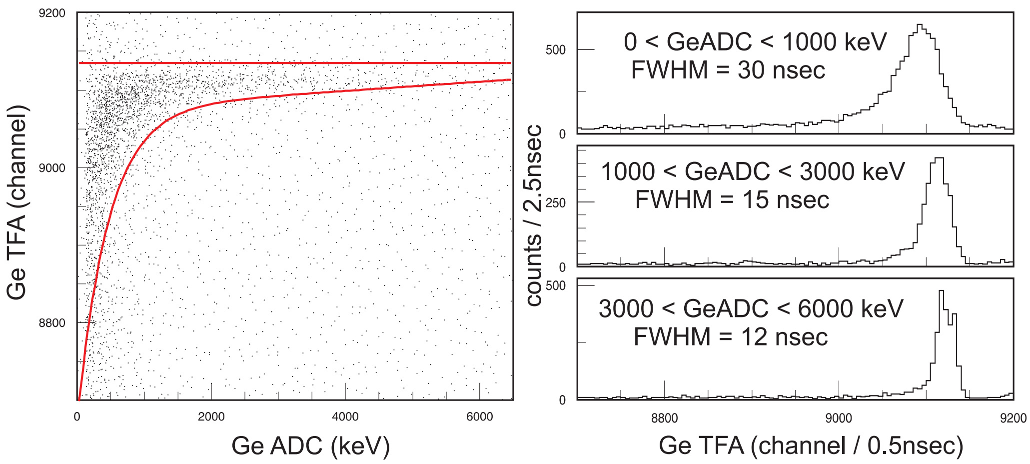

Figure 3.16: Energy (ADC) dependence of the TDC value (TFA) of γ rays for a typical Ge detector. In the left figure, the region between two lines were selected as a proper timing.

BGO scintillation counter

The timing information of the BGO scintillation counters was also measured using the PIK trigger as a common stop signal (see §6 in Chapter 2). If the γ ray hits the Ge detector and its surrounding BGO counters simultaneously, the event was eliminated from the γ-ray spectrum of the Ge detector. Figure 3.17 (a) shows a TDC spectrum of a typical BGO counter. The spectrum was plotted for good (π^+, K^+) events whose reaction vertex agreed with the target region. Here, a hit in the Ge detector surrounded by this BGO counter was also required using the TDC data (TFA) of the Ge detector. The region between two arrows were selected for the anti-coincidence, whose width was typically 100 nsec and adjusted for each counter. The width was adjusted in order to achieve a good signal-to-noize ratio in the Ge ADC spectrum [49]. The accidental killing rate can be estimated from the preceding component in the TDC spectrum. Then, the accidental killing rate was found to be negligibly small.

Figure 3.17 (b) shows ADC spectra of Ge detectors with and without the anti-coincidence with the BGO counters. The suppression factor (F) was defined as a ratio of observed counts in these spectra ($N_{with\ BGO}$, $N_{without\ BGO}$) by the Eq. (3.12) and shown in (c).

$$F \equiv \frac{N_{with\ BGO}}{N_{without\ BGO}} \tag{3.12}$$

Then, the continuous backgrounds were reduced to 1/4 in the γ-ray energy region of higher than 300 keV. On the other hand, the photo peak of the γ ray emitted from the target was not significantly reduced by the suppression. In the case of the 718-keV γ ray from ^{10}B, 9.6 $\pm$ 4.6 % of the photo-peak component was reduced. This is much larger than the one expected from the accidental killing rate, but explained by considering the other γ rays from ^{10}B emitted via cascade process.

Pile-up rejection

If there are more than two γ-ray hits within the 3-μsec integration time of UHA (see §4 in Chapter 2), the observed γ-ray energy can be different from the original one (Fig.3.19 (1)). Since we used the multihit TDC (see §4 in Chapter 2), such pile-up events in the Ge ADC spectrum can be removed by using the time difference of two subsequent γ rays (ΔT), which is defined as a time difference of the additional γ-ray hit against the proper-timing hit selected in 3.1.1. Figure 3.18 (a) shows a correlation between the ΔT and the Ge ADC. Region A ($-3 < \Delta\mathrm{T} < 0$ and $1 < \Delta\mathrm{T} < 3$ μsec) was selected for the pile-up rejection. The events in $0 < \Delta\mathrm{T} < 1$ μsec cannot be removed because there were satellite components of the proper γ ray produced by the preamplifier of the Ge detectors as shown in Fig.3.19 (2). These satellite components appeared after modifying the gain of the preamplifier lower. Figure 3.18 (b) is the Ge ADC spectrum around the 511-keV peak (e^+) measured for the

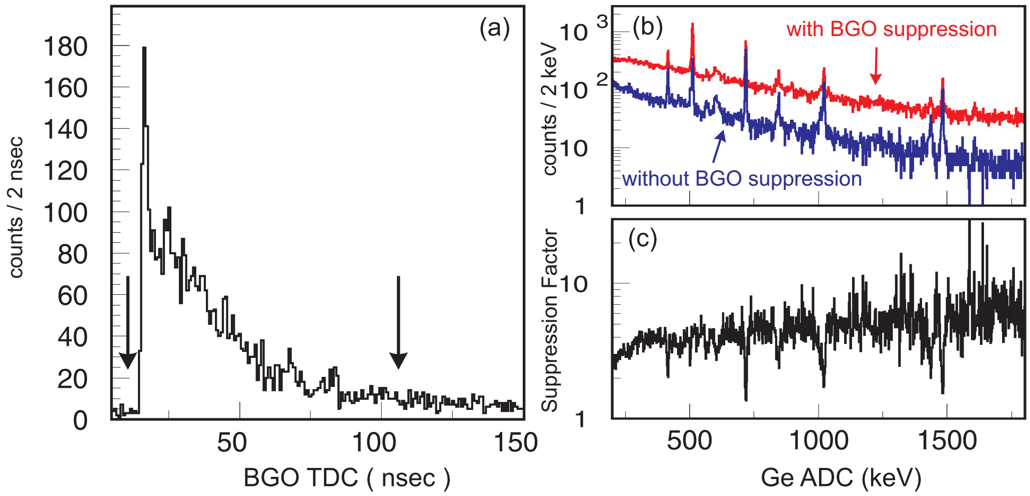

Figure 3.17: (a) The TDC spectrum of typical BGO scintillation counter. Events were selected as described in the text. (b) The ADC spectra of Ge detectors with and without BGO suppression. (c) Suppression factor defined by Eq. (3.12).

events in the region A and (c) is the spectrum in the region B (ΔT < -3 and $3 < \Delta$T μsec).

Here, the signal-to-noise ratio in (b) is worse than in (c). The 511-keV peak in (b) was mainly coming from the preceding region, namely $-3 < \Delta\mathrm{T} < 0$ μsec. These events also have to be removed because the satellite components may accidentally accord with the region selected in 3.1.1 (Fig.3.19 (3)). In total, the dead time of the Ge detectors due to the pile-up rejection was 5.6 ± 0.4 %.

Reset veto

After the reset of the preamplifier, the output of the UHA was affected by base line shift caused by differentiation of the sudden level drop of the preamplifier output. Therefore, the events have to be rejected when the reset signal was issued just before the γ-ray hits. The reset veto gate was set after the reset for the period of 15 μsec for the ORTEC detectors and 35 μsec for the Eurisys detectors. The reset timing was measured using a multihit TDC. Then, the events in the reset veto gate were rejected in the offline analysis.

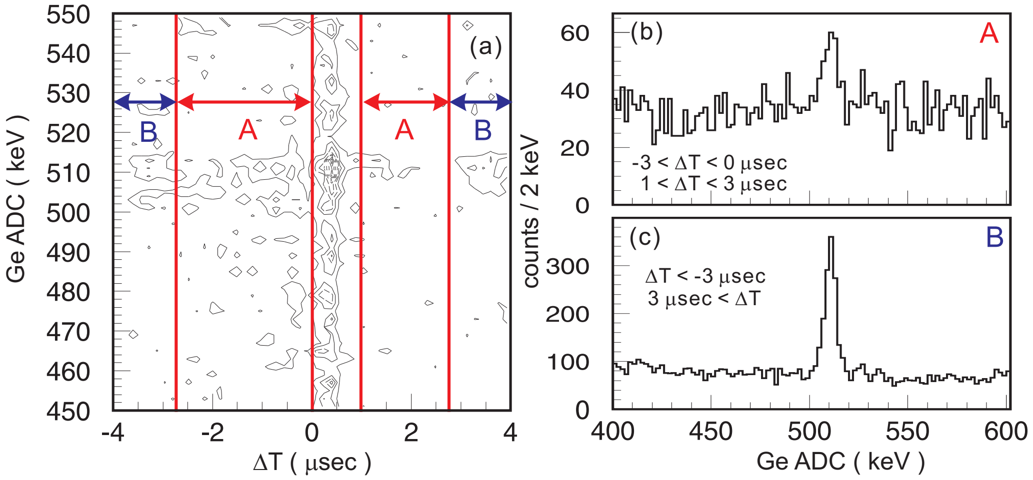

Figure 3.18: (a) The correlation between the time difference of subsequent two γ-ray hits in the Ge TFA and the Ge ADC for the proper-timing hit. Region A ($-3 < \Delta T < 0$ and $1 < \Delta T < 3$ μsec) was selected for the pile-up rejection. Region B ($\Delta T < -3$ and $3 < \Delta T$ μsec) is out of the region for the rejection. (b) The ADC spectra for the proper-timing hit of the Ge detectors measured from the region A. (c) The ADC spectra for the proper-timing hit of the Ge detectors measured from the region B.

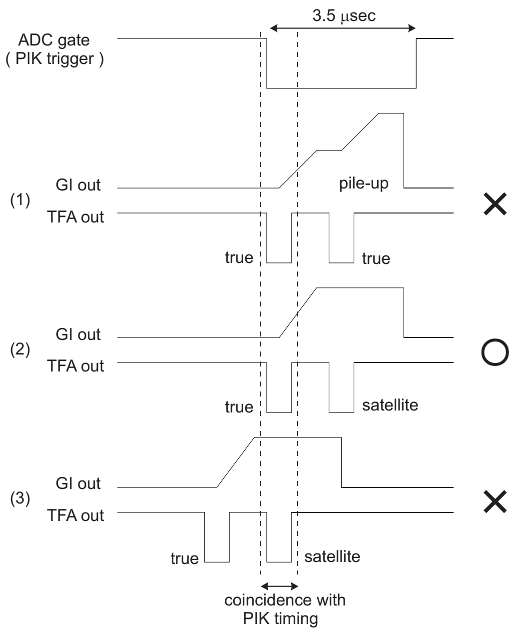

Figure 3.19: Illustration for the pile-up rejection. The timing for the ADC gate was determined by the PIK trigger. Figure shows the gated-integrator and TFA outputs for the event which has (1) two true hits within 3 μsec, (2) one true hit with a satellite component after the beam timing and (3) one accidental hit with a satellite component in the beam timing. (1) and (3) should be removed by the pile-up rejection.

3.2 Energy calibration

The energy calibration of the Ge detectors was performed several times during the experiment using ^{152}Eu and ^{60}Co sources. As shown in Table 3.2, we used γ rays from 121 keV to 1528 keV. The fourth-order polynomial was used to fit the energies. Because the peak position was typically 1 keV lower during the in-beam period than the off-beam period, the calibration curve was adjusted by comparing data taken with the CALIB trigger (see §6 in Chapter 2) in the in-beam and the off-beam periods. This effect is originated from the high counting rate of the Ge detectors. The various γ-ray peaks produced by incident π^+ beams during the in-beam period were used to confirm the calibration. Among these γ rays, the one where the effect from the Doppler effect is expected to be small was shown in Table 3.3. The residuals for these measured γ-ray energies were shown in Fig. 3.20. Then, the calibration error was estimated to be ±0.6 keV. In order to confirm the reliability at the higher energy region, we mea-

Table 3.2: γ-ray sources for the off-beam energy calibration.

Source	γ-ray energy
^{152}Eu	121.78 keV
^{152}Eu	244.7 keV
^{152}Eu	344.28 keV
^{152}Eu	411.12 keV
^{152}Eu	443.96 keV
^{152}Eu	411.12 keV
^{152}Eu	778.9 keV
^{152}Eu	867.37 keV
^{152}Eu	964.08 keV
^{152}Eu	1085.9 keV
^{152}Eu	1112.1 keV
^{60}Co	1173.24 keV
^{60}Co	1332.52 keV
^{152}Eu	1408.0 keV
^{152}Eu	1528.1 keV

Table 3.3: Observed γ rays during the in-beam period where the Doppler effect is expected to be small. Error in measured energy is statistical only.

Measured energy (keV)	Source	γ-ray energy (keV)
414.3 ± 0.06	^{10}B	414.1
510.6 ± 0.02	e^+e^-	511.0
717.7 ± 0.03	^{10}B	718.3
1021.1 ± 0.1	^{10}B	1021.7
1039.0 ± 0.2	^{70}Ge	1039.2
1237.8 ± 0.3	^{56}Fe	1238.3
1435.6 ± 0.15	^{10}B	1435.8
1608.6 ± 0.4	^{209}Bi	1608.5
2154.6 ± 0.4	^{10}B	2154.1

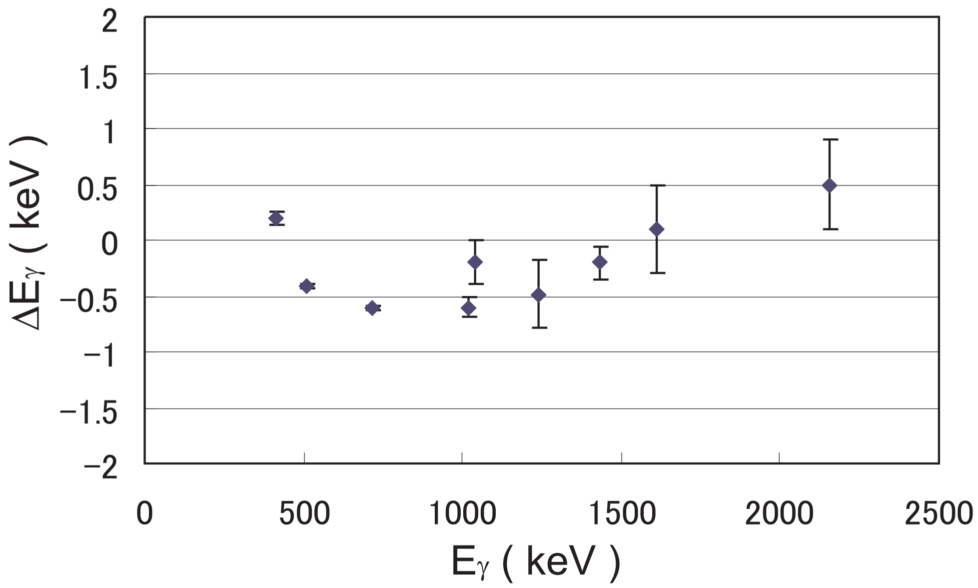

Figure 3.20: Residuals of the measured γ-ray energies in Table 3.3. Measured energies were not used for the calibration.

sured the γ rays from ^{16}O (6129 keV) by irradiating the 1.05-GeV π^+ beam onto the H_2O target.

The long term stability of the peak position of the Ge detectors was estimated using γ rays from ^{10}B (718 keV) and ^{10}B (1436 keV) as shown in Fig. 3.21. During the experimental terms, the peak position drifted within $\pm$0.7 keV.

The energy resolution of the Ge detectors was estimated from the γ rays which is not broadened by the Doppler effect. The γ rays of ^{10}B (718 keV) and ^{60}Co (1173, 1333 keV) were used for the estimation and the results were summarized in Table 3.4. Here, the γ rays from ^{60}Co (1173, 1333 keV) were measured by the CALIB trigger.

Table 3.4: Energy resolution of the Ge detectors measured for the in-beam period.

Source	γ-ray energy	Resolution (FWHM)
^{10}B	717.7 keV	4.37 $\pm$ 0.21 keV
^{60}Co	1173.24 keV	5.05 $\pm$ 0.07 keV
^{60}Co	1332.52 keV	5.07 $\pm$ 0.07 keV

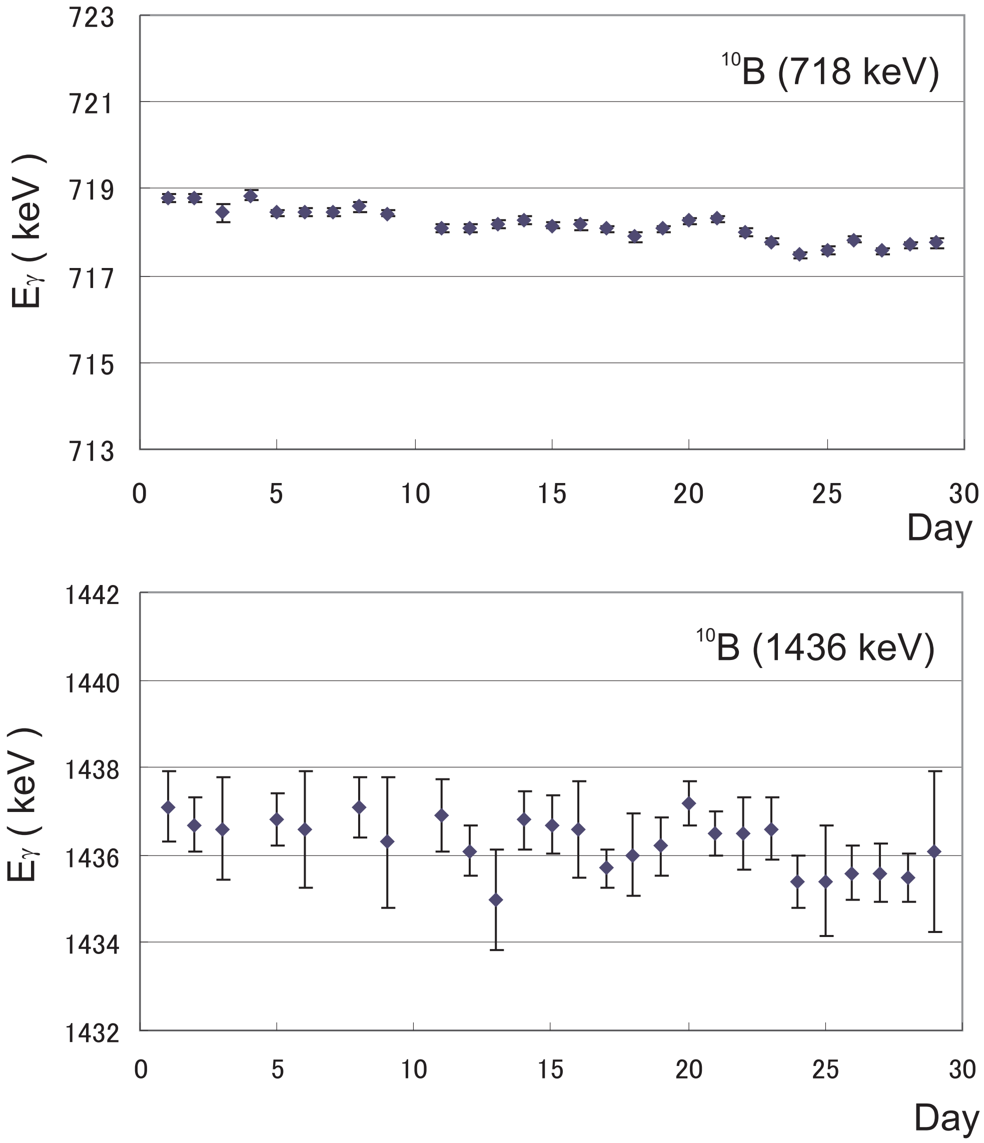

Figure 3.21: The long term stability of the peak position of the Ge detectors.

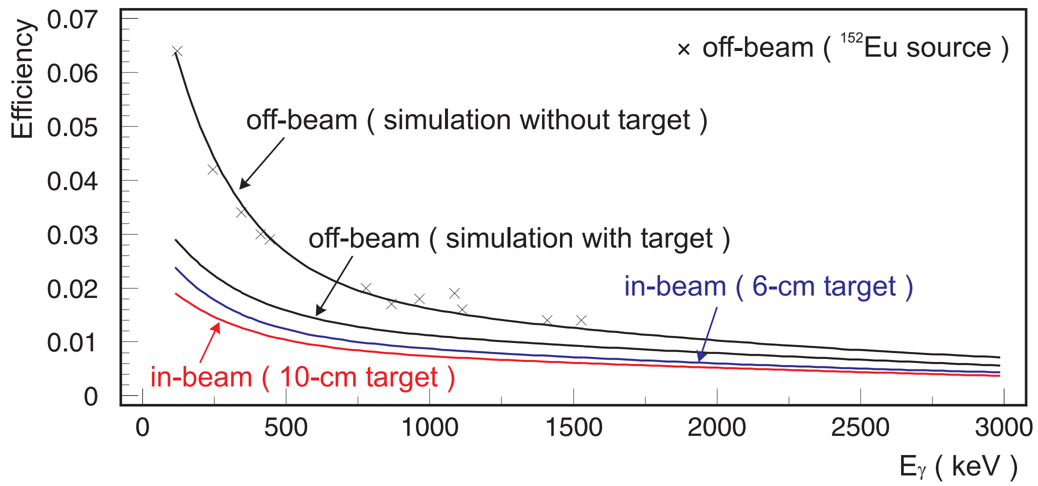

Figure 3.22: Total photo-peak efficiency of Ge detectors.

3.3 γ-ray detection efficiency

The absolute values of the photo-peak efficiencies of the Ge detectors were estimated from the γ-ray detection rate for a standard ^{152}Eu source. The ^{11}B target was removed and the source was placed at several points in the space for the ^{11}B target volume. By taking average of these points, the total photo-peak efficiency was obtained as shown in Fig. 3.22. In order to extend this result to higher energy region, the energy dependence of the photo-peak efficiency was simulated using GEANT4. Since the magnitude of the simulated efficiency curve was typically 1.5 times larger than that from the measured points, the magnitude was adjusted to reproduce the measured efficiency as shown in Fig. 3.22. The simulated result reproduced the energy dependence of the measured efficiency well.

The γ-ray absorption in the target was also taken into account. The difference between with and without the target was estimated by the simulation. The accuracy in the simulation was mainly determined by the geometrical position of the Ge detectors and estimated to be 10% for the energy region lower than 2500 keV.

Because of the high counting rate, the live time of the Ge detectors during the in-beam period was worse than that of the off-beam period. The difference was estimated using γ rays from ^{60}Co, which were measured by the CALIB trigger (see §2.6). Considering all the analysis efficiencies, the in-beam live time was estimated to be 62.4 ± 2.1 % of the off-beam period for the 10-cm target and 72.6 ± 2.5 % for the 6-cm target. Then, the in-beam efficiencies were calculated for the 6-cm and 10-cm target as shown in Fig. 3.22.

The photo-peak efficiency of the Ge detectors was also estimated using γ rays from ^{10}B by taking the γ-γ coincidence. The γ rays observed in coincidence with the 414-keV γ ray gives an efficiency for the 13 Ge detectors out of 14. The efficiency for these detectors were 1.1 ± 0.2 % for 718-keV γ ray and 0.9 ± 0.2 % for 1022-keV γ ray. These results were consistent with the efficiency which was estimated from the ^{152}Eu source.

3.4 Doppler-shift correction

When γ rays are emitted during the slowing down process of the recoiling nucleus, the γ-ray energies measured by the Ge detectors are shifted due to the Doppler effect. Since the momentum vectors of the incident and the outgoing particles were measured using the magnetic spectrometers, this effect can be corrected for every events. The Doppler shift was corrected using the momentum vector of the recoiling nucleus when the nucleus was produced, which is different from the momentum when the γ rays were emitted. Therefore, this correction is useful for the transition whose lifetime is short enough.

The γ-ray energies can be corrected using the following equation,

$$E_\gamma^{corrected} = \frac{1 - \beta\cos\theta}{\sqrt{1-\beta^2}} \cdot E_\gamma^{measured}, \tag{3.13}$$

where $E_\gamma^{corrected}$, $E_\gamma^{measured}$, β and θ are the corrected and the measured γ-ray energies, the velocity of the recoiling nucleus calculated by Eq. (3.11) and the angle between the directions of the γ ray and the recoiling nucleus, respectively. The direction of the γ ray was determined by the measured vertex position and the geometrical position of the Ge crystal. The position of the crystal is defined as the center of the volume. Therefore, the accuracy of this correction is mainly determined by the vertex resolution and the size of the crystal.

3.5 Doppler-shift attenuation method (DSAM)

When the lifetime of the γ-ray transition is comparable to the stopping time of the recoiling $^{11}_{\Lambda}$B, it can be measured by the Doppler-shift attenuation method (DSAM). The lifetime was derived by fitting the measured γ-ray peak with simulated peak shapes. Although the timing when the γ ray was emitted cannot be measured, the peak shape can be simulated using a Monte-Carlo method by assuming a certain lifetime. For a certain lifetime, the velocity of $^{11}_{\Lambda}$B when the γ rays were emitted was estimated from measured velocity of $^{11}_{\Lambda}$B (β), which was 0.03 – 0.04 (Fig. 3.15) as discussed in 2.6. Then, the stopping time was calculated from β using the stopping power in the target given by the SRIM code [50]. For such a velocity region, the stopping power is usually calculated from the empirical fitting formulae developped by Anderson and Ziegler in the SRIM code. Figure 3.23 shows a velocity dependence of the stopping time of $^{11}_{\Lambda}$B. Here, the accuracy of this code was reviewed by comparing existing experimental data and the stopping power given by the SRIM code (see Fig. 3.24). The accuracy of the stopping power is typically 5.4 %. The lifetime can be measured around the typical stopping time of 1.5 psec

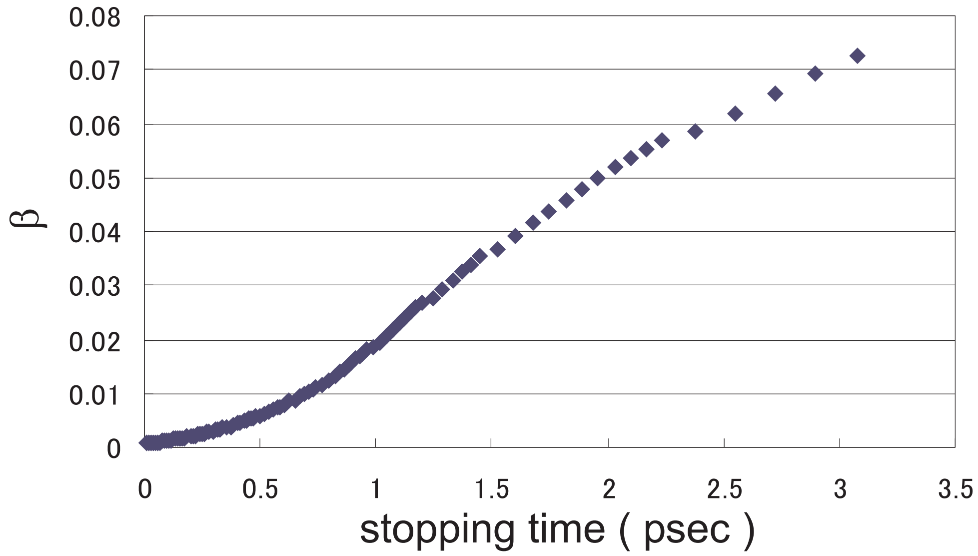

Figure 3.23: Stopping time of ${}^{11}_{\Lambda}$B in the ^{11}B target as a function of the initial velocity (β) calculated using the SRIM code.

Monte-Carlo simulation

In order to fit the γ-ray peaks, we simulated the peak shape for several lifetimes. If the γ-ray transition is not affected by a feeding from higher-lying states via γ-ray cascade, the γ-ray emission rate decreases exponentially. The velocity of ${}^{11}_{\Lambda}$B when the γ rays were emitted was simulated for the given lifetime and the effect of cascade feeding was included in the systematic error.

In the simulation, we used the geometrical position of the Ge crystal, the measured velocity of the recoiling ${}^{11}_{\Lambda}$B and the vertex position. The direction of the γ rays was assumed to distribute uniformly. Then, we accepted the γ rays which had a hit in the Ge crystal volume. The energy resolution of the Ge detectors were estimated from Table 3.4. The effect of the radiation damage was estimated from the peak shape of the γ ray from ^{10}B (718 keV) and the ^{60}Co source (1173, 1333 keV). Simulated peak shapes for the lifetime of 0.1, 0.5, 1.0 and 7.5 psec were shown in Fig. 3.25.

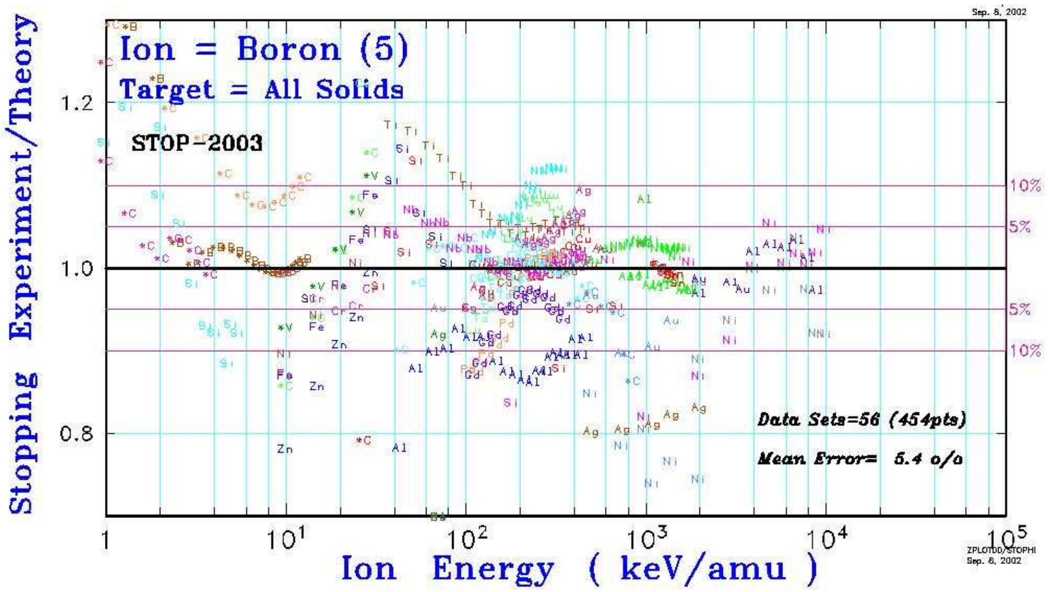

Figure 3.24: Stopping power of boron ion in various materials compared between the calculation by the SRIM code. Vertical axis is a ratio between the stopping power given by the SRIM code and the experimental data. The accuracy of the stopping power is typically 5.4 %.

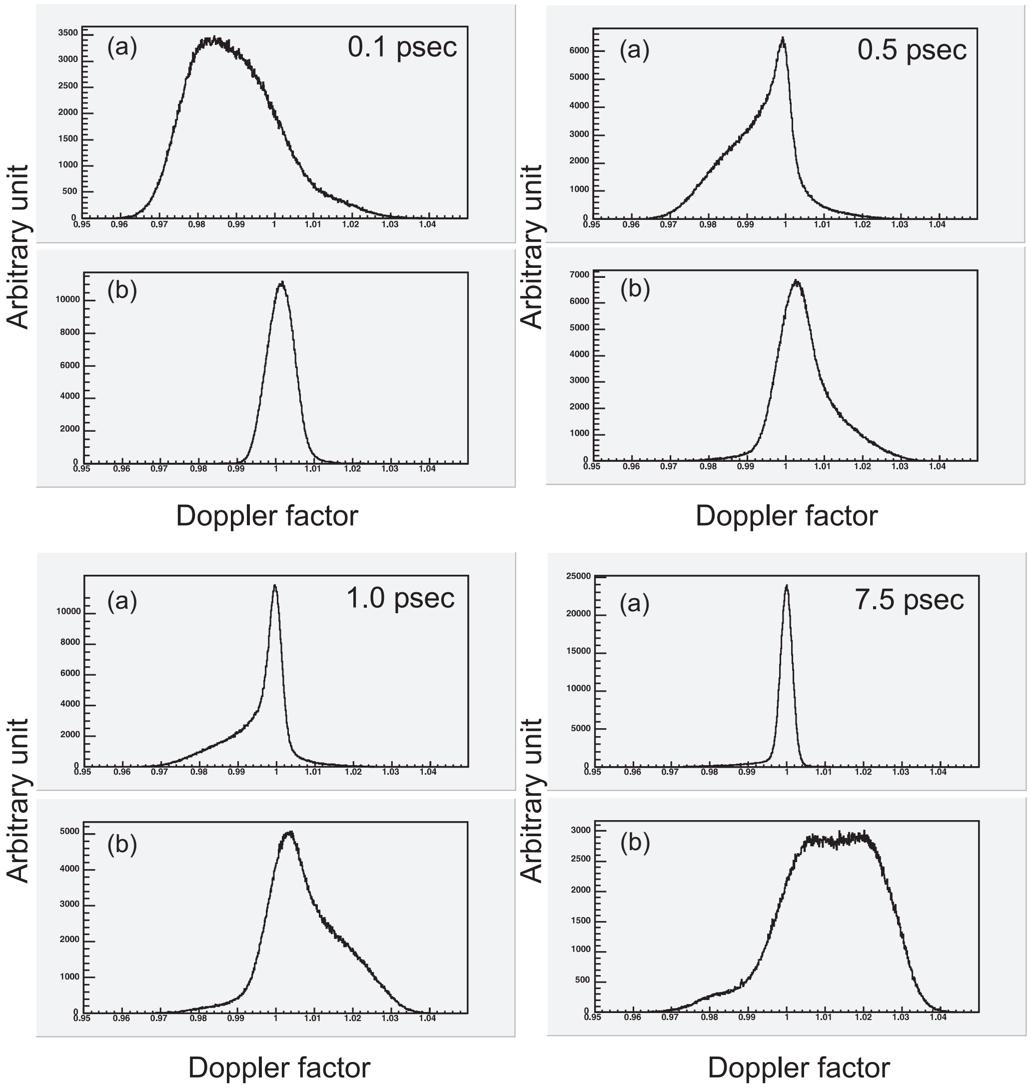

Figure 3.25: Simulated peak shapes for the lifetime of 0.1, 0.5, 1.0 and 7.5 psec. (a) Doppler effect is not corrected, (b) Doppler effect is corrected. The doppler factor is defined as $(1-\beta\cos\theta)/\sqrt{1-\beta^2}$. The energy resolution of the Ge detectors was included.

Chapter 4

γ-ray spectroscopy of ${}^{11}_{\Lambda}$B — Results

§ 1 Binding energy of ${}^{11}_{\Lambda}$B

The excitation energy spectrum of ${}^{11}_{\Lambda}$B via the (π^+, K^+) reaction was measured by the magnetic spectrometers. In order to measure the excitation energy with a good resolution, a measurement with a thin (2.38 g/cm^2) target was performed. The thin-target spectrum is shown in Fig. 4.1 (a). The horizontal axis of Fig. 4.1 has a scale of the binding energy of Λ (B_Λ) defined as $-B_\Lambda = M_{hyp} - M_\Lambda - M_{core}$. Here, M_{hyp}, M_Λ and M_{core} is the mass of the hypernucleus, the Λ and the core nucleus, respectively. Our experimental result was consistently reproduced with the theoretical calculation by Motoba as shown in Fig. 4.1 (c) [53]. In this calculation, the cross sections and the excitation energies of the states in ${}^{11}_{\Lambda}$B were obtained using a ΛN effective interaction which is calculated from the NSC97f model through G-matrix method. Here, the horizontal scale was adjusted at the ground state in ${}^{11}_{\Lambda}$B whose binding energy was determined in the previous experiment to be $B_\Lambda = 10.24 \pm 0.05$ MeV [47]. Figure 4.1 (b) shows the excitation energy spectrum obtained with the 6-cm (14.3 g/cm^2) and 10-cm (23.8 g/cm^2) targets. Then, the region "A" (-20 MeV $< -B_\Lambda < -2$ MeV) was selected to observe γ rays from ${}^{11}_{\Lambda}$B as the bound-state region where the excitation energy is lower than the particle decay threshold into a ${}^{10}_{\Lambda}$Be and a proton. The region "B" (20 MeV $< -B_\Lambda$) was selected as the unbound region.

§ 2 γ-ray energy spectrum

2.1 γ rays from ${}^{11}_{\Lambda}$B

Figure 4.2 shows the γ-ray spectra for the bound-state (Fig. 4.2 A) and unbound (Fig. 4.2 B) regions. By comparing the γ-ray spectra for the A and the B regions, six γ-ray peaks at 263.6 $\pm$ 0.5 (stat.) $\pm$ 1.1 (syst.) keV, 457.6 $\pm$ 1.2 $\pm$ 1.1 keV, 504.7 $\pm$ 1.0 $\pm$ 1.1 keV, 569.5.0 $\pm$ 0.5 $\pm$ 1.1 keV, 1483.3 $\pm$ 0.2 $\pm$ 0.7 keV and 2476.9 $\pm$ 2.1 $\pm$ 1.2 keV were identified as transitions from ${}^{11}_{\Lambda}$B because they were observed

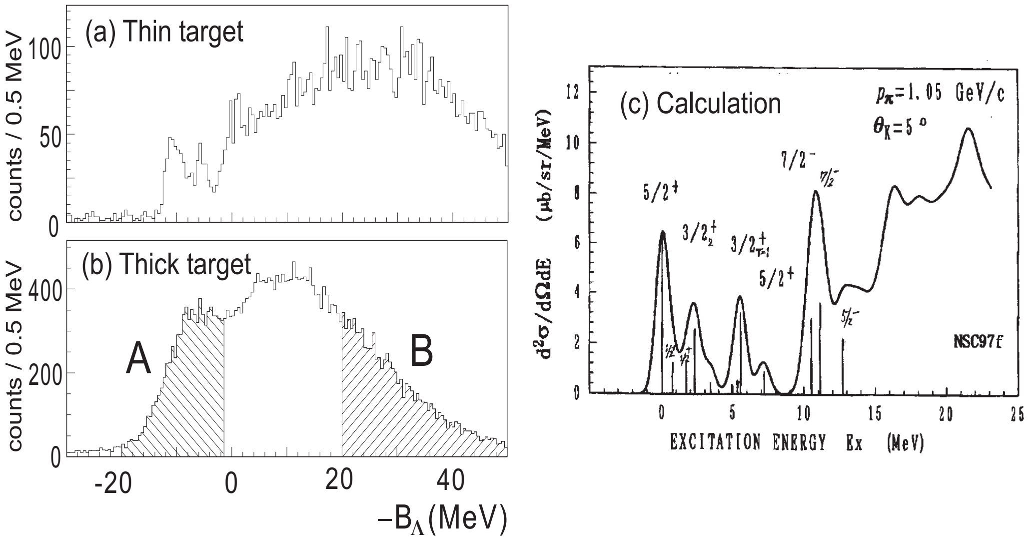

Figure 4.1: Excitation energy spectra of ${}^{11}_{\Lambda}$B. (a) Spectrum measured with the thin target (2.38 g/cm^2) and (b) with the thick targets. Horizontal axis has a scale of $-B_\Lambda$ (see text for details). The events in the region A (-20 MeV $< -B_\Lambda < -2$ MeV) of the spectrum (b) were selecled for the bound states of ${}^{11}_{\Lambda}$B, and the events in the region B (20 MeV $< -B_\Lambda$) were selected as unbound region. The energy loss of the incident and outgoing particles in the targets were corrected. The acceptance of the spectrometer is not taken into account. (c) Excitation energy spectra which is calculated by Motoba [53].

only in the spectrum for the bound-state region. Among these γ rays, the 2477 keV peak was observed after Doppler-shift correction.

The observed number of events and the relative intensity for each γ-ray transition are listed in Table 4.1. Since most of the observed peaks are wider than the Ge detector resolution, the γ-ray energies and the number of events were determined by fitting the spectrum with the peak shape which was calculated by a Monte-Carlo method taking Doppler shift into account (see §3 in Chapter 3). Then, the observed γ-ray peak was fitted with the lifetime as a parameter. In extracting the relative intensity, energy dependent efficiency of the Ge detector is taken into account (Fig. 3.22).

2.2 Systematic errors

The excited states, which are assumed to be directly populated by the (π^+, K^+) reaction, can also have a feeding from higher-lying states via γ-ray cascade. Since the target was not located at the center of Hyperball, the peak-shape difference affects

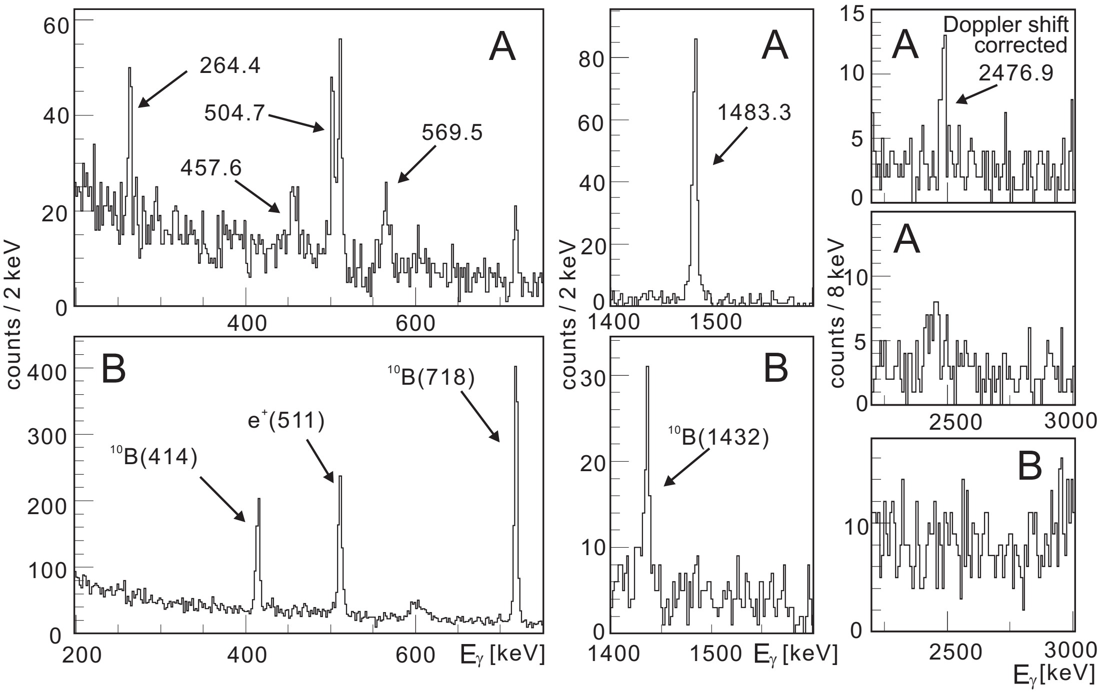

Figure 4.2: γ-ray spectra in the $^{11}\mathrm{B}(\pi^+, K^+)^{11}_{\Lambda}\mathrm{B}$ reaction. The Doppler shift effect is not corrected for all the spectra except for the top-right one. By comparing the spectra for the two regions, namely the bound-state region A (-20 MeV $< -B_\Lambda <$ -2 MeV) and the unbound region B (20 MeV $< -B_\Lambda$), six γ-ray transitions from $^{11}_{\Lambda}\mathrm{B}$ were observed. The 2477-keV peak was observed after Doppler-shift correction.

the γ-ray energy determined in the fitting. The effect of cascade feeding causes significant error; it is found to change the energy by less than 1 keV. Systematic errors of the γ-ray energies arising from uncertainty of the energy calibration was typically ± 0.4 keV. In addition, uncertainty of the measured vertex position, change of the peak shapes due to radiation damage of the Ge detectors, inaccuracy in the velocity, the stopping time of $^{11}_{\Lambda}\mathrm{B}$ and the angular correlation of the γ ray may also contribute to systematic errors. These effects were taken into account but estimated to be small (typically ± 0.2 keV). For the observed number of events in each peak, we considered uncertainty of the simulated peak shape and the background in the systematic error. For the relative intensity, the accuracy of the Ge-detector efficiency was estimated from the simulation to be 10 % (see §3 in Chapter 3).

Table 4.1: Number of events and relative intensities for observed γ transitions. Relative intensities were normalized to the number of events for the 1483 keV γ ray.

	E_γ (keV)	Number of events	Relative intensity
(a)	$263.6 \pm 0.5 \pm 1.1$	$78 \pm 10 \pm 8$	$0.14 \pm 0.02 \pm 0.02$
(b)	$457.6 \pm 1.2 \pm 1.1$	$50 \pm 9 \pm 5$	$0.12 \pm 0.02 \pm 0.02$
(c)	$504.7 \pm 1.0 \pm 1.1$	$114 \pm 11 \pm 9$	$0.28 \pm 0.03 \pm 0.04$
(d)	$569.5 \pm 0.5 \pm 1.1$	$89 \pm 10 \pm 7$	$0.23 \pm 0.03 \pm 0.03$
(e)	$1483.3 \pm 0.2 \pm 0.7$	$242 \pm 12 \pm 1$	1
(f)	$2476.9 \pm 2.1 \pm 1.2$	$30 \pm 5 \pm 1$	$0.16 \pm 0.03 \pm 0.02$

§ 3 γ-ray gated excitation energy

The excited states in ${}^{11}_{\Lambda}$B from which the γ rays are emitted were estimated by making an excitation energy spectrum for those events in which the γ rays were observed by the Ge detectors. Figure 4.3 (a)–(d) and 4.4 (e),(f) show the excitation energy spectra measured in coincidence with the 264-keV, 458-keV, 505-keV, 570-keV, 1483-keV and 2477-keV γ rays, respectively. In the right figure, the backgrounds were subtracted. Here, the background was obtained by choosing events in the γ-ray energy region slightly higher than each peak position with the same width as the peak regions. The spectra plotted for the γ ray from ^{10}B (718 keV) and for all the events were also shown in Fig. 4.4 (g) and (h). In these spectra, the lowest particle decay threshold into ${}^{10}_{\Lambda}$Be and a proton is located at $-B_\Lambda = -2.52$ MeV (Fig. 1.5). Since the horizontal scale was calibrated as disscussed in §2 in Chapter 3, we can see that the γ rays are obviously emitted from the bound states in ${}^{11}_{\Lambda}$B. Considering the energy-loss fluctuation in the targets, the resolutions of the hypernuclear mass spectrum were estimated to be 4.5 MeV (FWHM) for the 6-cm target and 5.8 MeV (FWHM) for the 10-cm target (see §2 in Chapter 3). Since the width of the bound state in Fig. 4.3 (e) is broader than the estimated resolution, we can see that the 1483-keV γ rays are emitted not only from a state which is produced via the (π^+, K^+) reaction directly but also from states which is produced by the cascade feeding from the higher excited states. For the other transition, such discussion is difficult because of low statistics.

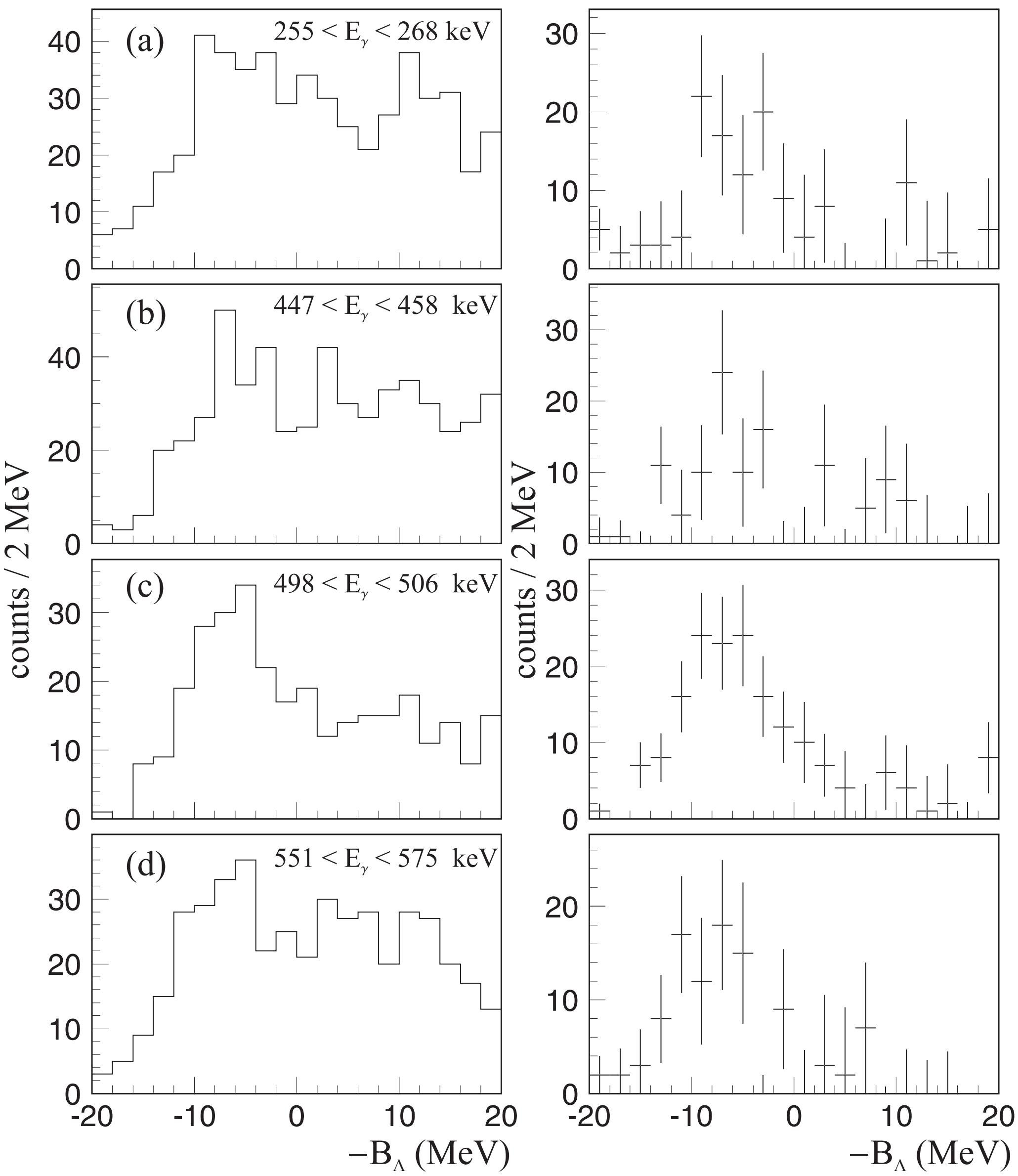

Figure 4.3: The excitation energy spectra of ${}^{11}_{\Lambda}$B plotted for those events in which the γ rays from ${}^{11}_{\Lambda}$B were observed. The corresponding γ-ray transition for (a)–(d) were shown in Table 4.1. In the right figure, backgrounds were subtracted by choosing events for the region slightly higher than the region for the γ rays from ${}^{11}_{\Lambda}$B.

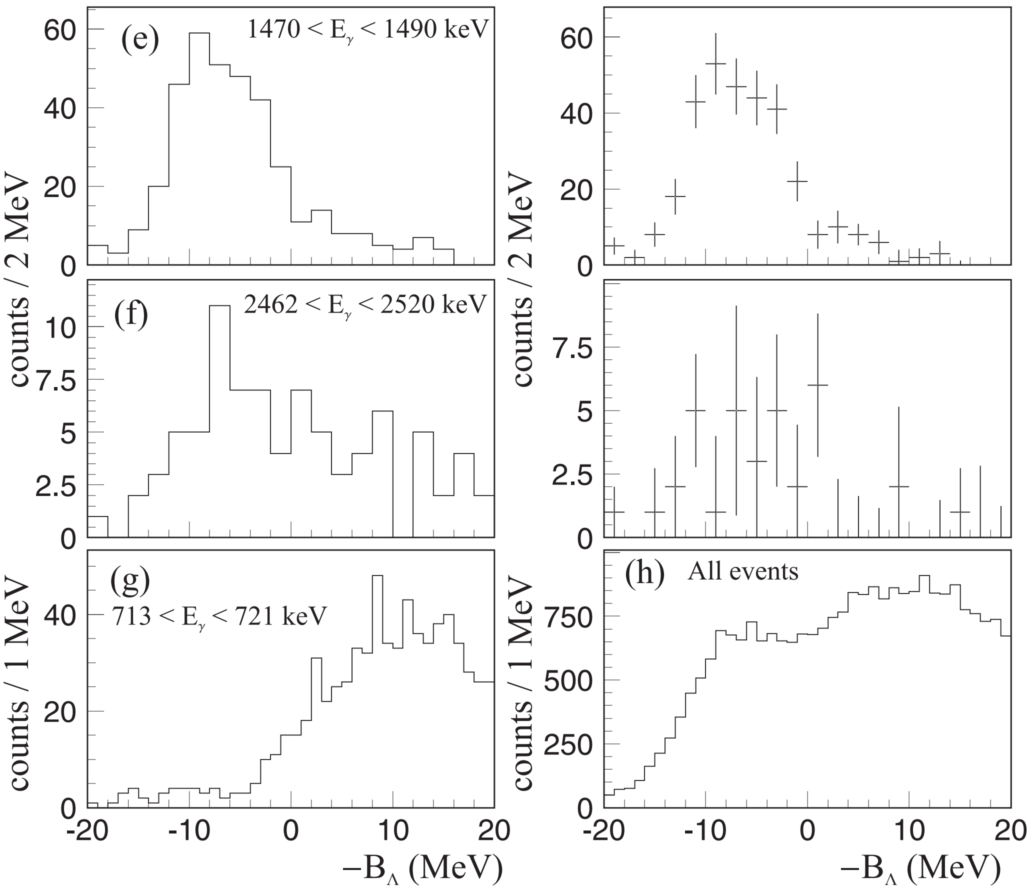

Figure 4.4: The excitation energy spectra plotted for those events in which the γ rays from ${}^{11}_{\Lambda}$B were observed (e),(f). The corresponding γ-ray transition for (e),(f) were shown in Table 4.1. The spectra for those events with the γ ray from ^{10}B (718 keV) (g) and for all the events (h) were also shown.

§ 4 Lifetime measurement

4.1 Lifetime of the γ-ray transitions in ${}^{11}_{\Lambda}$B

The lifetimes of the observed γ-ray transitions were estimated using the Doppler shift attenuation method (DSAM). For the 458-keV and the 570-keV transitions, the lifetimes were measured to be $0.6^{+0.7}_{-0.3}$ (stat.) ± 0.4 (syst.) psec and $0.5^{+1.0}_{-0.2} \pm 0.4$ psec, respectively. For the other transitions, experimental limit of the lifetime was determined with the confidence level of 68 % (1σ). The results of the fitting for each peak is shown in Fig.4.5 to 4.10 and the measured lifetime is summarized in Table 4.2.

The lifetime was determined by simultaneously fitting two spectra, before and after the Doppler-shift correction. The lifetime, the γ-ray energies and the number of events were parameterized and the resolution of the Ge detectors was fixed for each peak. In addition to them, two parameters which discribe the linear background were also introduced. For the 500-keV peak, the existence of the 511-keV peak was taken into account and the number of events in the 511-keV peak was also parameterized.

In order to estimate the statistical error, the spectra before and after the Doppler-shift correction were fitted individually, because these spectra are not completely independent. The statistical errors were estimated by considering the fitting results for both of these spectra. The γ-ray energy and the number of events were fixed to the values obtained by the simultaneous fitting. The systematic errors for the lifetime measurement will be described in the next section.

Table 4.2: Lifetimes of the observed γ transitions in ${}^{11}_{\Lambda}$B. (a) statistical error only, (b) statistical + systematic error, (c) contribution from the γ-ray cascade feeding was considered.

E_γ (keV)	lifetime (a) (psec)	lifetime (b) (psec)	lifetime (c) (psec)
263.6	> 3.5	> 1.0	> 1.0
457.6	$0.6^{+0.7}_{-0.3}$ (stat.)	$0.6^{+0.7}_{-0.3}$ (stat.) ± 0.4 (syst.)	< 1.6
504.7	2.8 ± 2.0 (stat.)	> 1.5	> 0.9
569.5	$0.5^{+1.0}_{-0.2}$ (stat.)	$0.5^{+1.0}_{-0.2}$ (stat.) ± 0.4 (syst.)	< 1.9
1483.3	> 15.0	> 6.0	> 6.0
2476.9	< 0.2	< 0.5	< 0.5

4.2 Systematic errors

γ-ray energy

Since the γ-ray energy was fixed in the fitting, the accuracy of the γ-ray energies affects the measured lifetime. In order to estimate the error, observed peaks were fitted by changing the energy within a statistical error. For the 458-keV and the 570-keV transitions, the error was estimated to be ± 0.1 psec. For the other transition, the error was included in the experimental limit of the lifetime which is shown in Table 4.2 (b).

Angular distribution of γ rays

In order to simulate the peak shape, we assumed an isotropic angular distribution of the γ-ray direction. However, since the spins of produced ${}^{11}_{\Lambda}$B are aligned by the (π^+, K^+) reaction, the emitted γ rays are expected to have a correlation against the spin-direction of the ${}^{11}_{\Lambda}$B. The angular distribution due to the spin alignment was estimated by assuming that the spins are fully aligned to the normal direction of the reaction plane. The multipolarity of the γ ray for the 1483-keV transition was assumed to be $E2$. For the other transitions, the multipolarity was considered to be $M1$. (see §5 for details.) Then, this effect was estimated to change the lifetime by ± 0.3 psec.

Effective volume of the Ge crystal

Since the effective volume of the Ge crystals was not precisely measured, its contribution to the lifetime has to be estimated as a systematic error. The size of the Ge crystals and the position of the BGO detectors may change the effective volume. Considering these effects, we have simulated the peak shape by changing the size of the crystal by $\pm 20\%$. Then, these effects were estimated to change the lifetime less than ± 0.1 psec.

Reaction vertex and position of Ge detectors

The accuracy of the measured vertex position and the geometrical position of the Ge detectors affects the measured direction of the γ rays. Considering the $\pm$ 5 mm offset in z-vertex, this effect was estimated to change the lifetime by ± 0.1 psec.

Stopping power

The stopping power of the recoiling ${}^{11}_{\Lambda}$B is calculated using the SRIM code (see §3 in Chapter 3). The accuracy of this calculation is estimated to be 5.4 % for the boron target [50]. Then, the effect was estimated to change the lifetime less than ± 0.1 psec. For the particle whose velocity is smaller than $0.5 \times 10^{-3} c$, the error in the stopping time is expected to be larger according to Ref. [50]. However, the contribution from this inaccuracy is negligibly small because the stopping time for such particle was calculated to be less than 0.01 psec.

Energy resolution of Ge detector

In order to simulate the peak shape, we fixed the energy resolution of Ge detector, which was estimated using the γ rays from the ^{10}B (718 keV) and the ^{60}Co source (1173, 1333 keV) (see §3 in Chapter 3). Therefore, the ambiguity of the resolution affects the accuracy in the lifetime measurement. The effect was estimated by changing the resoution by $\pm$ 10 %. The difference of the energy resolution contributes to the lifetime particularly for the peak which is not broadened by the Doppler effect. For the 458-keV and the 570-keV transitions, the error was estimated to be $\pm$0.1 psec

Radiation damage

The effect of the radiation damage gives a significant contribution to the measured lifetime. Since the target was placed at the downstream from the center of the Hyperball frame, the Doppler broadened peak has a low-energy tail which is difficult to distinguish from the effect of the radiation damage. The effect of the radiation damage was estimated using the γ rays from ^{10}B (718 keV) and the ^{60}Co source (1173, 1333 keV) (see §3 in Chapter 3). Then, the error was estimated to be $\pm$0.1 psec for the 458-keV and the 570-keV transitions.

γ-ray background

The measured lifetime can be affected according to the shape of the background function. By changing the parameters of the background, the systematic error was estimated to be $\pm$0.1 psec.

Feeding from γ-ray cascade

If two γ rays are successively emitted, the observed peak shape for the lower transition is affected by the lifetime of both transitions. By observing the lifetime and the yield of these γ rays, this effect can be estimated. However, since the spin assignment was not successful in the present study, the effect was estimated using the expected level structure calculated by Millener, which is shown in Fig. 1.5 [3]. This effect was estimated separately from the other systematic errors because it may cause unnecessarily large errors.

In this experiment, the order of the lifetime which we can measure was typically 1 psec. Therefore, the contribution from the states higher than $3/2^+_3$ in Fig. 1.5 were eliminated from the consideration because the lifetime of these states are mainly determined by an $M1$ transition to the states around the ground state and expected to be less than 0.1 psec. The most significant contribution was estimated from the $1/2^+_2 \to 3/2^+_1 \to 1/2^+_1$ transitions using the calculated values of the (π^+, K^+) cross section and the lifetime for the low-lying states in ${}^{11}_{\Lambda}$B. Then, by assuming that the most of the γ rays were emitted via the higher excited states whose lifetime is 0.5 psec, the lifetime when the effect of the cascade feeding was taken into account was obtained as shown in Table 4.2 (c).

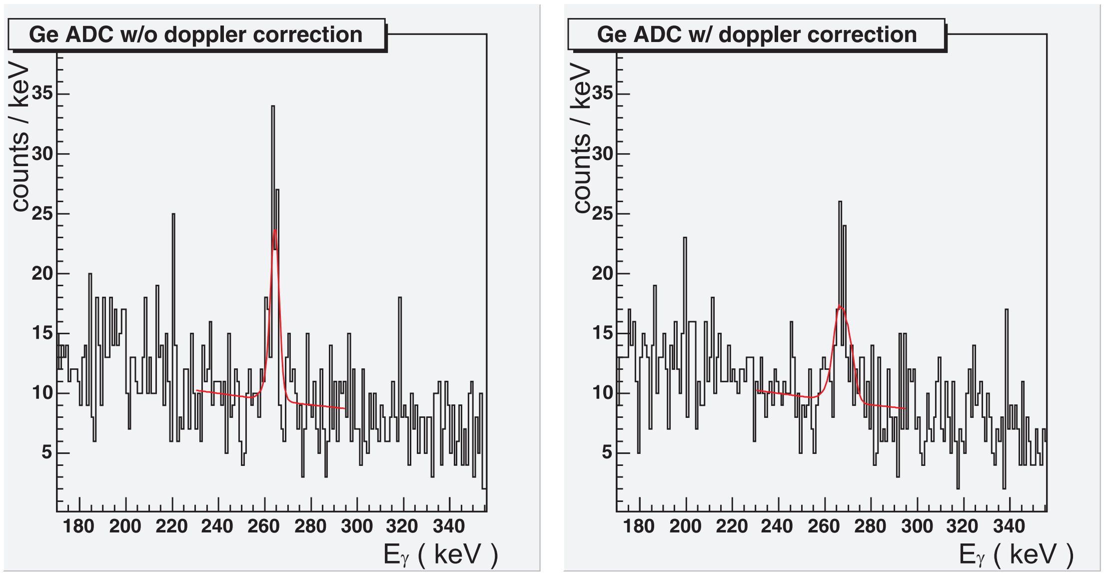

Figure 4.5: γ-ray energy spectrum for the 264-keV transition before (left) and after (right) the Doppler-shift correction. Fitting results were shown with the solid lines.

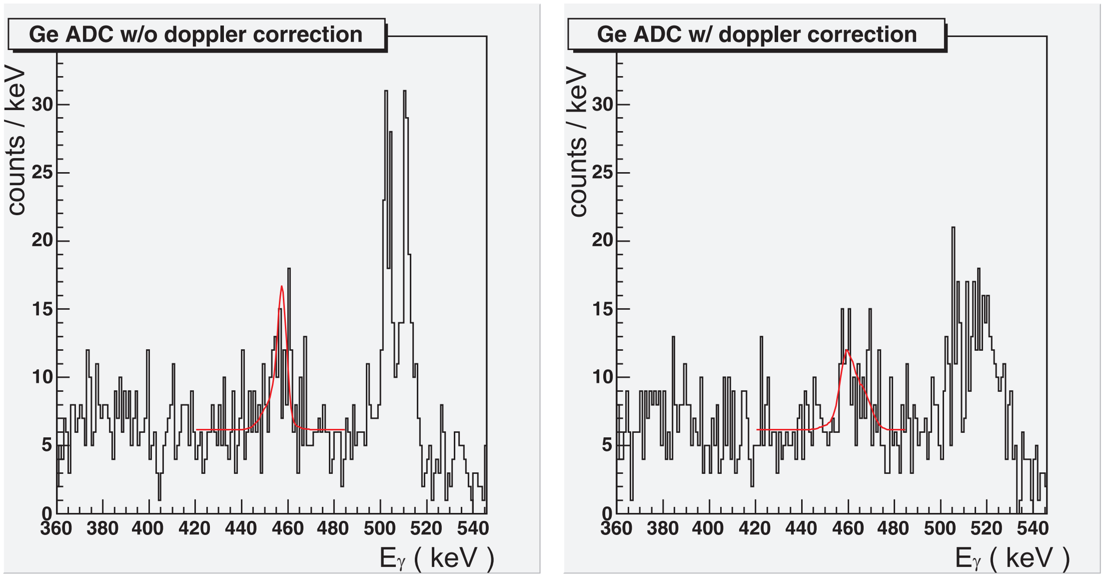

Figure 4.6: γ-ray energy spectrum for the 458-keV transition before (left) and after (right) the Doppler-shift correction. Fitting results were shown with the solid lines.

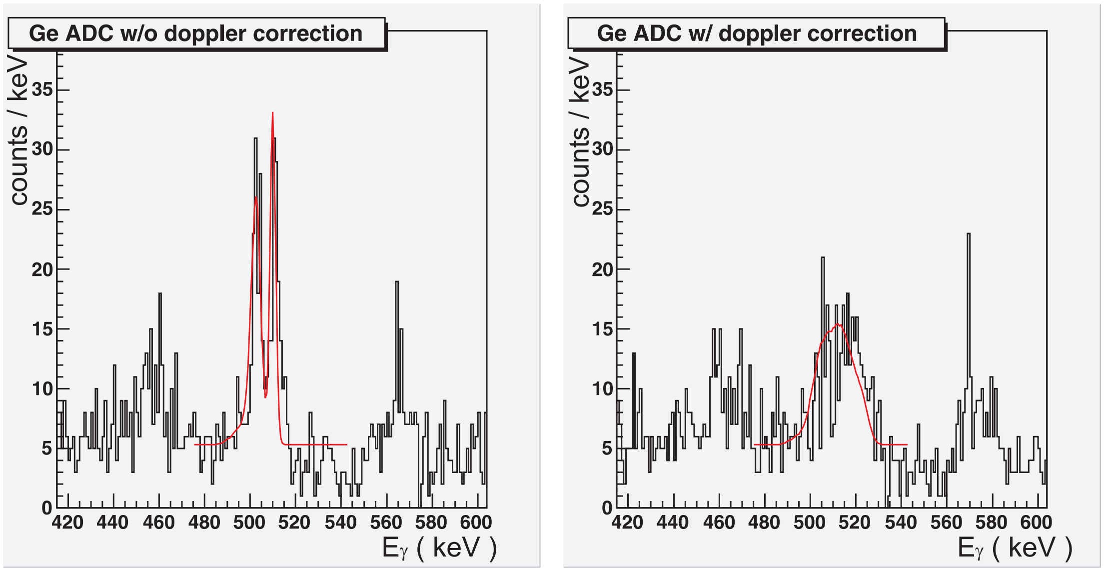

Figure 4.7: γ-ray energy spectrum for the 500-keV transition before (left) and after (right) the Doppler-shift correction. Fitting results were shown with the solid lines.

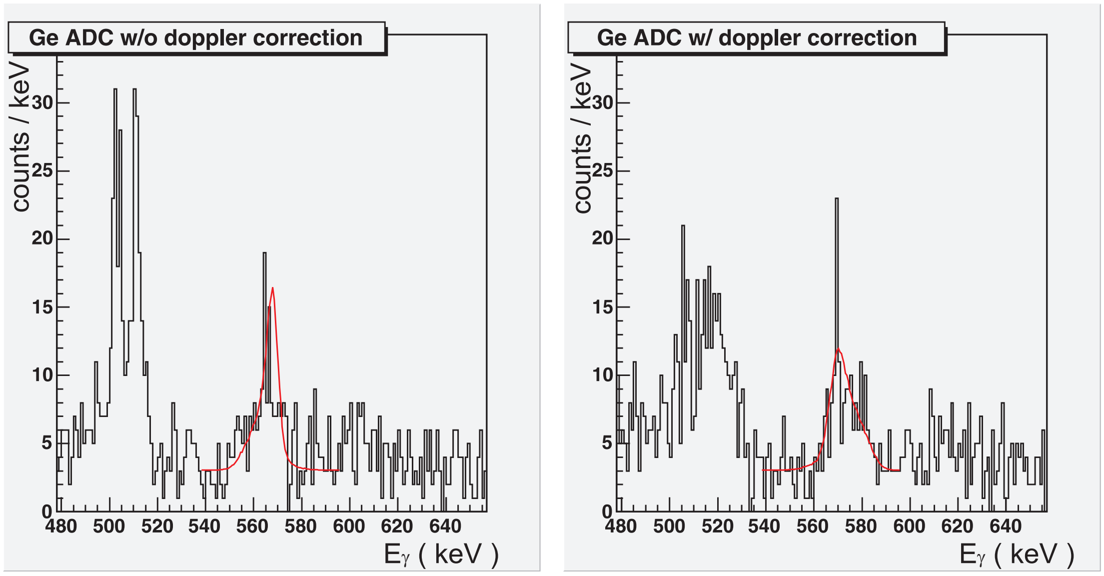

Figure 4.8: γ-ray energy spectrum for the 570-keV transition before (left) and after (right) the Doppler-shift correction. Fitting results were shown with the solid lines.

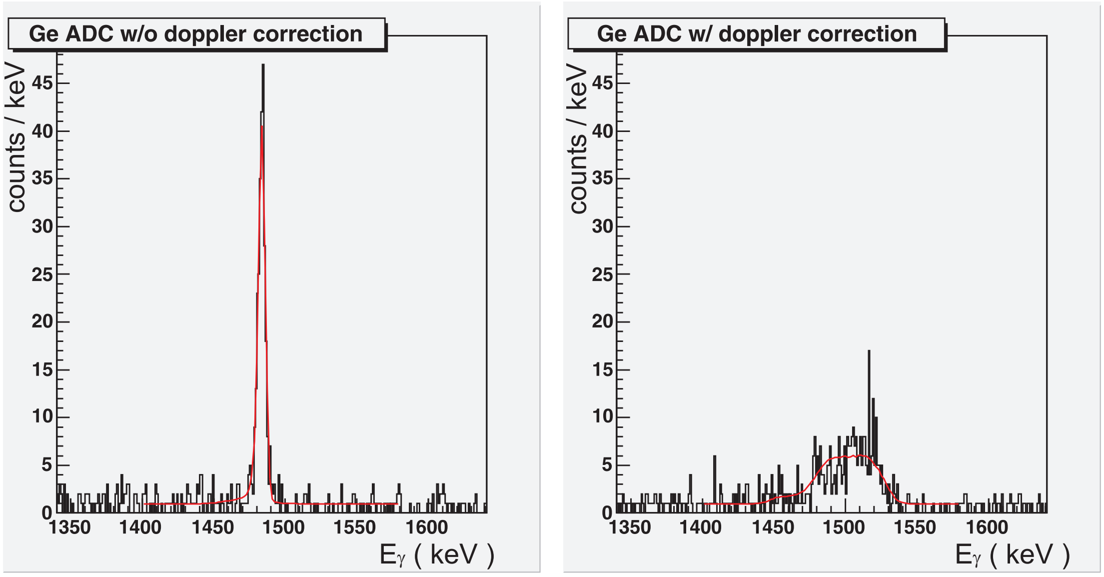

Figure 4.9: γ-ray energy spectrum for the 1483-keV transition before (left) and after (right) the Doppler-shift correction. Fitting results were shown with the solid lines.

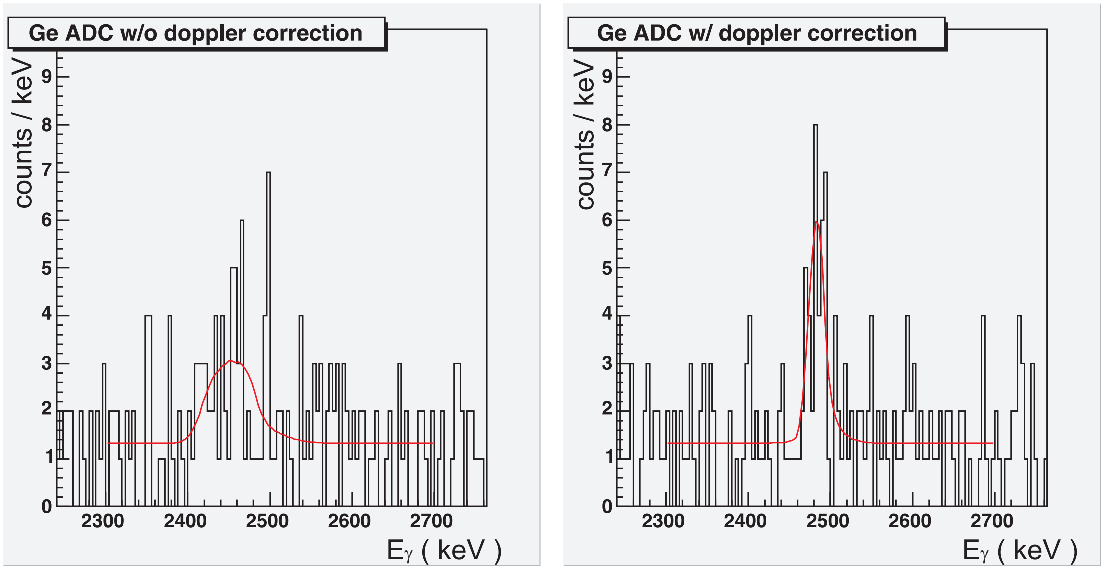

Figure 4.10: γ-ray energy spectrum for the 2477-keV transition before (left) and after (right) the Doppler-shift correction. Fitting results were shown with the solid lines.

Chapter 5

γ-ray spectroscopy of ${}^{11}_{\Lambda}\mathrm{B}$ — Discussion

§ 1 Properties of the observed γ rays

Among the observed γ rays, the 1483-keV transition has two notable characteristics in the lifetime and the γ-ray yield. Since the peak shape does not have a broadened component, the lifetime of the transition was estimated to be longer than 6 ps. If it is an $M1$ transition, its $B(M1)$ value is smaller than 1.6×10^{-3} [W.u.]. On the other hand, we obtain a reasonable value for $B(E2)$, which is smaller than 13 [W.u.]. Considering the structure of the core nucleus, ^{10}B, only $M1$ and $E2$ transitions are expected to be observed for the low-lying states of ${}^{11}_{\Lambda}$B (see Fig. 5.2). Therefore, the transition at 1483 keV is considered to be an $E2$ transition which does not mix with an $M1$ transition. In addition, as shown in Fig. 5.2, the spin values of the ground-state spin doublet are high ($5/2^+$ and $7/2^+$) and most of the other excited states are low ($1/2^+$ and $3/2^+$). It suggests that the final state of this γ-ray transition is either of the ground-state spin doublet members in ${}^{11}_{\Lambda}$B $(7/2^+, 5/2^+)$, where the ground-state spin is experimentally determined to be $5/2^+$ [51].

The initial state of the 1483-keV transition is the lowest excited state (S_1) except for the ground-state spin doublet. The $E2$ transition may compete with slow $M1$ transitions whose γ-ray energies are smaller than a few hundred keV. Consequently, if there is an excited state (S_2) whose excitation energy is slightly larger than S_1, such a state can also be an initial state of the 1483-keV γ ray because of a small $\mathrm{S}_2 \rightarrow \mathrm{S}_1$ $M1$ transition probability.

This assignment is consistent with the largest yield of all the observed γ-rays from ${}^{11}_{\Lambda}$B as shown in Table 4.1; the large γ-ray yield is explained by considering that the state is produced via the γ-ray cascade from higher excited states as well as the direct (π^+, K^+) reaction process. On the other hand, the lifetime of the transitions in ^{10}B may suggests that the core transition of the 1483-keV transition corresponds to $1^+ \rightarrow 3^+$ because the lifetime of this transition (0.7 ps) is longer than 6 ps and the lifetime is shorter for the other core transitions. However, the spin values of the initial and the final states cannot be conclusively identified from the present results.

The lifetime of the 2477-keV transition (< 0.5 ps) shows that the transition is an $M1$ transition. Since most of the γ-ray transition to the ground state is expected to occur via S_1 or S_2, the excitation energy of the initital state of the 2477-keV transition is considered to be larger than $1483 + 2477 = 3960$ keV. On the other hand, in the mass spectrum with a thin target, we found two peaks in the bound states region (Fig. 4.1 (a)). The narrow peak at B_Λ = 5–6 MeV ($E_{ex} \simeq 4$ MeV) was assigned to the $3/2^+; T = 1$ state because the large cross section is expected for this state (see Fig. 5.2). It is suggested that the γ-ray transition at 2477 keV is a transition from the $3/2^+; T = 1$ state to one of the ${}^{11}_{\Lambda}$B states coupled to the ^{10}B(1^+, 718 keV and 2154 keV) states.

The multipolarity of the 458-keV and the 570-keV transitions were also estimated from the lifetime to be $M1$ but their spin assignment is not possible. On the other hand, the 264-keV and the 505-keV transitions are less broadened by the Doppler effect and only the upper limit of the lifetimes are obtained. These transitions can be assigned to both of $M1$ and $E2$ transitions but $M1$ transition is more probable assignment because spin values of the most of the excited states, except for the ground-state spin doublet, are $1/2^+$ and $3/2^+$ and most of the transitions to the ground state are expected to occur via S_1 or S_2.

In order to establish a level scheme for all of the γ-ray transitions observed in the present study, it is necessary to use γ-γ coincidence method. However, it is impossible to use this method because of low statistics in the present data.

§ 2 Spin assignment

The spin assignment for states connected by the 1483-keV and the 2477-keV transitions is possible by assuming the weak coupling between the Λ and the ^{10}B core, whose structure is expected to be preserved in ${}^{11}_{\Lambda}$B. In this section, the possible candidates for the spin assignment are discussed.

2.1 1483-keV transition

Possible candidates for the assignment of the 1483-keV transition are (a) $1/2^+ \rightarrow 5/2^+$, (b) $3/2^+ \rightarrow 5/2^+$ and (c) $1/2^+; T = 1 \rightarrow 5/2^+$, where the core of the $1/2^+$ and the $3/2^+$ states is ^{10}B(1^+, 718 keV) and $1/2^+; T = 1$ is ^{10}B($0^+; T = 1$, 1740 keV) as shown in Fig. 5.1. The other possibility for the initial state, namely $1/2^+$ and $3/2^+$ where the core state is the ^{10}B(1^+, 2154 keV) and higher excited states than them, is excluded because such a large modification of the level ordering is not expected [3].

Among the three candidates, the shell-model calculation shows that (a) $1/2^+ \rightarrow 5/2^+$ is the most probable assignment for this transition [3]. However, if the energy spacing of the $(3/2^+, 1/2^+)$ is small, the 1483-keV transition may be assigned to (b) $3/2^+ \rightarrow 5/2^+$. Such modification is possible by considering other components of the orbital angular momenta in the ^{10}B (1^+) core wave function, which is mainly composed of $L = 0$ and $S = 1$ (see Appendix B).

In this case, the energy spacing between $3/2^+$ and $7/2^+$ is restricted by considering the transition probability. In the weak-coupling scheme, the $B(E2)$ value of the $3/2^+ \rightarrow 7/2^+$ transition is six times larger than that of the $3/2^+ \rightarrow 5/2^+$ transition (see Appendix C). The $E2$ transition probability ($\Gamma(E2)$) is expressed using the $B(E2)$ value in e^2fm^4 and the γ-ray energy (E_γ) in MeV as

$$\Gamma(E2) = 1.23 \times 10^9 \cdot B(E2) \cdot E_\gamma^5 \ [\mathrm{sec}^{-1}]. \tag{5.1}$$

Then, the γ-ray yield of the $3/2^+ \rightarrow 7/2^+$ transition ($Y(3/2^+ \rightarrow 7/2^+)$) is estimated to be,

$$Y(3/2^+ \rightarrow 7/2^+) = 6 \cdot \left(\frac{E_\gamma(3/2^+ \rightarrow 7/2^+)}{1483 \text{ keV}} \right)^5 \cdot \frac{\varepsilon\left(E_\gamma(3/2^+ \rightarrow 7/2^+)\right)}{\varepsilon(1483 \text{ keV})} \cdot Y(1483 \text{ keV}), \tag{5.2}$$

where ε is an energy-dependent γ-ray detection efficiency of the Ge detectors (see §3 in Chapter 3) and Y(1483 keV) is the observed number of event for the 1483-keV γ ray (see §2 in Chapter 4). Since two γ-ray transitions which satisfy the relation as $E(3/2^+ \rightarrow 7/2^+) + E(7/2^+ \rightarrow 5/2^+) = 1483$ keV were not observed, the yield of the $3/2^+ \rightarrow 7/2^+$ transition should be small so that the energy spacing of this transition is less than 580 keV. Therefore, if the 1483-keV transition is assigned to $3/2^+ \rightarrow 5/2^+$, the energy spacing of the $(7/2^+, 5/2^+)$ states is suggested to be larger than $1483 - 580 = 903$ keV.

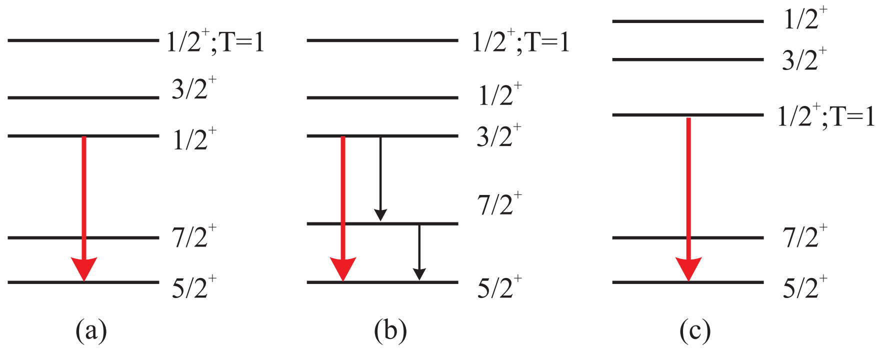

Figure 5.1: Possible candidates for the spin-assignment of the 1483-keV transition. p-type electrode is on the outside.

The possibility of the assignment to the $3/2^+ \rightarrow 7/2^+$ transition is excluded for the following reason. In this case, since the spin of the ground state in ${}^{11}_{\Lambda}$B is $5/2^+$, the energy spacing between $3/2^+$ and $5/2^+$ is larger than 1483 keV. Although the $3/2^+ \rightarrow 5/2^+$ transition was searched for in the γ-ray spectrum as a Doppler-unbroadened peak in the energy region higher than 1483 keV, the corresponding transiton was not found. Thus, the $3/2^+ \rightarrow 5/2^+$ yield was given to be less than 5 % of the $3/2^+ \rightarrow 7/2^+$ transition. Such a small branching ratio is not expected because the yield of the $3/2^+ \rightarrow 5/2^+$ transition is estimated using the weak-coupling scheme to be larger than 1/6 of the $3/2^+ \rightarrow 7/2^+$ transition.

2.2 2477-keV transition

The most probable assignment for the γ-ray transition at 2477 keV is $3/2^+; T = 1 \rightarrow 1/2^+$ where the $1/2^+$ state is based on the ^{10}B(1^+, 2154 keV) state, because the γ-ray energy is close to the 3010-keV energy spacing of the core states and the $B(M1)$ of the $3/2^+ \rightarrow 1/2^+$ transition is calculated to be five times larger than the $3/2^+ \rightarrow 3/2^+$ in the weak-coupling scheme (see Appendix C).

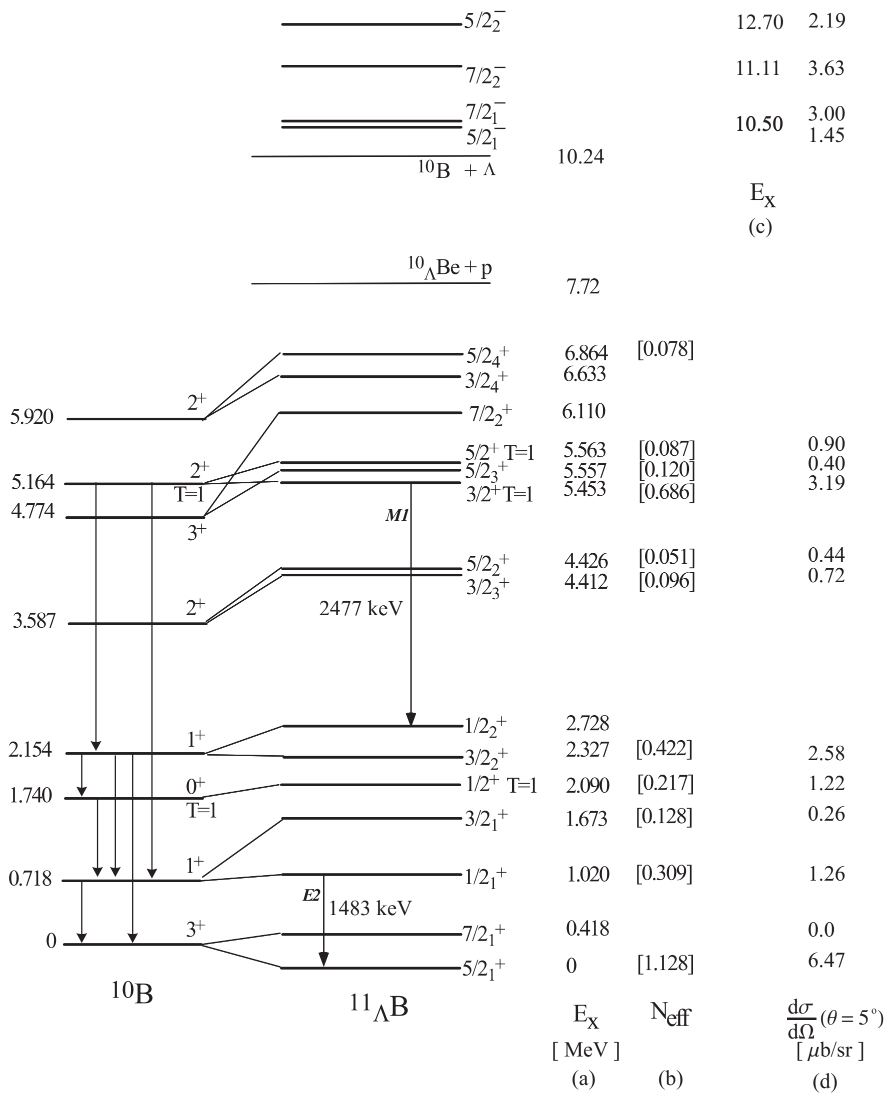

Figure 5.2: The most probable assignments for the 1483-keV and the 2477-keV transitions in ${}^{11}_{\Lambda}$B are shown with the calculated level scheme. The γ-ray transition to the ground-state spin doublet is expected to occur via the lowest excited state except for the ground-state spin doublet. (a) Excitation energies of low-lying states, (b) spectroscopic strengths for production of hypernuclear states by non-spin-flip transitions are calculated by Millener [3]. (c) Excitation energies of p_Λ states and (d) differential cross sections for the (π^+, K^+) reaction at the scattering angle of 5 degree are calculated by Motoba [53]. The core transitions which have substantial yields are shown in the left hand. The ordering of the hypernuclear states can be changed according to the configuration of the core states as well as the ΛN effective interaction parameters. The notation "$T = 0$" is omitted.

§ 3 Consistency of the ΛN effective interaction parameters

3.1 1483-keV transition

By assuming that the γ ray at 1483 keV corresponds to the ${}^{11}_{\Lambda}\mathrm{B}(1/2^+ \to 5/2^+)$ transition, which is the most probable assignment, the energy spacing can be compared with the shell-model calculation by Millener [3]. Using the Barker I interaction for the ${}^{10}\mathrm{B}$ core [36] and the four spin-dependent parameters of the ΛN effective interaction which were determined from the results of the previous experiments, the γ-ray energy of the E2$(1/2^+ \to 5/2^+)$ transition is predicted as

$$\begin{aligned} &E(1/2^+_1) - E(5/2^+_1) \\ &\qquad = -0.243\Delta + 1.234S_\Lambda - 1.090S_N - 1.627T + \Delta E_{core} + \Lambda\Sigma \\ &\qquad = 1020 \text{ [keV]}. \end{aligned} \tag{5.3}$$

Here, ΔE_{core} is the measured energy spacing of the core nuclear levels (718 keV) and $\Lambda\Sigma$ is calculated to be -4 keV. In this case, the energy spacing is mainly determined by the nucleon-spin-dependent spin-orbit interaction (S_N). The difference between the calculated and measured γ-ray energy is more than 400 keV. Since the energy spacing of these states is mainly determined by S_N, this parameter can be determined from the measured energy of 1483 keV.

Using the other parameters in Table 1.1, we obtain $S_N = -0.9$ MeV, which is much different from the value of -0.4 MeV obtained from ${}^{7}_{\Lambda}\mathrm{Li}$ [3]. All the other observed transitions, such as ${}^{13}_{\Lambda}\mathrm{C}$ $(3/2^+ \to 1/2^+)$ and ${}^{16}_{\Lambda}\mathrm{O}(1^- \to 1^-)$ can be consistently explained with the value of $S_N \sim -0.4$ MeV [4, 7, 6] but -0.9 MeV is unacceptable (Table 5.1). If the initial state of the 1483-keV transition is assigned to the $1/2^+; T = 1$ state, the energy spacing of the $(1/2^+, 5/2^+)$ states is larger than 1483 keV, which results in S_N smaller than -0.9 MeV.

If the 1483-keV transition is assigned to $3/2^+ \to 5/2^+$, the energy spacing of the ground-state spin doublet $(7/2^+, 5/2^+)$, which is mainly determined by the spin-spin interaction (Δ), is larger than 900 keV. In this case, we obtain $\Delta > 1.0$ MeV [3] while the parameter was obtained from the previous experiments to be 0.5 MeV [4]. This result is also inconsistent with the measured energy spacing of the ${}^{7}_{\Lambda}\mathrm{Li}$ $(7/2^+, 5/2^+)$ [7].

3.2 2477-keV transition

Considering the most possible candidate for the γ-ray transition at 2477 keV, $3/2^+; T = 1 \to 1/2^+$ where the $1/2^+$ state is based on the ${}^{10}\mathrm{B}(1^+$, 2154 keV) state, the energy spacing was compared with the shell-model calculation by Millener [3].

Table 5.1: The difference in the measured and the expected energy spacing of the hypernuclear levels measured in the previous experiments. These energy spacings have a strong contribution from S_N. The expected energy spacings are calculated by Millener [3]. The difference in $^{11}_{\Lambda}$B $(1/2^+_1 \to 5/2^+_1)$ is larger than the other results.

Transition	Measured spacing (keV)	Expected spacing (keV)
$^{7}_{\Lambda}$Li $(1/2^+_2 \to 1/2^+_1)$	3877 [4]	3779
$^{13}_{\Lambda}$C $(3/2^+ \to 1/2^+)$	4880 [6]	4831
$^{16}_{\Lambda}$O $(1^-_2 \to 1^-_1)$	6534 [7]	6435
$^{11}_{\Lambda}$B $(1/2^+_1 \to 5/2^+_1)$	1482	1020

The energy spacing between $3/2^+; T = 1$ and $1/2^+$ was calculated as

$$\begin{aligned} &E(3/2^+; T=1) - E(1/2^+) \\ &\qquad = -0.545\Delta - 0.050S_\Lambda - 0.116S_N - 2.118T + \Delta E_{core} + \Delta E'_{core} + \Lambda\Sigma \\ &\qquad = 2725 \text{ [keV]}. \end{aligned} \tag{5.4}$$

Here, ΔE_{core} is the measured energy spacing of the core nuclear levels (3010 keV) and $\Lambda\Sigma$ is calculated to be -69 keV. $\Delta E'_{core} = 46$ keV is originated from the configuration mixing of two $3/2^+$ states in $^{11}_{\Lambda}$B as we have discussed in Chapter 1. In this case, the energy spacing is mainly determined by Δ. If we determine Δ from this γ-ray energy, this parameter becomes 0.7 MeV. It is also much different from the value of 0.5 MeV obtained from $^{7}_{\Lambda}$Li.

3.3 ΛN effective interaction parameters

The present results imply that hypernuclear structure cannot be always reproduced consistently with the ΛN spin-dependent interaction parameters. More experimental and theoretical studies for various hypernuclear levels are necessary to understand the ΛN interaction and hypernuclear structure. In the present case, it is also conjectured that the wave functions of the core nucleus, ^{10}B, have to be improved. If the inconsistency can be explained by the modification of the core wave functions, it suggests a possibility that inaccuracy of the wave functions become visible by adding a Λ particle to the nucleus.

§ 4 $B(M1)$ measurement

In order to determine the $B(M1)$ from the measured lifetime, all of the branching ratios from the initial state and the cascade-feeding component from the higher states have to be measured. Since the spin assignment was not successful in the present study, the $B(M1)$ cannot be measured. By assuming that the branching ratio to the other states and the effect from the cascade feeding are negligibly small, the $B(M1)$ values for the observed $M1$ transitions from ${}^{11}_{\Lambda}$B were suggested as shown in Table 5.2. Here, 1483-keV transition was excluded because the multipolarity of this transition is an $E2$.

In the present study, systematic error due to the angular correlation of the γ ray was significantly large. In order to measure the $B(M1)$ in the future experiment, the systematic errors have to be reduced by measuring the angular distribution of the γ ray with higher statistics. The systematic errors due to the cascade-feeding and the branching ratio to the other states were also large. These effects can be removed if the spin assignment of the observed γ rays is confirmed by the future experiment.

In addition to these points, it is suggested that the $B(M1)$ should be measured for the transition which is well explained by the weak-coupling scheme because the magnetic moment of a Λ in the nucleus is derived from this framework (see §3 in Chapter 1). In this sence, ${}^{11}_{\Lambda}$B ($7/2^+ \to 5/2^+$) is the most suitable transition because the spin values are different from the other low-lying states. We are planning to measure the $B(M1)$ of this transition by observing γ rays emitted via the ${}^{12}_{\Lambda}\mathrm{C}^* \to {}^{11}_{\Lambda}$B ($7/2^+$) $+p$ process. In this case, the effect from the cascade feeding is negligible because only the ground-state spin doublet members are produced by this process.

Table 5.2: $B(M1)$ values for observed γ rays from ${}^{11}_{\Lambda}$B.

E_γ (keV)	Lifetime (psec)	$B(M1)$ (μ_N^2)
263.6	> 1.0	< 44.6
457.6	$0.6^{+0.7}_{-0.3} \pm 0.4$	$4.7^{+4.7}_{-2.5}$ (stat.) $^{+9.4}_{-1.9}$ (syst.)
504.7	> 1.5	< 1.2
569.5	$0.5^{+1.0}_{-0.2} \pm 0.4$	$1.9^{+1.3}_{-1.3}$ (stat.) $^{+7.6}_{-0.8}$ (syst.)
2476.9	< 0.5	> 0.001

Chapter 6

γ-ray spectroscopy of ${}^{10}_{\Lambda}\mathrm{B}$

§ 1 Overview

The energy spacing of the ground-state spin doublet in ${}^{10}_{\Lambda}\mathrm{B}$ $(2^-, 1^-)$ is mainly determined by the spin-spin force of the ΛN effective interaction. As we have mentioned in Chapter 1, the fact that no γ rays were observed for the transition between these states in an old experiment [8] is inconsistent with the spin-spin parameter which is determined from ${}^{7}_{\Lambda}\mathrm{Li}$ [4, 7]. In order to investigate this level spacing again, we performed a γ-ray spectroscopy experiment of ${}^{10}_{\Lambda}\mathrm{B}$ using Hyperball. A peak was searched for the γ-ray energy region from 60 keV to 470 keV where the γ rays from ${}^{10}_{\Lambda}\mathrm{B}$ is expected to be observed. However, no significant γ-ray peak was observed and a conclusive result on the energy spacing was not obtained because the fluctuation of background was not low enough compared with the expected yield for this γ-ray transition. In this chapter, the results of this experiment will be described.

§ 2 Experimental setup

The experiment (E930('01)) was performed at the D6 beam line of the Alternating Gradient Synchrotron (AGS) in the Brookhaven National Laboratory (BNL) (Fig. 6.1). The purpose of this experiment was to measure the γ rays from ${}^{16}_{\Lambda}\mathrm{O}$ via the (K^-, π^-) reaction. In this experiment, γ rays from the ${}^{10}_{\Lambda}\mathrm{B}$ was also measured using a ${}^{10}\mathrm{B}$ target. The momentum of K^- was 0.93 GeV/c and a typical beam intensity was $2{\times}10^5$ K^- per an extraction period of 1.5 second. The number of K^- at the target was three times larger than that of π^- by grace of the two-stage electrostatic separator.

The experimental setup was identical to that for the γ-ray spectroscopy experiment of ${}^{16}_{\Lambda}\mathrm{O}$ [7], which was performed in the beginning of the experimental term. The momenta of incident K^- and scattered π^- were measured with magnetic spectrometers (Fig. 6.2). The trajectory of each particle was reconstructed using drift chambers and was used to obtain the excitation energy and the recoil momentum vector of the produced ${}^{10}_{\Lambda}\mathrm{B}$. Subsequently, they were used for a selection of the events in which bound states of ${}^{10}_{\Lambda}\mathrm{B}$ were populated as well as for correction of γ-ray energies for Doppler shift.

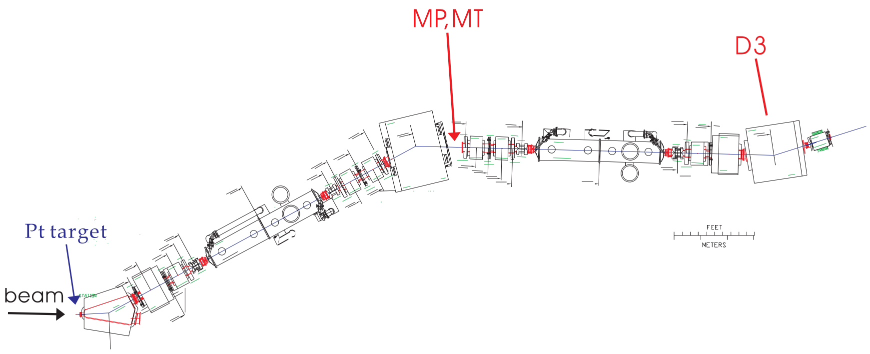

Figure 6.1: Schematic view of the BNL-AGS D6 beamline.

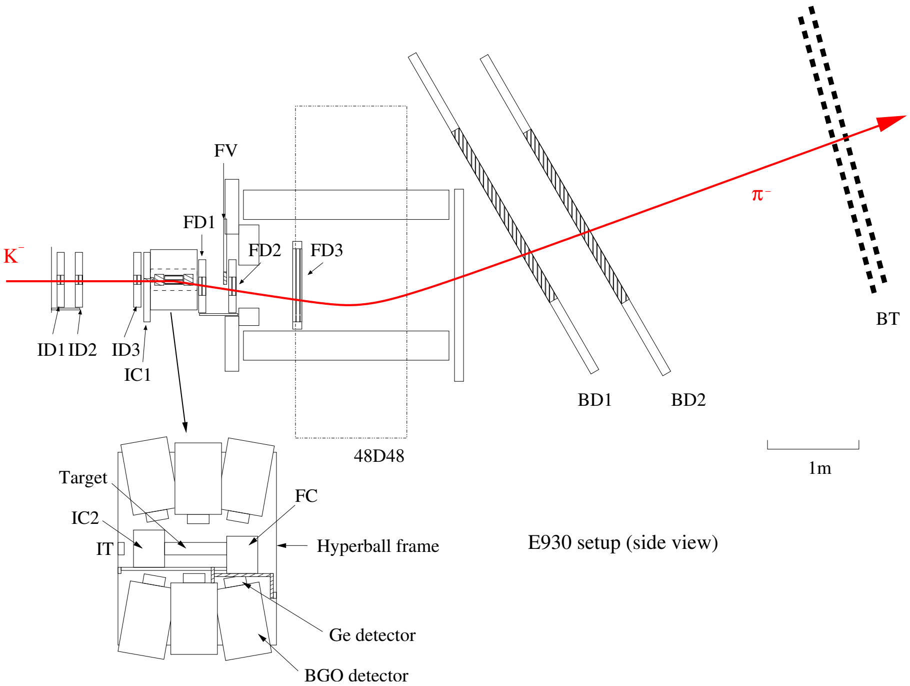

Figure 6.2: Schematic view of the BNL-AGS E930('01) setup around the target.

In order to measure γ rays from hypernuclei, we used Hyperball, which we have described in Chapter 2. The only difference of Hyperball setup between the ${}^{10}_{\Lambda}$B and the ${}^{11}_{\Lambda}$B experiment was the distance from the target to the Ge detectors, and the photo-peak efficiency was better than in the γ-ray spectroscopy of ${}^{11}_{\Lambda}$B. Details of the setup and the data analysis are described in Ref. [7, 52].

§ 3 γ rays from ${}^{10}_{\Lambda}$B

In order to observe γ rays from ${}^{10}_{\Lambda}$B, the bound-state region was selected from the excitation energy spectrum which was measured using the magnetic spectrometers. Figure 6.4 (a) shows the excitation energy spectrum whose horizontal scale is the binding energy of Λ (B_Λ). In this figure, the events originated from two decay processes, $K^- \to \pi^-\pi^0$ and $K^- \to \mu^-\nu$, were removed. Figure 6.5 (a) shows a scattering angle dependence of the excitation energy spectrum. In this spectrum, these K^- decay events are clearly observed. As shown in Fig. 6.5 (b), the backgrounds from decay of K^- were mostly removed by choosing a scattering angle in the (K^-, π^-) reaction as a function of the excitation energies. Considering the angular dependence of the (K^-, π^-) cross section, the events whose scattering angle was smaller than 2° were also removed. The energy losses of the incident and the outgoing particles in the target region were corrected using the calculated mean values of 1.97 MeV for K^- and 1.84 MeV for π^-.

Considering the energy resolution of the spectrometers, the region "A" (-20 MeV $< -B_\Lambda <$ 0 MeV) is selected as the bound-state region of ${}^{10}_{\Lambda}$B. The region "B" (50 MeV $< -B_\Lambda$) was selected as the unbound region. The energy resolution of the excitation energy spectrum was estimated to be 15 MeV (FWHM) [7]. The bound-state region was determined by using the excitation energies of ${}^{10}_{\Lambda}$B states which decay into ${}^{7}_{\Lambda}$Li ($5/2^+$) and ${}^{9}_{\Lambda}$Be ($3/2^+, 5/2^+$) as shown in Fig. 6.3. The γ rays from these states were observed by the Ge detectors [7]. Figure 6.4 (b) and (c) are the mass spectra which were measured in coincidence with the γ rays at 2050 keV for ${}^{7}_{\Lambda}$Li ($5/2^+ \to 1/2^+$), and around 3050 keV for ${}^{9}_{\Lambda}$Be ($3/2^+, 5/2^+ \to 1/2^+$), respectively. As shown in Fig. 6.3, the excitation energies of the states (3^- and others) which decay into ${}^{9}_{\Lambda}$Be ($3/2^+, 5/2^+$) are ~6 MeV and ~10 MeV higher than ${}^{10}_{\Lambda}$B (2^-). These excitation energies were measured by the (π^+, K^+) reaction in Ref. [54].

Figure 6.6 shows the γ-ray spectra measured for the "A" and the "B" regions. The γ-ray peak which corresponds to the transition between the ground-state spin doublet in ${}^{10}_{\Lambda}$B ($2^-, 1^-$) was not observed from the bound-state region with the confidence level of higher than 2σ.

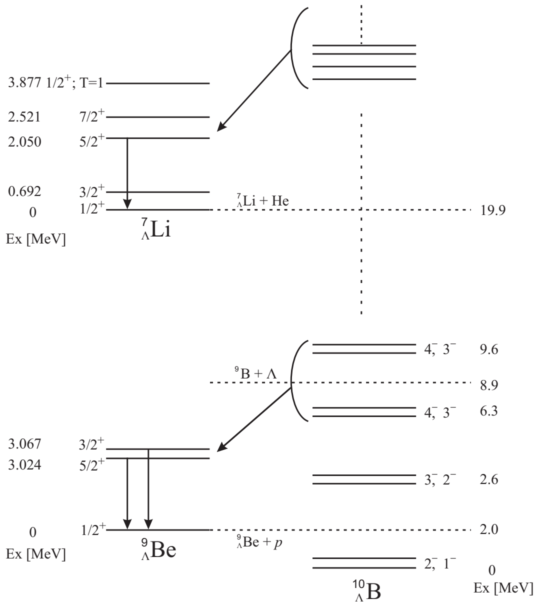

Figure 6.3: Expected level scheme of ${}^{10}_{\Lambda}$B. The bound state region was estimated from the mass spectrum which was observed in coincidence with the ${}^{7}_{\Lambda}$Li $(5/2^+ \rightarrow 1/2^+)$ and the ${}^{9}_{\Lambda}$Be $(3/2^+, 5/2^+ \rightarrow 1/2^+)$ transitions. The decay process to these transitions were also shown. Excitation energies of ${}^{10}_{\Lambda}$B were measured using the (π^+, K^+) reaction in Ref. [54]. For the ${}^{7}_{\Lambda}$Li and ${}^{9}_{\Lambda}$Be, the energies were measured by observing γ rays [7].

§ 4 Energy spacing of ${}^{10}_{\Lambda}$B $(2^-, 1^-)$

Considering the expected γ-ray yield for the transition between the ground-state spin doublet in ${}^{10}_{\Lambda}$B $(2^-, 1^-)$, the absence of a γ-ray peak in the observed spectrum may indicate that the energy spacing of the ground-state spin doublet is smaller than the experimental lower threshold energy for γ-ray detection. In order to investigate such a possibility, the expeced yield of the ${}^{10}_{\Lambda}$B $(2^- \rightarrow 1^-)$ transition was estimated from the measured yield of the ${}^{16}_{\Lambda}$O $(1^-_2 \rightarrow 1^-_1, 0^-)$ transitions and calculated (K^-, π^-) cross sections of ${}^{10}_{\Lambda}$B (2^-) and ${}^{16}_{\Lambda}$O (1^-_2). Since the experimental setup was identical for the ${}^{10}_{\Lambda}$B and ${}^{16}_{\Lambda}$O measurements, the contributions from the detector and analysis efficiency were expected to be the same. The remaining difference was the energy depenence of the Ge detector efficiency, the number of irradiated K^- and the number of the target nucleus.

Then, the expected yield for the ${}^{10}_{\Lambda}$B $(2^- \rightarrow 1^-)$ transition was estimated by the equation,

$$\begin{aligned} Y\left({}^{10}_{\Lambda}\mathrm{B}(2^- \rightarrow 1^-)\right) = Y\left({}^{16}_{\Lambda}\mathrm{O}(1^-_2 \rightarrow 1^-_1, 0^-)\right) &\cdot \frac{\varepsilon(E_\gamma)}{\varepsilon(6600\mathrm{keV})} \\ &\cdot \frac{N_{K^-}\,({}^{10}\mathrm{B})}{N_{K^-}\,({}^{16}\mathrm{O})} \cdot \frac{N_{targ}\,({}^{10}\mathrm{B})}{N_{targ}\,({}^{16}\mathrm{O})} \cdot \frac{\sigma\left({}^{10}_{\Lambda}\mathrm{B}(2^-)\right)}{\sigma\left({}^{16}_{\Lambda}\mathrm{O}(1^-_2)\right)} \cdot (1 - BR_{weak}), \end{aligned} \tag{6.1}$$

where Y, N_{K^-}, N_{targ} and σ are the γ-ray yield, the number of irradiated K^-, the number of the target nuclei and the cross section for the ${}^{16}_{\Lambda}$O and ${}^{10}_{\Lambda}$B states, respectively. BR_{weak} is the branching ratio of ${}^{10}_{\Lambda}$B going to the weak decay. The

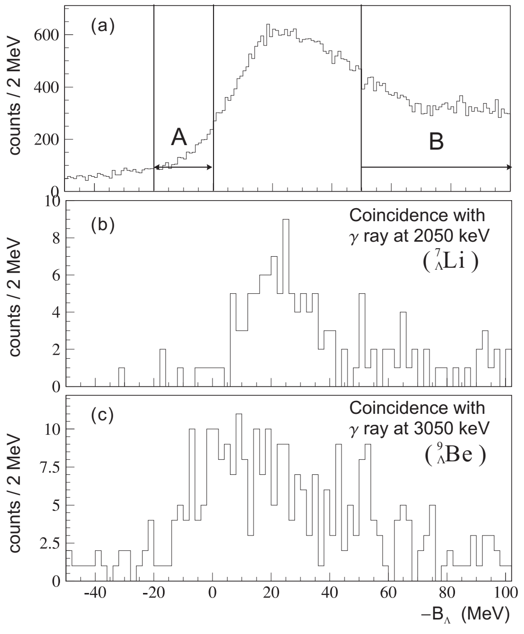

Figure 6.4: Excitation energy spectra of ${}^{10}_{\Lambda}$B. The events in the region A (-20 MeV $< -B_{\Lambda} < -5$ MeV) of the spectrum (a) were selected for the bound states of ${}^{10}_{\Lambda}$B, and the events in the region B (50 MeV $< -B_{\Lambda}$) were selected as the highly unbound region. (b) Spectrum obtained in coincidence with the ${}^{7}_{\Lambda}$Li ($5/2^+ \rightarrow 1/2^+$) γ ray, for which we set a gate from 2040 keV to 2060 keV. (c) Spectrum obtained in coincidence with the ${}^{9}_{\Lambda}$Be ($3/2^+, 5/2^+ \rightarrow 1/2^+$) γ ray, for which we set a gate from 3000 keV to 3100 keV. The acceptance of the spectrometer is not taken into account.

γ-ray detection efficiency relative to the 6.6 MeV γ ray ($\varepsilon(E_{\gamma})/\varepsilon(6600\text{keV})$) was estimated by a Monte-Carlo simulation by GEANT4 (Fig. 6.9). In the simulation, the γ-ray absorption in the target was taken into account. However, the simulation includes a large ambiguity because the photo-peak efficiency was not accurately measured, particularly for the high energy region. The relative efficiency can be changed in the simulation due to inaccuracy in the geometrical positions of the Ge detectors and the target. The ambiguity of the efficiency ratio in this simulation was estimated to be $\pm$ 30 %.

The γ-ray yield for the sum of two transitions, ${}^{16}_{\Lambda}$O ($1^-_2 \rightarrow 1^-_1, 0^-$), was 84 $\pm$ 12 counts (Fig. 6.7), which was obtained by choosing events from the excitation energy spectrum (-12 MeV $< -B_{\Lambda} <$ 8 MeV). The backgrounds from the decay of K^- were removed by choosing a scattering angle with the same cut condition as ${}^{10}_{\Lambda}$B. The total amount of irradiation was $0.56 \times 10^{10} K^-$ for ^{10}B and 3.94 $\times 10^{10} K^-$ for ^{16}O. The thickness of the targets was 14.2 g/cm^2 for ^{10}B and 20.0 g/cm^2 for H_2O.

The cross section of ${}^{10}_{\Lambda}$B (2^-) was estimated from a theoretical calculation by Motoba and Itonaga. In this calculation, the cross section for the 800 MeV/c K^- at the scattering angle of 6 degree was estimated to be 98 μb/sr for ${}^{10}_{\Lambda}$B (2^-_1, 3^-_1 and 3^-_2) [33, 34], which reproduces the result of the previous experiment [8]. Figure 6.8 shows the cross sections of the ${}^{10}_{\Lambda}$B (2^-) and the ${}^{16}_{\Lambda}$O (1^-_2) states for 930 MeV/c K^- calculated by Motoba [53]. According to this calculation, the cross section of ${}^{10}_{\Lambda}$B (2^-) was estimated to be five times smaller than that of ${}^{16}_{\Lambda}$O (1^-_2).

The branching ratio against the weak decay was estimated from the $B(M1)$ of the spin-flip $M1$ transition and the lifetime of the weak decay process ($\sim$200 psec). The $B(M1)$ value was calculated from Eq. (1.13) to be 1.78 [W.u.] [1] using the

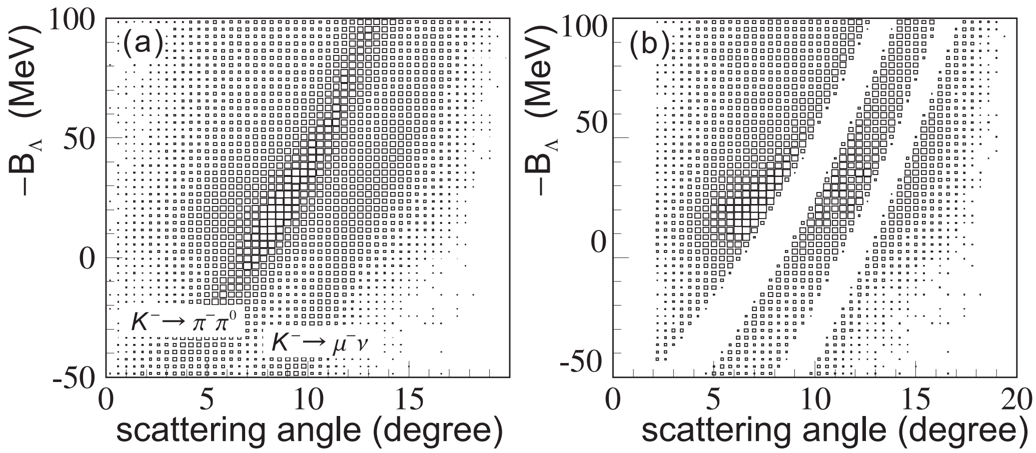

Figure 6.5: The (K^-, π^-) scattering angle dependence in the excitation energy of ${}^{10}_{\Lambda}$B. In (b), the backgrounds originated from the decay of K^- were removed.

g-factor of the ^{9}B$(3/2^-)$ core ($g_{core} = 1.99$ $[\mu_N]$) and that of a Λ in the free space ($g_\Lambda = -1.34$ $[\mu_N]$).

Then, the expected yield for the ${}^{10}_{\Lambda}$B $(2^- \rightarrow 1^-)$ γ ray (Y_1) was estimated as shown in Fig. 6.10. In this estimation, the errors from the γ-ray angular distribution, the accuracy in the efficiency of the Ge detectors, statistical error for the number of the γ rays from ${}^{16}_{\Lambda}$O (1^-_2), the difference between ${}^{10}_{\Lambda}$B and ${}^{16}_{\Lambda}$O in choosing events from the excitation energy and the scattering angle, and the accuracy of the calculated cross section has to be considered. Overall, the error $(\Delta Y_1/Y_1)$ was estimated to be ± 40 % of the expected yield.

The probability for the peak non-existence in Fig. 6.6 was tested for the γ-ray energy region from 60 keV to 470 keV in the following way.

- Determine the background function by fitting Fig. 6.6 with fourth-order polynomial from 50 keV to 480 keV.

- By assuming a peak on the background function at a certain energy, we fitted the spectrum again. The γ-ray peak was assumed to have a Gaussian shape whose width was determined by the energy resolution of Ge detector and the effect from the Doppler shift. The energy resolution of Ge detector was typically 4 keV (FWHM) for the energy region of less than 500 keV. The Doppler effect was estimated from the lifetime of the $2^- \rightarrow 1^-$ transition derived from the calculated $B(M1)$ value and the stopping time of the recoiling ${}^{10}_{\Lambda}$B. Then, the yield for the assumed peak (Y_2) was obtained for several energies by changing the γ-ray energy by 1 keV (Fig. 6.10). Here, the negative yield was turned to zero.

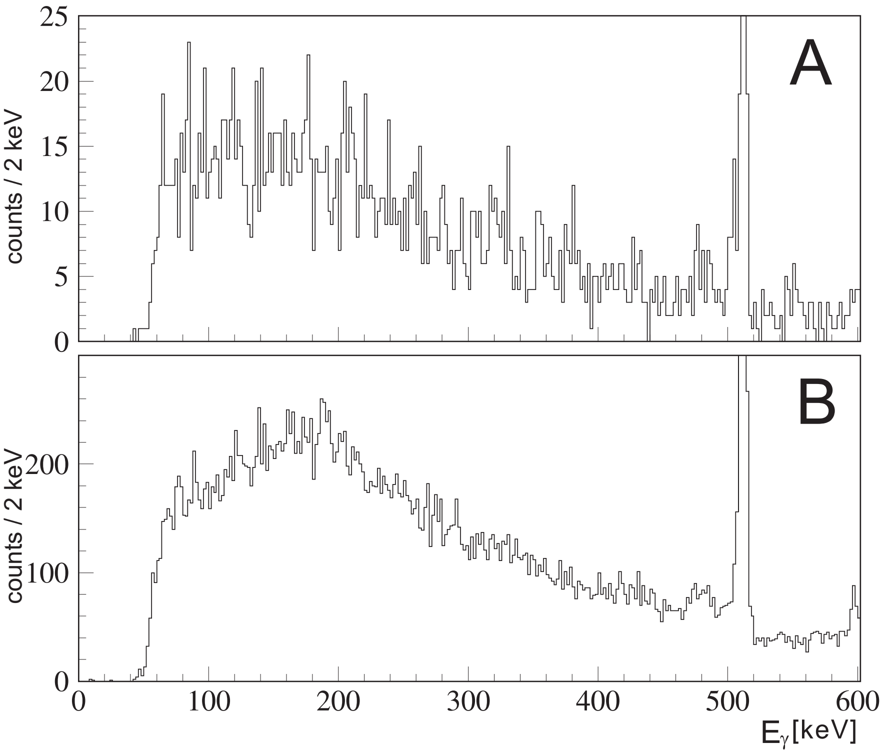

Figure 6.6: γ-ray spectrum measured for the region A (${}^{10}_{\Lambda}$B bound-state region) and B (unbound region), defined in Fig. 6.4. The events originated from the $K^- \to \pi^-\pi^0$ and the $K^- \to \mu^-\nu$ reactions were removed.

- Considering the statistical error of Y_2 (ΔY_2) and the difference between Y_1 and Y_2, the confidence level of the non-existence for the ${}^{10}_{\Lambda}$B ($2^- \to 1^-$) transition was evaluated. In Fig. 6.10, the error in Y_2 was given for 2σ. The error in Y_1 (± 40 %) was also shown in this figure.

Figure 6.10 shows that the expected yield is not large enough to be observed in the present study. Therefore, conclusive information on the energy spacing between the ground-state spin doublet in ${}^{10}_{\Lambda}$B is not obtained. In Ref. [7], the expected yield for this transition was also estimated from the same experimental data using the yield of the ${}^{9}_{\Lambda}$Be ($5/2^+, 3/2^+ \to 1/2^+$) which was observed from the higher excited states in ${}^{10}_{\Lambda}$B and it was concluded that non-existence of the peak reported in the old experiment was confirmed with higher statistics. However, this estimation is not reliable at all because ambiguities from the calculated (K^-, π^-) cross section of each state in ${}^{10}_{\Lambda}$B and the calculated branching ratio of the state going to the ${}^{9}_{\Lambda}$Be ($5/2^+, 3/2^+$) states are significantly large.

The sensitivity of the present study was found to be not enough . It can be understood by following reasons.

- γ-ray background was not suppressed enough because of the rather poor mass resolution of the magnetic spectrometers.
- The photo-peak efficiency of the Ge detectors was not accurately measured for the γ ray around 6 MeV.
- Ambiguity in the calculated (K^-, π^-) cross sections is large; the cross section for ${}^{10}_{\Lambda}$B (2^-) state should be precisely measured using a thin target.
- Number of irradiated K^- was not enough.

Considering these problems, the γ-ray spectroscopy experiment of ${}^{10}_{\Lambda}$B should be performed in near future at J-PARC using a magnetic spectrometer with better mass resolution.

§ 5 ΛN effective interaction parameters

In the present experiment, the ${}^{10}_{\Lambda}$B $(2^- \to 1^-)$ γ ray was not observed, although we were not able to confirm the non-existence of the transition with energy larger than 100 keV, which was claimed in the previous experiment. If the energy spacing of the ground-state spin doublet in ${}^{10}_{\Lambda}$B $(2^-, 1^-)$ is confirmed to be too small to be observed $(E(2^-) - E(1^-) < 100$ keV) in the future, a constraint will be given to the strength of the spin-spin interaction. As we have already mentioned in Chapter 1, the energy spacing was calculated using the parameters in Table 1.1 as

$$\begin{aligned} E(2^-) - E(1^-) &= 0.578\Delta + 1.414 S_\Lambda + 0.014 S_N - 1.068 T + \Lambda\Sigma \\ &= 197 \text{ [keV]}. \end{aligned} \tag{6.2}$$

Here, $\Lambda\Sigma$ expresses the ΛN-ΣN coupling effect and is calculated to be -15 keV. If we determine the spin-spin parameter (Δ) from the pervious experimental limit for the energy spacing of ${}^{10}_{\Lambda}$B $(2^-, 1^-)$, this parameter becomes 0.3 MeV. This result is much different from the value of 0.458 MeV obtained from ${}^{7}_{\Lambda}$Li.

Since Δ is determined from the energy spacing of the Λ-spin-flip $M1$ transition, this parameter is not affected by the core state in the weak-coupling scheme. Therefore, the ambiguity in the theoretical calculation for the ${}^{10}_{\Lambda}$B $(2^-, 1^-)$ spacing is expected to be smaller than the calculation for the ${}^{11}_{\Lambda}$B $(1/2^+, 5/2^+)$ spacing. It is conjectured that in the present case, one possible reason for the inconsistency of Δ is the effect from the ΛNN three body interaction.

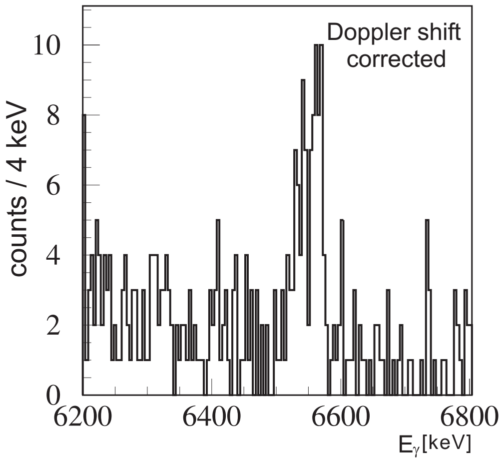

Figure 6.7: γ-ray spectrum of the ${}^{16}_{\Lambda}$O $(1^-_2 \to 1^-_1, 0^-)$ transition measured using the H_2O target after the Doppler-shift correction. The width of the gate for the binding energy and the scattering angle were the same for the analysis of the ${}^{10}_{\Lambda}$B.

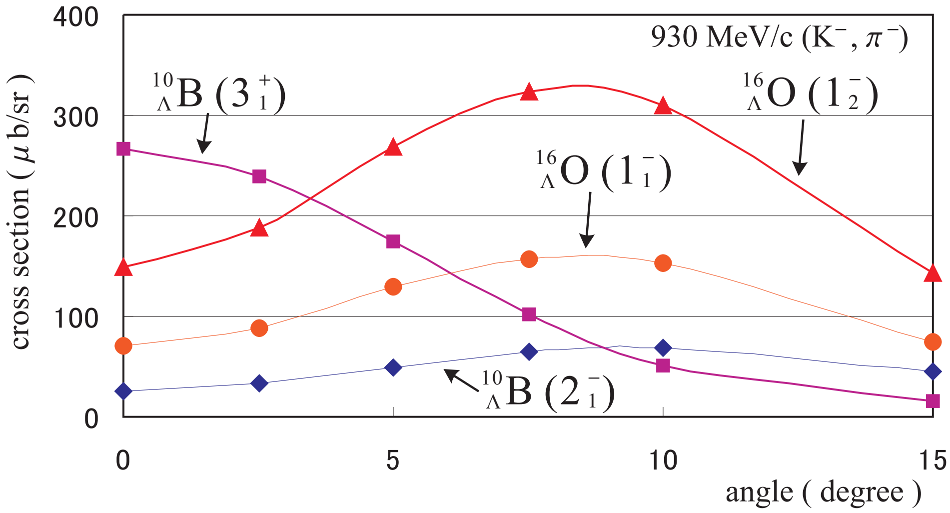

Figure 6.8: Cross sections for the 930 MeV/c K^- calculated by Motoba [53]. The angular dependences of the cross sections were calculated for ${}^{10}_{\Lambda}$B (2^-_1), ${}^{10}_{\Lambda}$B (3^+_1), ${}^{16}_{\Lambda}$O (1^-_1) and ${}^{16}_{\Lambda}$O (1^-_2).

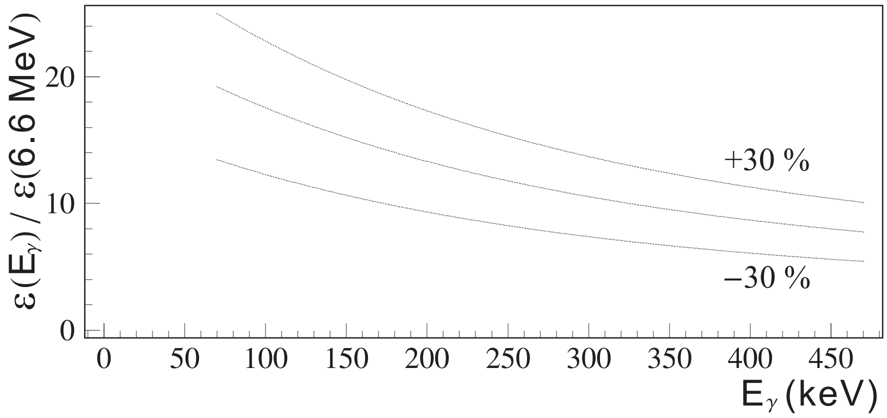

Figure 6.9: The energy dependence of the γ-ray detection efficiency. The efficiency was simulated using GEANT4 and obtained relative to the efficiency for 6.6-MeV γ ray.

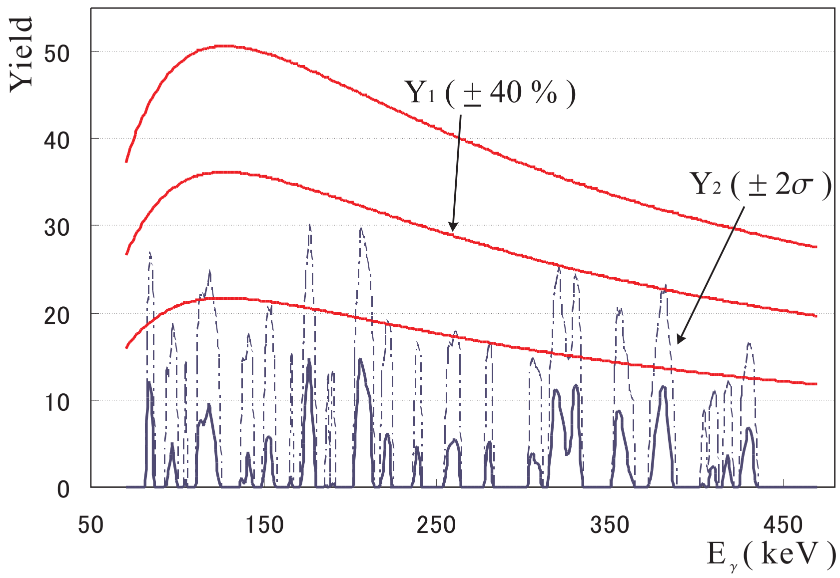

Figure 6.10: Energy dependence of the expected yield for the the ${}^{10}_{\Lambda}$B ($2^- \rightarrow 1^-$) transition (Y_1) and the yield for the assumed peak on the background (Y_2) (see text for details). In Y_1, branching ratio to the weak decay process was taken into account. The error in Y_1 was given for ± 40 % and the error in Y_2 was given for 2σ.

Chapter 7

Summary

The experiment for γ-ray spectroscopy of ${}^{11}_{\Lambda}$B (KEK-PS E518) was performed to confirm the ΛN effective interaction parameters. In this experiment, the excited states of ${}^{11}_{\Lambda}$B were produced by the (π^+, K^+) reaction and the γ rays were observed using a germanium detector array, Hyperball. In order to observe the γ rays from ${}^{11}_{\Lambda}$B, the bound states region was selected from the excitation energy measured by the magnetic spectrometers. Then, six γ-ray transitions from ${}^{11}_{\Lambda}$B were observed at 263.6 ± 0.5 (stat.) $\pm$ 1.1 (syst.) keV, $457.6 \pm 1.2 \pm 1.1$ keV, $504.7 \pm 1.0 \pm 1.1$ keV, $569.5.0 \pm 0.5 \pm 1.1$ keV, $1483.3 \pm 0.2 \pm 0.7$ keV and $2476.9 \pm 2.1 \pm 1.2$ keV.

In the weak coupling scheme, there are three candidates for the spin assignment of the 1483-keV transition, namely $1/2^+ \to 5/2^+$, $3/2^+ \to 5/2^+$ and $1/2^+; T = 1 \to 5/2^+$. Among them, ${}^{11}_{\Lambda}$B (E2; $1/2^+ \to 5/2^+$) is suggested to be the most probable assignment using a shell-model calculation by Millener. On the other hand, the peak at 2477 keV is suggested to be $M1(3/2^+; T = 1 \to 1/2^+)$ where the core state of $1/2^+$ state is ^{10}B(1^+, 2154 keV). In order to establish a level scheme for all of the γ-ray transitions observed in the present study, γ-γ coincidence method is necessary. It will be possible in near future by using an upgraded Hyperball.

The measured energy spacings of the 1483-keV and the 2477-keV transitions are significantly different from a theoretical prediction derived from the previously determined parameters of the ΛN spin-dependent effective interactions. In the present case, it is also conjectured that the wave functions of the core nucleus, ^{10}B, have to be improved.

The experiment for γ-ray spectroscopy of ${}^{10}_{\Lambda}$B (BNL-AGS E930('01)) was also performed to measure the energy spacing of the ground-state spin doublet. In this experiment, the corresponding transition was not observed for the γ-ray energy higer than 50 keV. Using the calculated values of the (K^-, π^-) cross section for the ${}^{10}_{\Lambda}$B (2^-) and the ${}^{16}_{\Lambda}$O (1^-_2) states, it is concluded that the expected yield for the ${}^{10}_{\Lambda}$B $(2^-, 1^-)$ transition was not large enough to be observed. If the energy spacing is smaller than 50 keV, this result is also different from a theoretical prediction derived from the previously determined parameters of the ΛN spin-dependent effective interactions. One of the possible reasons for the inconsistency in ${}^{10}_{\Lambda}$B is the effect from the ΛNN three body interaction.

The present study for the ${}^{11}_{\Lambda}$B and ${}^{10}_{\Lambda}$B imply that hypernuclear structure cannot be always reproduced consistently with the ΛN spin-dependent interaction parameters in the present framework. These results show that it is necessary to investigate structure of several more hypernuclei both experimentally and theoretically to confirm the ΛN interaction.

Appendix A

Matrix elements of the two-body ΛN forces

The spin dependence of the ΛN effective interaction has been studied from the excitation energies of the low-lying states in p-shell hypernuclei. In appendix A, the procedure to set up expressions for the matrix elements of the two-body ΛN forces will be described.

In a weak-coupling scheme, the level energies (E) are expressed in terms of hamiltonians for a core nucleus (H_{core}) and a part which is described by the ΛN effective interaction (H_Λ) as

$$\begin{aligned} E &= \langle \Psi_{HY} \,|(H_{core} + H_\Lambda)|\, \Psi_{HY} \rangle \\ &= E_{core} + \Delta E_\Lambda, \end{aligned} \tag{A.1}$$

where Ψ_{HY} is the wave function of the hypernuclear state. Since we consider low-lying states of p-shell hypernuclei, we take a shell model with a Λ in the s orbit and the $A-5$ nucleons in the p orbit ($p_N^{A-5} s_\Lambda$), where A is the mass number of the hypernucleus including a Λ. Then, H_Λ is expressed as

$$H_\Lambda = -\frac{\hbar^2}{2m}\Delta_{\mathbf{r_\Lambda}} + V_{\Lambda\text{-}\alpha}(\mathbf{r_\Lambda} - \mathbf{r_\alpha}) + \sum_{i=1}^{A-5} V_{\Lambda N_i}(\mathbf{r_\Lambda} - \mathbf{r_{N_i}}). \tag{A.2}$$

Here, $V_{\Lambda\text{-}\alpha}$ is the potential between the Λ in the s-orbit and the α core, namely the four nucleons in the s-orbit coupled to $L = 0$ and $S = 0$ ($s_N s_\Lambda$). $V_{\Lambda N_i}$ is the potential between i-th nucleon in the p-orbit and the Λ ($p_{N_i} s_\Lambda$).

The $p_N s_\Lambda$ interaction is shown in the last term of Eq. (A.2). This term is expressed using the ΛN effective interaction potential given in Eq. (1.1) as

$$\begin{aligned} \sum_i^{A-5} V_{\Lambda N_i}(\mathbf{r_\Lambda} - \mathbf{r_{N_i}}) = (A-5)\cdot V_0(r) + V_\sigma(r)\sum_i^{A-5} \mathbf{s_{N_i}}\cdot\mathbf{s_\Lambda} + V_N(r)\sum_i^{A-5} \mathbf{l_{N_i\Lambda}}\cdot\mathbf{s_{N_i}} \\ + V_\Lambda(r)\sum_i^{A-5} \mathbf{l_{N_i\Lambda}}\cdot\mathbf{s_\Lambda} + V_T(r)\sum_i^{A-5} \mathbf{S_{N_i\Lambda}}. \end{aligned} \tag{A.3}$$

On the other hand, Ψ_{HY} is divided into the core, $s_N s_\Lambda$ and $p_N s_\Lambda$ part, and expressed using a relative wave function between a nucleon and the Λ ($\phi_{\Lambda N}$) as

$$\begin{aligned}\Psi_{HY}(\mathbf{r_1}, \mathbf{r_2}, \ldots, \mathbf{r_{A-1}}, \mathbf{r_\Lambda}) &= \prod_{i,j}^{A-1} \phi_{N_i N_j}(\mathbf{r_i} - \mathbf{r_j}) \cdot \prod_{i}^{A-1} \phi_{\Lambda N_i}(\mathbf{r_i} - \mathbf{r_\Lambda}) \\ &= \Psi_{core}(\mathbf{r_1}, \mathbf{r_2}, \ldots, \mathbf{r_{A-1}}) \cdot \underbrace{\prod_{i}^{4} \phi^s_{\Lambda N_i}(\mathbf{r_i} - \mathbf{r_\Lambda})}_{s_N s_\Lambda} \cdot \underbrace{\prod_{i}^{A-5} \phi^p_{\Lambda N_i}(\mathbf{r_i} - \mathbf{r_\Lambda})}_{p_N s_\Lambda}.\end{aligned} \tag{A.4}$$

Here, $\phi^s_{\Lambda N_i}$ and $\phi^p_{\Lambda N_i}$ denote the relative wave functions between a Λ and a nucleon in the s and p orbit, respectively. Since the spatial components of the wave function, $\phi^p_{\Lambda N}$ are considered to be the same for any combination of $p_N s_\Lambda$, the contribution from the $p_N s_\Lambda$ effective interaction to the hypernuclear level energies is expressed in terms of five parameters ($\overline{V}$, Δ, S_Λ, S_N and T) corresponding to radial integrals of $V_0(r)$, $V_\sigma(r)$, $V_\Lambda(r)$, $V_N(r)$ and $V_T(r)$ with $\phi^p_{\Lambda N}$. For example, the contribution of the spin-spin interaction for a hypernuclear state with total angular momentum J is calculated from Eq. (A.3) as

$$\begin{aligned}\Delta E_{\Lambda,\sigma} &= \left\langle \Psi_{HY} \left| V_\sigma(r) \sum_{N}^{A-5} \mathbf{s_N} \cdot \mathbf{s_\Lambda} \right| \Psi_{HY} \right\rangle \\ &= \langle J | \mathbf{S_c} \cdot \mathbf{s_\Lambda} | J \rangle \cdot \Delta \\ &= \frac{1}{2} \langle J | (\mathbf{S_c} + \mathbf{s_\Lambda})^2 - \mathbf{S_c}^2 - \mathbf{s_\Lambda}^2 | J \rangle \cdot \Delta\end{aligned} \tag{A.5}$$

Here, the hypernuclear state $|J\rangle$ is expressed as a combination of the core state $|J_c\rangle$ and the Λ state $|J_\Lambda\rangle$, where $J_\Lambda = s_\Lambda = 1/2$ in the present case for the Λ in the s orbit. In the weak-coupling scheme, $|J_c\rangle$ is preserved in $|J\rangle$, namely, J_c is a good quantum number. $|J_c\rangle$ is expressed by a combination of the orbital angular momentum (L_c) and the spin (S_c) of the core state as

$$|J_c\rangle = \sum_{L_c, S_c} C_{L_c, S_c} |J_c; L_c S_c\rangle, \tag{A.6}$$

where C_{L_c,S_c} is derived from shell-model calculations for the core nuclei. Therefore, $|J\rangle$ is expressed as a combination of three angular momenta, L_c, S_c and s_Λ as

$$|J\rangle = \sum_{L_c, S_c} C_{L_c, S_c} |(L_c S_c) J_c, s_\Lambda; J\rangle. \tag{A.7}$$

Since $S_c + s_\Lambda$ which appears in Eq. (A.5) is not a good quantum number for $|(L_c S_c) J_c, s_\Lambda; J\rangle$, $|(L_c S_c) J_c, s_\Lambda; J\rangle$ has to be decomposed into eigenfunctions using

Racah coefficients. Then, $|(L_cS_c)J_c, s_\Lambda; J\rangle$ is expressed in terms of $6j$-symbols as

$$|(L_cS_c)J_c, s_\Lambda; J\rangle = \sum_{J'}(-1)^{L_c+S_c+s_\Lambda+J}\sqrt{(2J_c+1)(2J'+1)}\begin{Bmatrix} L_c & S_c & J_c \\ s_\Lambda & J & J' \end{Bmatrix}|(S_cs_\Lambda)J', L_c; J\rangle, \tag{A.8}$$

where $J_c = L_c \otimes S_c$, $J' = S_c \otimes s_\Lambda$ and $J = L_c \otimes S_c \otimes s_\Lambda$. Considering the all components in Eq. (A.7), the strength of the spin-spin interaction is obtained.

For example, the contribution from the spin-spin interaction to the energy spacing of the ground-state spin-doublet in ${}^{11}_{\Lambda}\mathrm{B}(7/2^+, 5/2^+)$ can be calculated using a simplified LS component for ${}^{10}\mathrm{B}(3^+)$ state. Considering that the ${}^{10}\mathrm{B}(3^+)$ is mainly composed of the $L_c = 2$ and $S_c = 1$ configuration, the contribution is expressed as

$$\begin{aligned}
\Delta E_{\Lambda,\sigma}(7/2^+) &- \Delta E_{\Lambda,\sigma}(5/2^+) \\
&= \frac{1}{2}\left(\langle 7/2|(\mathbf{S_c}+\mathbf{s_\Lambda})^2|7/2\rangle - \langle 5/2|(\mathbf{S_c}+\mathbf{s_\Lambda})^2|5/2\rangle\right)\cdot\Delta \\
&= \frac{1}{2}\Bigg(\underbrace{\frac{3}{2}\left(\frac{3}{2}+1\right)}_{J=7/2} - \underbrace{\frac{7}{9}\cdot\frac{1}{2}\left(\frac{1}{2}+1\right) + \frac{2}{9}\cdot\frac{3}{2}\left(\frac{3}{2}+1\right)}_{J=5/2}\Bigg)\cdot\Delta \qquad \text{(A.9)} \\
&= \frac{7}{6}\Delta.
\end{aligned}$$

In order to obtain more realistic contribution, it is necessary to use a shell-model calculation as described in Appendix B. For the other spin-dependent interactions, the strengths are calculated in similar manners [57].

Appendix B

Wave function of ^{10}B

In order to describe the structure of the $^{11}_{\Lambda}$B using a weak-coupling scheme, it is necessary to understand the structure of the core nucleus, ^{10}B. Millener calculated the core wave function based on the Barker I wave function. Barker modified the (6–16)2BME parameter which is proposed by Cohen and Kurath [55] to give better agreement with experiments for the electromagnetic transition strengths and energies of the low-lying levels of ^{10}B [36]. The improved parameters were obtained by mixing the two lowest $1^+; T = 0$ states and the $2^+; T = 0$ states. The experimental data have been updated after the calculation by Barker. Therefore, Millener improved the Barker I wave function using typical effective g-factors instead of the bare g-factors [3]. The comparison between theory and experiment [56] for electromagnetic transition strengths is summarized in Table B.1. The states which are especially important for the γ-decay scheme in $^{11}_{\Lambda}$B were shown in this table.

As mentioned in Appendix A, the angular momentum of the core state has to be decomposed into LS component to describe the hypernuclear states in terms of four spin-dependent ΛN effective interaction parameters. The states in ^{10}B are interpreted by the dominance of the [42] spatial symmetry, which is proposed from the shell model calculation by Kurath [35]. The observed features of the electromagnetic transition in ^{10}B are well explained by this model. In this spatial symmetry, the allowed L values are 0 and 2 for $K_L = 0$ and 2, 3 and 4 for $K_L = 2$, where K_L is obtained by projecting L into an intrinsic coordinate system. Spin and isospin values of the low-lying states in ^{10}B can only be $S = 1$ for $T = 0$ or $S = 0$ for $T = 1$. Then, the LS component of each state in ^{10}B can be calculated. Table B.2 shows a projected component of the Barker I wave functions for ^{10}B [3]. If there is a large contribution from the spin-orbit interaction, this symmetry cannot be used because the spin-orbit interaction also mixes different spatial symmetries.

Table B.1: The comparison between theory and experiment for electromagnetic transition strengths in ^{10}B.

ΔE [keV]	Spin $J_i^\pi;T_i$	$J_f^\pi;T_f$	Mult.	$B(\lambda)$ [W.u.] Expt.	(6–16)2BME	Barker I	Millener
718	$1^+;0$	$3^+;0$	E2	3.20	3.05	2.18	3.09
1022	$0^+;1$	$1^+;0$	M1	4.2	22.6	25.6	6.20
2154	$1^+;0$	$3^+;0$	E2	1.33	0.51	1.1	0.52
1436	$1^+;0$	$1^+;0$	M1	9.1×10^{-5}	8.6×10^{-3}	1.9×10^{-5}	9.5×10^{-5}
			E2	12.2	1.5	2.6	3.7
414	$1^+;0$	$0^+;1$	M1	0.107	1.25	0.175	0.118
3587	$2^+;0$	$3^+;0$	M1	2.6×10^{-4}	1.7×10^{-6}	6.5×10^{-4}	2.1×10^{-4}
			E2	0.90	1.4	1.7	2.43
2869	$2^+;0$	$1^+;0$	M1	$< 5\times10^{-4}$	1.3×10^{-3}	1.7×10^{-4}	5.4×10^{-5}
			E2	13.9	6.28	5.14	7.3
1433	$2^+;0$	$1^+;0$	M1	8.5×10^{-3}	3.5×10^{-2}	3.2×10^{-2}	9.9×10^{-3}
			E2	11.9	1.7	2.9	4.2
5164	$2^+;1$	$3^+;0$	M1	2.3×10^{-2}	0.09	0.02	4×10^{-6}
			E2	< 0.7	0.07	0.1	0.034
4446	$2^+;1$	$1^+;0$	M1	0.18	8.9×10^{-5}	0.35	0.14
3010	$2^+;1$	$1^+;0$	M1	1.71	6.03	5.67	1.51
1577	$2^+;1$	$2^+;0$	M1	1.41	6.56	6.83	1.44

Table B.2: The [42] symmetry components of the Barker I wave functions for ^{10}B.

E_x [keV]	Spin $J^\pi;T$	$L=0$	$K_L=0$ $L=2$	$K_L=2$ $L=2$	$L=3$	$L=4$	%[42]
0	$3^+;0$		0.0459	0.8836	-0.3823	0.0776	93.50
718	$1^+;0$	0.9498	-0.0186	-0.1486			92.46
1740	$0^+;1$	0.9128					83.31
2154	$1^+;0$	0.0726	0.8058	-0.3117			75.17
3587	$2^+;0$		0.9618	-0.1174	0.1417		95.90
4774	$3^+;0$		0.9739	0.0426	-0.0372	-0.0238	95.22
5164	$2^+;1$		0.8518	0.1028			73.62
5920	$2^+;0$		-0.0891	0.9279	-0.3140		96.75

Appendix C

Transition probability in the weak-coupling scheme

In the weak-coupling scheme, four hypernuclear γ-ray transitions in Fig. C.1 can be considered from the spin coupling between a Λ and a core nucleus, namely a part of the hypernucleus except for a Λ. In Appendix C, the procedure to derive the branching ratio between these γ-ray transitions from initial states (J_{i1}, J_{i2}) to the states which are connected by electromagnetic transitions with multipolarity λ (J_{f1}, J_{f2}) will be described.

In the weak-coupling scheme, the reduced transition probabilities of the hypernuclear γ-ray transitions ($B_{HY}(\lambda)$) can be expressed as

$$B_{HY}(\lambda) = \frac{1}{2J_i+1}|\langle J_f\|\boldsymbol{O_c}+\boldsymbol{O_\Lambda}\|J_i\rangle|^2 = \frac{1}{2J_i+1}|\langle J_f\|\boldsymbol{O_c}\|J_i\rangle+\langle J_f\|\boldsymbol{O_\Lambda}\|J_i\rangle|^2, \quad \text{(C.1)}$$

where $\boldsymbol{O_c}$ and $\boldsymbol{O_\Lambda}$ are operators for the electromagnetic multipole of the core nucleus and for the the magnetic moment of a Λ, respectively. $\langle J\|\boldsymbol{O}\|J\rangle$ is the reduced matrix element defined with the Wigner-Eckart theorem. If the core states are different between the initial and the final states, only the term which is related to the core transition survives in Eq. (C.1) [39]. Therefore, $B_{HY}(\lambda)$ can be derived from the tranisiton probability of the core transition by decomposing the initial and the final states of hypernucleus ($|J_i\rangle, |J_f\rangle$) into the eigenfunctions of the Λ ($|s_\Lambda\rangle$) and the core nucleus ($|J_{ci}\rangle, |J_{cf}\rangle$) [1].

Essentially, the reduced transition probability for a core tranisiton ($B_{core}(\lambda)$) can be described using reduced matrix elements of four hypernuclear transitions which are associated with one core transition as

$$\begin{aligned} B_{core}(\lambda) &= \frac{1}{2J_{ci}+1}|\langle J_{cf}\|\boldsymbol{O_c}\|J_{ci}\rangle|^2 \\ &= \frac{1}{2J_{ci}+1}\Bigg((2J_{i1}+1)\sum_{n=1,2}|\langle J_{fn}\|\boldsymbol{O_c}+\boldsymbol{O_\Lambda}\|J_{i1}\rangle|^2 \\ &\qquad + (2J_{i2}+1)\sum_{n=1,2}|\langle J_{fn}\|\boldsymbol{O_c}+\boldsymbol{O_\Lambda}\|J_{i2}\rangle|^2\Bigg). \end{aligned} \quad \text{(C.2)}$$

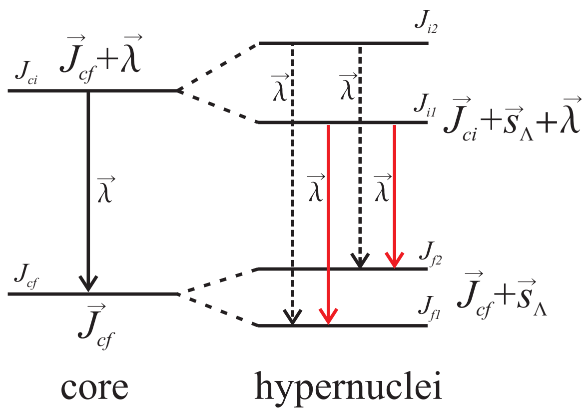

Figure C.1: The electromagnetic transitions between the hypernuclear states, which are based on a transition of the core nucleus. The reduced transition probability for the core nucleus can be written in terms of four hypernuclear transition probabilities.

By substituting Eq. (C.1) into Eq. (C.2), this equation can be written as

$$B_{core}(\lambda) = \frac{2J_{i1}+1}{2J_{ci}+1} \sum_{n=1,2} |\langle J_{fn} \| \boldsymbol{O_c} \| J_{i1} \rangle|^2 + \frac{2J_{i2}+1}{2J_{ci}+1} \sum_{n=1,2} |\langle J_{fn} \| \boldsymbol{O_c} \| J_{i2} \rangle|^2. \quad \text{(C.3)}$$

Here, four transitions are divided into two groups according to the initial states of the hypernuclear transitions (J_{i1}, J_{i2}). The coefficients are derived from the degeneracy of J_{i1} and J_{i2}. Then, $|J_{in}\rangle$ $(n = 1, 2)$ are decomposed into J_{fn} components as

$$\begin{aligned} |J_{in}\rangle &= |J_{in}; J_{ci}\rangle \\ &= \sum_{J_{fn}} (-1)^{J_{cf}+\lambda+s_\Lambda+J} \sqrt{(2J_{ci}+1)(2J_{fn}+1)} \begin{Bmatrix} \lambda & J_{cf} & J_{ci} \\ s_\Lambda & J_{in} & J_{fn} \end{Bmatrix} |J_{in}; J_{fn}\rangle. \end{aligned} \quad \text{(C.4)}$$

Here, the spin of the each state is described by a combination of three angular momenta, namely the total spin of the initial state in the core nucleus (J_{cf}), multipolarity of the core transition (λ) and the spin of Λ (s_Λ). In term of these angular momenta, the initial state of the core nucleus, the final states of the hypernucleus and the initial states of the hypernucleus are written as $J_{ci} = J_{cf} \otimes \lambda$, $J_{fn} = J_{cf} \otimes s_\Lambda$ and $J_{in} = J_{cf} \otimes s_\Lambda \otimes \lambda$, respectively. Then, Eq. (C.3) is expressed as,

$$\begin{aligned} B_{core}(\lambda) = &\frac{2J_{i1}+1}{2J_{ci}+1} \sum_{n=1,2} w(J_{fn}, J_{i1}, \lambda) |\langle J_{fn} \| \boldsymbol{O_c} \| J_{i1}; J_{fn} \rangle|^2 \\ &+ \frac{2J_{i2}+1}{2J_{ci}+1} \sum_{n=1,2} w(J_{fn}, J_{i2}, \lambda) |\langle J_{fn} \| \boldsymbol{O_c} \| J_{i2}; J_{fn} \rangle|^2. \end{aligned} \quad \text{(C.5)}$$

where $w(J_{fn}, J_{in}, \lambda)$ is expressed in terms of $6j$-symbol as,

$$w(J_{fn}, J_{in}, \lambda) = (2J_{ci}+1)(2J_{fn}+1) \begin{Bmatrix} \lambda & J_{cf} & J_{ci} \\ s_\Lambda & J_{in} & J_{fn} \end{Bmatrix}^2. \quad \text{(C.6)}$$

The reduced matrix elements in Eq. (C.5) are expressed in terms of the eigenfunctions of the Λ and the core nucleus as

$$\begin{aligned}\langle J_{fn}\|\boldsymbol{O_c}\|J_{i1};J_{fn}\rangle &= \langle J_{fn}\|\boldsymbol{O_c}\|J_{i2};J_{fn}\rangle \\ &= \langle s_\Lambda|\langle J_{cf}\|\boldsymbol{O_c}\|J_{ci}\rangle|s_\Lambda\rangle \\ &= \langle J_{cf}\|\boldsymbol{O_c}\|J_{ci}\rangle.\end{aligned} \tag{C.7}$$

Therefore, the reduced matrix elements in Eq. (C.5) take same value and the ratio of the reduced transition probability can be derived. In case of the two transitions, $J_{i1} \to J_{f1}$ and $J_{i1} \to J_{f2}$, the ratio is obtained to be,

$$R\left(\frac{J_{i1} \to J_{f1}}{J_{i1} \to J_{f2}}\right) = \frac{w(J_{f1}, J_{i1}, \lambda)}{w(J_{f2}, J_{i1}, \lambda)}. \tag{C.8}$$

For example, this calculation can be applied for the $B(E2)$ of the first $3/2^+$ to the ground-state spin doublet members $(7/2^+, 5/2^+)$ in ${}^{11}_{\Lambda}$B. This calculation shows that the $B(E2)$ of the $3/2^+ \to 7/2^+$ transition is six times larger than that of the $3/2^+ \to 5/2^+$ transition.

Appendix D

Previous experiment for the γ-ray spectroscopy of $^{10}_{\Lambda}$B

In the previous experiment by Chrien *et al.*, the γ-ray spectroscopy of $^{10}_{\Lambda}$B was attempted to measure the energy spacing of the ground-state spin doublet $(2^-, 1^-)$ [8]. In this experiment, γ rays from $^{10}_{\Lambda}$B was not observed for the energy region from 80 keV to 1 MeV. Considering the expected yield for the transition, they showed that obtained upper limit for the γ-ray yield is lower than the expected yield in the 95 % confidence level. Then, they concluded that the energy spacing of the ground-state spin doublet in $^{10}_{\Lambda}$B $(E(2^-) - E(1^-))$ is smaller than 80 keV. In Appendix D, the experimental condition for this measurement will be summarized to compare the result with the present study.

The experiment by Chrien was carried out with the same (K^-, π^-) reaction using a different beamline and magnetic spectrometers at BNL AGS. The difference in the experimental condition between previous and present experiment is summarized in Table D.1. The obvious differences were found in the irradiated number of K^-, photo peak efficiency of the Ge detectors and the mass resolution of the magnetic spectrometers. In the present experiment, while number of the irradiated K^- was four times smaller, the photo peak efficiency was eight times larger than the previous experiment. The beam momentum of K^- was slightly different but the cross section was calculated to be comparable [53]. Because of the acceptance of the spectrometer, the cross section for the effective solid angle was considered to be different. The acceptance of the magnetic spectrometer was not estimated for the present study but it can be expected from the previous experiments using the same spectrometers as shown in Table D.1. The product of the DAQ and the tracking efficiency was estimated to be worse in the present study, but the tracking efficiency is expected to be improved by further analysis. Because of the difference in the analysis condition in removing the background from K^- decay, it is difficult to compare the difference resulting from the other analysis efficiencies quantitatively. Although, it is expected that the γ-ray yield for $^{10}_{\Lambda}$B $(2^-, 1^-)$ was larger in the present experiment (see Chapter 6).

The amount of the background was also different between two experiments. Because of the poorer mass resolution, the width of the region which was set to select events from the bound states was broader in the present experiment. Since the (K^-, π^-) cross section for the other excited state is significantly large, the amount of γ-ray background rapidly increase according to the width of the selected region. In addition, there is another difference in the method for the background suppression. In the present experiment, we used BGO scintillation counters to suppress background from the Compton scattering and the decay of π^0 (see Chapter 2). In this point, the γ-ray background originated from the target was removed more effectively by a factor of about two in the present experiment. As a result, the sensitivity for the γ rays from ${}^{10}_{\Lambda}$B in the present study is expected to be comparable to the previous experiment by further analysis.

Table D.1: Difference in the experimental setup between the previous [8] and present experiment.

	Previous experiment	Present experiment
Beam momentum	800 MeV/c	930 MeV/c
Irradiated K^-	2.0 $\times 10^{10}$	0.56 $\times 10^{10}$
Target thickness	12.3 g/cm^2	14.2 g/cm^2
Volume of Ge crystal	50 mmϕ $\times$ 40 mm	70 mmϕ $\times$ 70 mm
Photo peak efficiency	0.5 % @ 478 keV	4 % @ 500 keV [7]
Mass resolution	6 MeV(FWHM)	15 MeV(FWHM)
Width for bound states	8 MeV	20 MeV
Solid angle of spectrometer	18 msr	20–40 msr$^{(*}$
Calculated cross section	50 μb/sr @ 5.8°	69.1 μb/sr @ 7.5°
Expected yield	40 count @ 200 keV	35 count @ 200 keV$^{(*}$
Signal / Noise	1	$\sim 0.3^{(*}$
Signal / $\sqrt{\text{Noise}}$	1	$\sim 0.5^{(*}$

($*$: Estimation will be improved.

Acknowledgements

There are many people who have been a great source of strength while writing this thesis. Let me introduce some of them to show my appriciation. First, I would like to express my appriciation to Prof. H. Tamura, my graduate advisor, for his kindhearted direction. Prof. Tamura was the one who led and encouraged me to study the hypernuclear physics. Without his understanding and help, I could not have finished this thesis. I owe him lots of gratutude for having me shown this way of resarch.

Next, I would appreciate Prof. O. Hashimoto for giving me a good opportunity to study an interesting subject. His integral view on resarch has made a deep impression for me. Also, I would like to say a special thanks to Prof. S. N. Nakamura, Prof. T. Takahashi and Dr. Y. Fujii who kept an eye on the progress of my work and always was available when I needed their advice. I am grateful for Prof. T. Nagae, Prof. T. Fukuda, Prof. H. Outa and Dr. S. Ajimura who helped me to perform an experiment at KEK-PS. They gave me a valuable advice on this experiment. I also would like to acknowledge the KEK staffs for their supports to maintain the experiment.

I would like to thank Dr. K. Tanida who gave me strict and extensive comments. The many discussions with him had a direct impact on the final form and quality of this thesis. He could not even realize how much I have learned from him. I thank Dr. M. Ukai for the invalid discussion about the analysis. I sincerely thank Mr. K. Miwa and Mr. K. Mizunuma for their contribution to setup the experiment and analyze data. Dr. P. K. Saha, Dr. A. Toyoda, Dr. H. Hotchi and Mr. W. Imoto were very helpful during the experiment. It was pleasure for me to work with them. I also thank to Dr. T. Saito who took care of me a lot when I have visited his resarch institute. I acknowledge Dr. T. Koike, Mr. M. Ejima and Ms. S. Kinoshita for their substantial contribution to many tasks which were necessary for the present work. I had the pleasure to work with several students who did their graduation work in our group and have been somehow beneficial for the present work in this thesis. I would like to thank Ms. N. Kawamura, Mr. M. Kato and Mr. N. Chiga for their supports.

I am grateful to Dr. D.J. Millener and Prof. T. Motoba for theoretical calculations and discussions. They showed me very important direction to understand the experimental data.

I feel a deep sense of gratitude for my parents who formed a part of my vision and taught me the good things that really matter in life.

References

[1] R.H. Dalitz and A. Gal, Ann. Phys. (N.Y.) **116** (1978) 167.

[2] D.J. Millener, A. Gal, C.B. Dover, R.H. Dalitz, Phys. Rev. C**31** (1985) 499.

[3] D.J. Millener, private communication.

[4] H. Tamura *et al.*, Phys. Rev. Lett. **84** (2000) 5963.

[5] H. Akikawa *et al.*, Phys. Rev. Lett. **88** (2002) 082501.

[6] S. Ajimura *et al.*, Phys. Rev. Lett. **86** (2001) 4255.

[7] M. Ukai, Doctoral thesis, Tohoku Univ. (2004)

[8] R.E. Chrien *et al.*, Phys. Rev. C**41** (1990) 1062.

[9] H. Bandō, Prog. Theor. Phys. **66** (1981) 1349.

[10] T.A. Rijken, V.G.J. Stoks, Y. Yamamoto, Phys. Rev. C **59** (1999) 21.

[11] M.M. Nagels, T.A. Rijken, J.J. de Swart, Phys. Rev. D **15** (1977) 1947.

[12] M.M. Nagels, T.A. Rijken, J.J. de Swart, Phys. Rev. D **20** (1979) 1633.

[13] M.Bedjidian *et al.*, Phys. Lett. **62B** (1976) 467.

[14] M.Bedjidian *et al.*, Phys. Lett. **83B** (1979) 252.

[15] B.F. Gibson, I.R. Afnan, J.A. Carlson, and D.R. Lehman, Prog. Theor. Phys. Suppl. **117** (1994) 339.

[16] Y. Akaishi, T. Harada, S. Shinmura, and K.S. Myint, Phys. Rev. Lett. **84** (2000) 3539.

[17] E. Hiyama, K. Kaminuma, T. Motoba, T. Yamada, and Y. Yamamoto, Nucl. Phys. **A 639** (1998) 169c.

[18] E. Hiyama, Nucl. Phys. **A 670** (2000) 273c.

[19] K. Tanida *et al.*, Phys. Rev. Lett. **86** (2001) 1982.

[20] D.J. Millener, Nucl. Phys. **A 691** (2001) 93c.

[21] V.N. Fetisov, L. Majling, J. Žofka and R.A. Eramzhyan, Z. Phys. **A 339** (1991) 399.

[22] H. Hotchi *et al.*, Phys. Rev. C **64** (2001) 044302.

[23] E. Hiyama, Phys. Rev. Lett. **85** (2000) 270.

[24] T. Hatsuda and S.H. Lee, Phys. Rev. C **60** (1992) R24.

[25] K. Ozawa *et al.*, Phys. Rev. Lett. **86** (2001) 5019.

[26] M. Naruki *et al.*, Nucl. Phys. **A 721** (2003) 297c.

[27] T. Takeuchi, K. Shimizu, K. Yazaki, Nucl. Phys. **A 481** (1988) 693.

[28] K. Saito, M. Oka, T. Suzuki, Nucl. Phys. **A 625** (1997) 95.

[29] H. Bandō, T. Motoba, and J. Žofka, Int. J. Mod. Phys. A**5** (1990) 4022.

[30] H. Bandō, T. Motoba, M. Sotona, and J. Žofka, Phys. Rev. C **39** (1989) 587.

[31] T. Motoba, H. Bandō and K. Ikeda, Prog. Theor. Phys. **80** (1983) 189.

[32] E. Hiyama, M. Kaminuma, K. Miyazaki and T. Motoba, Phys. Rev. Lett. **86** (2001) 1982.

[33] K. Itonaga, T. Motoba, and H. Bandō, Prog. Theor. Phys. Suppl. **84** (1990) 291.

[34] K. Itonaga, T. Motoba, and M. Sotona, Prog. Theor. Phys. Suppl. **117** (1994) 17.

[35] D. Kurath, Nucl. Phys. **A 317** (1978) 175.

[36] F.C. Barker, Aust. J. Phys. **34** (1981) 7.

[37] D.J. Millener, nucl-th/0402091,*Proc. 8th Int. Conf. on "Hypernuclear and Strange Particle Physics"*, (Jlab, Oct. 2003), Nucl. Phys. **A** to be published.

[38] Y. Akaishi, T. Harada, S. Shinmura, and K.S. Myint, Phys. Re v. Lett. **84** (2000) 3539.

[39] A. de-Shalit, Phys. Rev. **122** (1961) 1530.

[40] T. Fukuda *et al.*, Nucl. Instr. Meth. A **361** (1995) 485.

[41] T. Hasegawa, Doctoral thesis, Tokyo Univ. (1994)

[42] H. Hotchi, Doctoral thesis, Tokyo Univ. (2000)

[43] http://www.ortec-online.com

[44] http://www.canberra.com

[45] K. Tanida, Doctoral thesis, Tokyo Univ. (2000)

[46] http://wwwkm.phys.sci.osaka-u.ac.jp/˜ajimura/mem

[47] M. Juric *et al.*, Nucl. Phys. **B 52** (1973) 1.

[48] M. Iwasaki, Low Energy Particle Simulator version 7.0, 1999 (unpublished)

[49] K. Mizunuma, Master's thesis, Tohoku Univ. (2002)

[50] J.F. Ziegler *et al.*, The Stopping and Range of Ions in Matter, http://www.srim.org

[51] D. Ziemińska, Nucl. Phys. **A 242** (1975) 461.

[52] Y. Miura, Master's thesis, Tohoku Univ. (2001)

[53] T. Motoba, private communication.

[54] T. Hasegawa, Phys. Rev. **C 53** (1996) 1210.

[55] S. Cohen and D. Kurath, Nucl. Phys. **73** (1965) 1.

[56] F. Ajzenberg-Selove, Nucl. Phys. **A 490** (1988) 1.

[57] A. Gal, J.M. Soper and R.H. Dalitz, Ann. Phys. (N.Y.) **63** (1971) 53.